Smoothed Particle Hydrodynamic Modelling of Wave Impact

A numerical and theoretical analysis of non-breaking wave loads on structures with overhang

by

Stefan Been

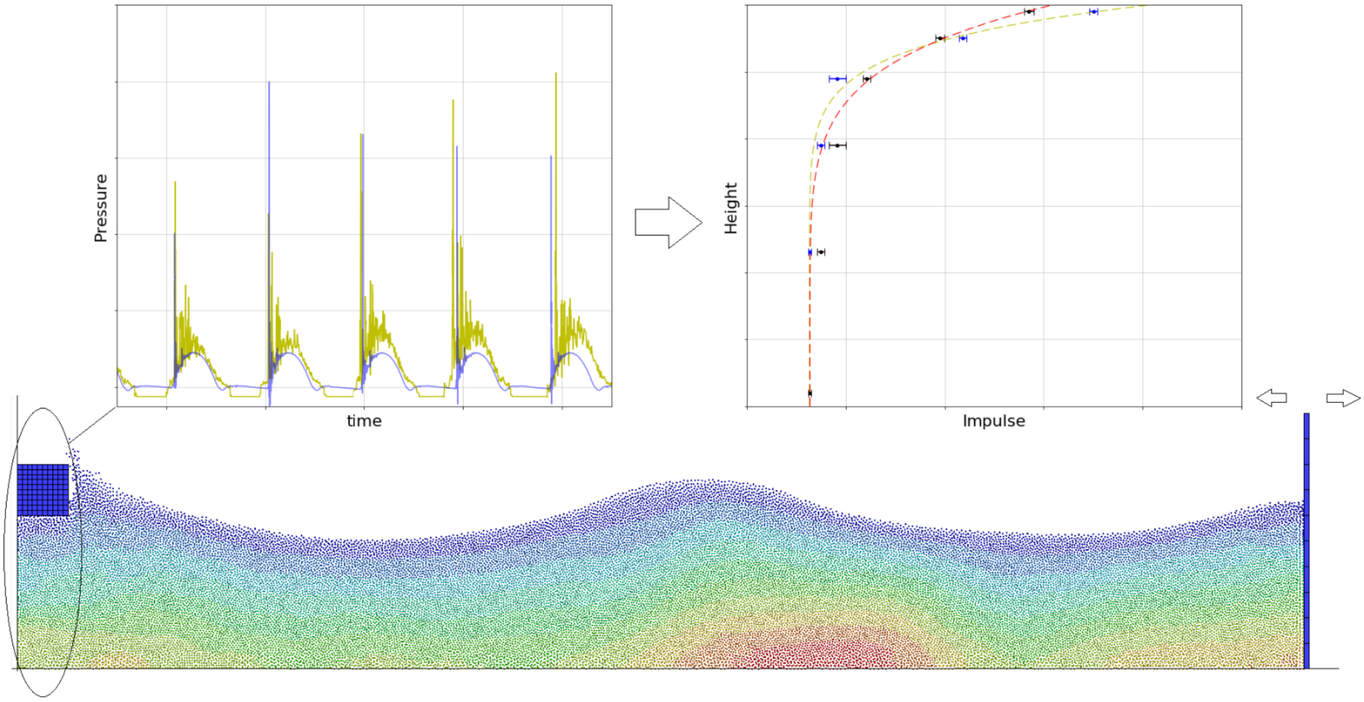

Smoothed Particle Hydrodynamic Modelling of Wave Impact

A numerical and theoretical analysis of non-breaking wave loads on structures with overhang

by

Stefan Been

Final report to obtain the Master's degree in Civil Engineering at the Delft University of Technology

to be publicly defended on July 30th, 2020 at 15:00 pm

Student number:	4330986	
Thesis committee:	Dr. Ir. A. Antonini	TU Delft, Chairman
	Dr. Ir. J. Bricker	TU Delft
	Ir. E. de Almeida Sousa	TU Delft
	Ir. W. F. Molenaar	TU Delft
	Ir. N. Kostense	Arcadis
	Ir. H. G. Tuin	Arcadis

This page intentionally left blank.

Preface

Before you lies my thesis as the final project in my Masters Hydraulic Engineering, with specialisation Hydraulic Structures and Flood Risk at the Delft University of Technology. It concludes my time as student, in which I gained a lot of knowledge in the world of civil engineering and discovered my passion for the giant Dutch structures that make up our defense system against the unforgiving sea.

In this project, I was able to fully apply my knowledge to act as an engineer to investigate wave impacts that cause headaches in the design of hydraulic structures, and contribute to the never ending developments that take place in the field of civil engineering. More so, it was a very insightful and educational experience in which I learned new skills as a numerical modeller and programmer. Before you commence reading the report, I would like to express my gratitude to the people that were of major importance in the realisation of this project and overall for my journey to become an engineer.

Firstly, I would like to thank Niels Kostense for taking me in at Arcadis and providing all the help I needed with the numerical tools. You are truly an expert and your ideas never failed to steer me in the right direction. Then, I would like to say thank you to Henry Tuin for joining my committee. Your endless enthusiasm was an inspiration and your theories and feedback improved the content of my thesis greatly. Furthermore, I would like to thank the members of my committee from the TU Delft. Alessandro Antonini for chairing the committee and for introducing me to the overhang problems. Without your input, I would not have had such a specialised research. Jeremy Bricker for his constructive and insightful feedback that shaped my thesis in the right way. Ermano de Almeida for being willing to include me in his Phd research by sharing his results of the experiments and for answering all my questions about them. And finally Wilfred Molenaar, for always reminding me to the practical side of the study and his advice on the structure of the report.

Lastly, I would like to sincerely thank my family and friends for their unconditional support. It helped me not only through the writing of the thesis, but through my time as a student overall. I hope I made you proud.

I wish you a pleasant read,

Stefan Been
Delft, July 2020

This page intentionally left blank.

Summary

Impulsive wave impact on hydraulic structures is a highly stochastic and uncertain process. This type of impact, defined by extreme peaks and a very short duration is not only caused by breaking waves, but also by non-breaking standing waves on structures with an overhang, such as culverts and steel gates. There is a need for analytical and numerical models that can accurately predict this behaviour. By integrating the pressure over the impact duration, the so called pressure-impulse can be obtained and translated to reaction forces (Chen et al., 2019), which provides more stable results than pressure peaks (de Almeida Sousa & Hofland, 2020).

In this thesis, smoothed particle hydrodynamics (SPH) is applied and compared to physical experiments. SPH distinguishes itself by discretising the numerical domain in particles instead of a grid, unlike traditional computational fluid dynamics (CFD). In doing so, it excels in free surface modelling and complex wave-structure interaction.

In an analysis of the theoretical background, various design formulae have been identified for non-breaking waves on vertical walls, namely Sainflou (1928), Goda (1972) and linear wave theory (LWT) (Airy, 1845). For the overhang construction, two models are proposed, which are the pressure-impulse model (Wood & Peregrine, 1996) and a conceptual model (Tuin, 2019) based on LWT, which is introduced in this thesis. The differences of the models lie in the schematisation of the stopped water mass; the pressure-impulse model assumes a circular mass over a width and depth equal to the overhang width W, with a constant upward velocity V, and disregards horizontal impact. The conceptual model splits the contribution to the total impulse in horizontal and vertical direction. In doing so, it assumes a rectangular (horizontal impact) and triangular (vertical impact) area of integration of the LWT velocities over the full water depth d. Both models are schematised in figure 3.

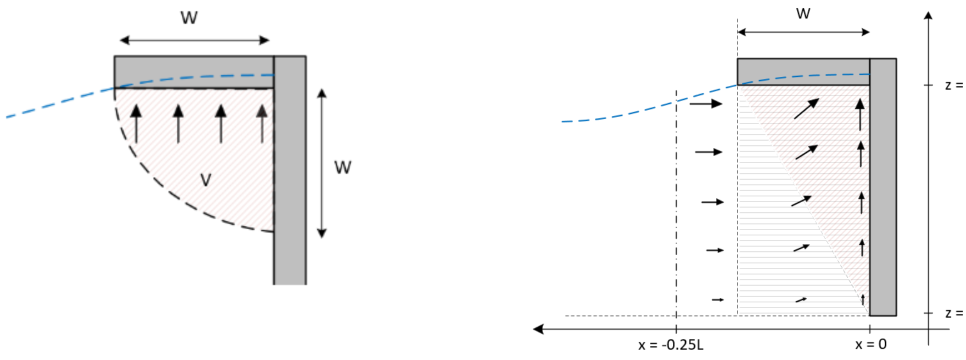

(a) Pressure-impulse model (b) Conceptual model

Figure 3: Assumptions velocity fields of theoretical models

In a literature review, it was concluded that SPH was not yet applied to non-breaking waves on overhangs. Besides, validation of the pressure-impulse model was scarce (de

Almeida Sousa & Hofland, 2020; Hofland et al., 2019). Therefore, this knowledge gap was treated by formulating the objectives to test SPH for structures with overhang, combined with validation of the theoretical models.

The physical experiments were conducted at the Delft University of Technology by de Almeida Sousa et al. (2019) and shared with the author for two short overhangs ($3 < d/W < 6$) and a case without overhang, all loaded by two wave conditions. The software applied throughout this report was DualSPHysics (Crespo et al., 2015) and LS-Dyna (Hallquist, 2006).

The results of the SPH models showed good agreement. For the structure without overhang, the wave fields and pressures showed an almost 1 to 1 correlation. The overhang configurations showed a repetitive overestimation of the uppermost sensors, just below the overhang. It was concluded that this was caused by the lack of air in the model, which provides a cushioning effect. The pressure-impulse profiles were well reproduced by SPH, which were obtained by applying a 3rd order Butterworth filter to the data set to filter out the quasi-static and impulsive time series. The variety of impact duration in the experiments (10-110 ms) due to entrapped air pockets, did not occur in the models, as a constant duration of 30-40 ms was found. However, the numerical pressure-impulse profiles somewhat corrected the overestimated pressures by the shorter duration, mitigating the lack of air. Moreover, 3-5 times less variability was observed when pressure-impulses were used.

In an analysis of the velocity fields, it was found that the stopped velocities at impact show circular contours, but with a decreasing magnitude over the width and depth, unlike the assumption in the pressure-impulse model. Furthermore, a contribution of the horizontal impact was found. Moreover, modified integration limits were proposed for the concept model as shown in figure 4 with W = overhang width.

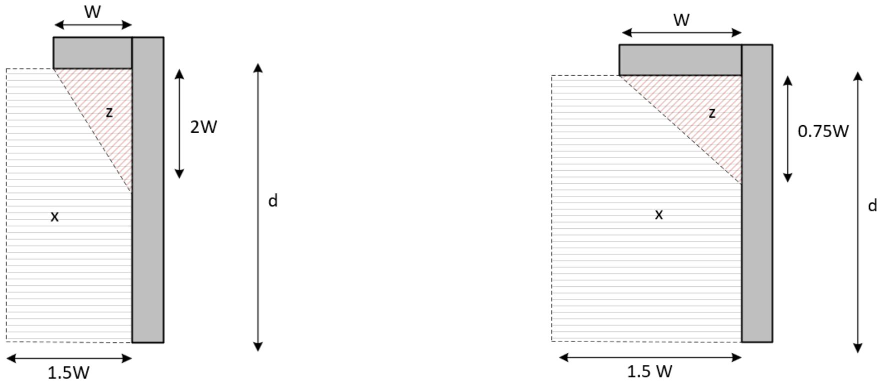

(a) Short overhang configuration (b) Longer overhang configuration

Figure 4: Conceptual model: Optimised areas of integration

By means of an analytical validation, the force-impulses and dimensionless pressure-impulse profiles were compared to SPH and the experiment. The pressure-impulse model showed a good fit to the profiles and accurately computed the force-impulses, for both the wall and overhang. The conceptual model was best applied to the longer overhang configuration, as it showed inaccuracy ($\sim$ 30%) for the short overhangs. The modified model, with the adapted areas of integration, returned excellent agreement for all cases and showed a better fit to the pressure-impulse profiles. It was found that based on LWT, the base pressure was caused by the impact in horizontal direction and the increase in pressure-impulse near the water level by the contribution of the upward velocities.

This page intentionally left blank.

List of Figures

List of Tables

List of Abbreviations

2D	Two-Dimensional
3D	Three-Dimensional
A	Low wave condition
AWAS	Active Wave Absorption System
CFD	Computational Fluid Dynamics
CPU	Computational
DIM	Dimension
DLF	Dynamic Load Factor
DualSPH	DualSPHysics
Dyna	LS-Dyna
E	High wave condition
Exp	Experiment
FEM	Finite Element Method
L	Longer overhang configuration
LWT	Linear Wave Theory
PI	Pressure-Impulse
PS	Pressure Sensor
S	Short overhang configuration
SDOF	Single Degree Of Freedom
SPH	Smoothed Particle Hydrodynamics
SWL	Still water level
WCSPH	Weakly Compressible Smoothed Particle Hydrodynamics
WG	Wave Gauge

List of Symbols

Symbol	Unit	Description
∇	-	Divergence operator
$\alpha_{1,2,3,4}$	-	Parameters Goda
β	$^\circ$	Obliqueness of wave attack
γ	-	Breaker parameter
γ	-	SPH constant
$\delta(x)$		Dirac-delta function
ζ	-	Damping ratio
η	m	Water surface elevation
κ	-	Constant for support domain SPH
μ		Mean value
ξ	-	Irribarren number
ρ	kg/m^3	Water density
σ		Standard deviation
ω	rad/s	Angular frequency
Φ	-	Dynamic amplification factor
a	m	Wave amplitude
c	m/s	Wave celerity
c	Ns/m	Viscous damping coefficient
c_0	m/s	Velocity of sound at reference density
d	m	Water depth
dp	m	Particle size
f	N	External forcing
g	m/s^2	Gravitational constant
h	m	Height water level
h'	m	Water level above foundation
h_0	m	Still water level increase
h_s	m	Smoothing length
i	-	Irrational constant
k	s^{-1}	Wave number
k	N/m	Stiffness
m	kg	Mass
p_0	N/m^2	Pressure at the bed
p_0	N/m^2	Initial pressure before shock
p_1	N/m^2	Pressure at mean water level
p_{wave}	N/mm^2	Wave induced pressure
$\hat{p}_{wave}$	N/mm^2	Amplitude wave induced pressure
t	s	Time

t_a	s	Time after impact
t_b	s	Time before impact
t_d	s	Decay time
t_d, T_d	s	Impact duration
t_r, T_r	s	Rise time
u	m/s	Particle velocity
$\hat{u}$	m/s	Amplitude particle velocity
$x_p(t)$		Displacement function piston
v_0	m/s	Water velocity
y_0	m	Static displacement
z	m	Reference level
B_M	m	Berm width
C_h	-	Smoothing length coefficient
F	N	Force
F_q	N	Quasi-static force
G	m	Gate height
H	m	Wave height
H_b	m	Wave height at breaking
H_i	m	Incoming wave height
I	Ns	Force-impulse
$\overline{I}$	-	Dimensionless force-impulse
I_{im}	Ns	Total impulse force-impulse
K	-	Coefficient impact pressure
L	m	Wave length
L_x	m	Length numerical domain
P	Pa	Pressure
P	$Pa\ s$	Pressure-impulse
$\overline{P}$	-	Dimensionless pressure-impulse
R^2	-	Coefficient of determination
R_c	m	Freeboard
S	m	Piston stroke
T	s	Wave period
U	m/s	Velocity
V	m/s	Velocity
W	m	Overhang width
$W(x)$		Smoothing function

Contents

Chapter 1

Introduction

1.1 Motive

Forces induced by waves is an important factor in the structural design of hydraulic structures. Specifically loads by impulsive waves, i.e. impact with a short duration with extreme peak pressures, can lead to structural failure or local damages. The structural response to wave loads has been the subject in a broad variety of literature, in which (semi)-empirical design formulae have been derived. However, the validity of these formulae are limited and impulsive wave loads are often underestimated (Oumeraci et al., 2001). Numerical models are able to simulate physical behaviour, which could be a powerful tool when analytical formulae fail. Yet, validation of its applications by experimental research is required.

1.1.1 Background

Previous research mainly focused on non-impulsive loads (e.g. Goda (1972), Sainflou (1928)) or impulsive loads caused by breaking waves on vertical walls (e.g. Goda (1972), Takahashi and Hosoyamada (1993), Cuomo et al. 2010, Oumeraci et al. (2001)). However, impact can also be caused by non-breaking standing waves on a structure with an overhang (de Almeida Sousa et al., 2019; Kisacik et al., 2014) as depicted in figure 1.1. Examples of which are steel gates, culverts and defensive overhanging beams in storm surge barriers and locks.

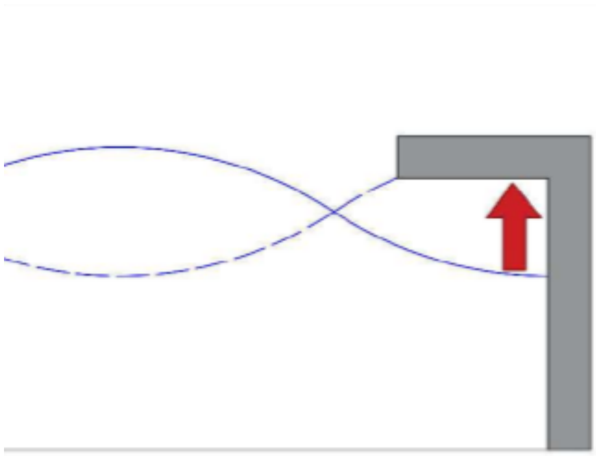

Figure 1.1: Structure with overhang (de Almeida Sousa et al., 2019)

A practical example is the Eastern Scheldt storm surge barrier, built in 1986 as part of the Dutch Deltaworks. Steel gates with large dimensions (42 m long and 12 m high) were constructed to protect against floods during extreme weather conditions (Rijkswaterstaat, 2019). Naturally, these gates have to withstand wave impacts. An impression of the barrier is given in figure 1.2.

Figure 1.2: Eastern Scheldt storm surge barrier (Waternoodsmuseum, 2018)

The design initially consisted of a double plated steel gate with plate girders on the seaward side. This setup was thoroughly tested in scale models, in which the wave impact was studied (Visser, 2003). The forces and pressures measured in the experiments turned out to be so severe, that the dimensions of the frame girders had to be adjusted and one of the plates was removed to prevent wave reflections as the theoretical models strongly underestimated the observed pressures (Korthof, 1982b).

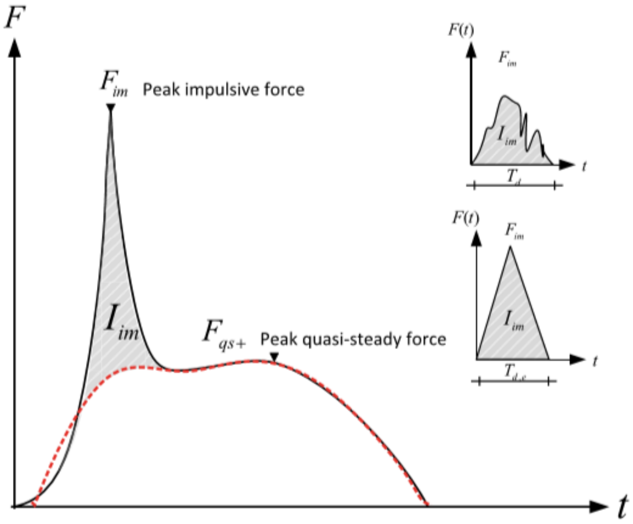

Figure 1.3: Force-time series and integration of force-impulse (Chen et al., 2019)

Instead of using peak pressures or forces, which usually show a great variation in magnitude and occurrence, it is possible to integrate the impulsive pressure time series over the duration of the impact to obtain a so called pressure-impulse, which is a more constant and stable way to represent wave impact than using the peaks (de Almeida Sousa & Hofland, 2020). The force-impulse can be obtained by either direct integration of the force time series in a similar fashion or by integrating the pressure-impulse over the surface area. Figure 1.3 shows a typical force-time series of an impulsive wave and its force-impulse I_{im}, in which a clear distinction is made between the quasi-static (F_{qs}) and impulsive F_{im} parts of the impact with the impact duration denoted as T_d. Chen et al. (2019) proposed a method to translate the force-impulses to reaction forces on hydraulic structures.

To obtain a time series of pressures or forces, it is needed to either conduct physical experiments or perform numerical modelling, which is a time-consuming and expensive method. However, a theoretical pressure-impulse model was developed by Wood and Peregrine (1996), who schematised wave impact on a structure with overhang as a plate being dropped on a water body, similar to Wagner (1932). This model is the subject of research in recent studies (de Almeida Sousa & Hofland, 2020; de Almeida Sousa et al., 2019; Hofland et al., 2019) for the design of hydraulic structures. Another method to obtain force-impulses is proposed by Tuin (2019), in which the basis of wave description is applied, namely linear wave theory (Airy, 1845). In this conceptual model, the impulse is directly obtained by integrating the particle velocities under the overhang by assuming control areas of integration in the two-dimensional (2D) plane, i.e. the total force-impulse consists of both horizontal and upward velocities.

1.1.2 Problem description

A knowledge gap exists when it comes to the validation of aforementioned theoretical models and the numerical modelling of structures with an overhang. Moreover, literature involving calculation of pressure-impulse by wave impact in both horizontal (on the wall) and vertical sense (on the overhang) by numerical models is not available. Furthermore, the performance of the proposed conceptual model and its schematic assumptions are yet to be validated. In this thesis, the knowledge gap is treated by comparing a physical experiment to the numerical and theoretical models.

Traditionally, grid-based finite element and finite volume methods are applied in numerical modelling of wave-structure interaction. However, difficulties arise when complex free surface flows are simulated, like wave breaking and impact. An often overlooked numerical approach was introduced by Gingold and Monaghan (1977), called Smoothed Particle Hydrodynamics (SPH), based on a mesh-free Lagrangian method. The application of SPH to wave loads on coastal structures is scarce, even though promising results are achieved (e.g. Cummins et al., 2012, Dao et al., 2013, Didier et al., 2014 and Yreux, 2018). Few studies are available of SPH modelling of impact waves on coastal structures. In a review of which, three main problems were identified:

1. Only simple vertical walls are considered. More complex geometries like a structure with overhang loaded by standing waves have yet to be studied
2. Only the wave generation or force and pressure-peaks considered. No implementation of pressure-impulse theory
3. Lack of extensive analytical and/or experimental validation

1.2 Research objectives, scope and methodology

The aim is to assess the capabilities of SPH modelling in an analysis of impact loads on simplified vertical walls, as well as a structure with overhang, which is the main focus of this research. A second objective is to analyse the performance of the conceptual model compared to the pressure-impulse model. The objectives are formulated in research questions, after which the scope and methodology are described respectively.

1.2.1 Research objectives and scope

The main objective of this study is derived from the problems as stated in the problem description, which reads:

Numerical and experimental validation of SPH modelling applied to wave impact on a structure with overhang and to validate the existing and newly proposed theoretical models.

Achieving this objective is reached by answering the following research questions:

1. Can SPH accurately predict non-impulsive and impulsive wave loads of non-breaking waves?
2. Can SPH be used to calculate the force-impulse on a structure with overhang?
3. How do the results of the theoretical models for a structure with overhang compare to SPH?

In answering these questions, some simplifications are made. Firstly, only 2D models are considered, as SPH is computationally intensive. Secondly, air is disregarded in the numerical model. Thirdly and finally, the structural response to the wave loading is out of the scope of this study and is modelled as fully rigid.

1.2.2 Methodology

To find the answers to the three research questions, the following methodology is applied:

- *Understand the mechanics of impulsive wave impact*
  A literature study is conducted to gain insight into the descriptions of wave loads. A classification of wave types is given and an overview of the influencing factors on the resulting forces. The translation to structural design is made, by identifying applicable theoretical models, including a new conceptual model

- *Finding relevant experimental data*
  Experimental research is conducted in the wave flume of the Delft University of Technology for a structure with overhang, performed by de Almeida Sousa et al. (2019). These results are shared with the author of this thesis

- *Numerical modelling of the experimental setup*
  Physical setup is reconstructed as an SPH model and optimised by exploring limitations and the sensitivity of the numerical parameters as visualised as a flow chart depicted in figure 1.4

- *Compare numerical and theoretical results*
  The performance of the model is compared and analysed in terms of wave generation, pressures and pressure-impulses for both the wall and overhang. In addition, the velocity fields at impact are analysed and compared to the assumptions in the theoretical models

- *Validate theoretical models with numerical and experimental results*
  The analytical formulae and theoretical models found in the literature study are compared to the physical and numerical results

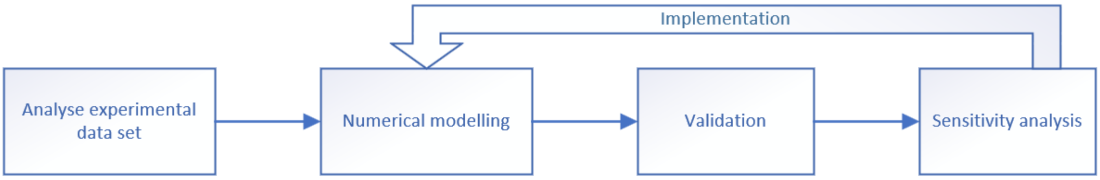

Figure 1.4: Methodology research

1.3 Research outline

Chapter 2 starts with the theoretical background of wave impact, divided in the categories non-impulsive and impulsive wave loads. Furthermore, an in depth decomposition of the theoretical models for a structure with overhang is provided.

Chapter 3 includes the methodology and mathematical background of the SPH method. Thereafter, a literature review is conducted of SPH applied to wavs loads on hydraulic structures

Chapter 4 gives a description of the physical model and the applied overhang configurations and wave conditions, after which the observed wave impact is explained

Chapter 5 provides an overview of the numerical tools used in this thesis and their limitations, after which the setup of the numerical models is elaborated. A sensitivity study is performed to optimise the numerical models

Chapter 6 treats the results of the SPH models and compares them to the experiment. The method of impulse calculation is elaborated after which the numerical and experimental pressure-impulse profiles are given. Furthermore, an analysis of the velocity fields is carried out and the findings compared to the assumptions in the theoretical models. Based on SPH, modifications are proposed to the conceptual model

Chapter 7 provides a full analytical analysis of the cases with and without overhang. The dimensionless pressure-impulse profiles and force-impulses are calculated and compared to SPH and the experiment. Modifications to the conceptual model proposed in chapter 6 are validated

Chapter 8 concludes the thesis by summarising and discussing the results, before drawing the conclusions. Recommendations are given for further study

Chapter 2

Theoretical background

This chapter describes the types the theoretical background of wave loading on vertical walls. Applicable design formulae used in practice are stated, after which the influence of aeration and the dynamic structural response are explained. Furthermore, a practical case of a steel gate is treated. Finally, the theoretical models for overhangs are derived.

2.1 Classification of wave types

The wave forcing in the static and dynamic loading of hydraulic structures is of major importance in the design of the structural elements. The type of loading is dependent on the wave type that strikes the vertical wall. In general, a distinction is made between three wave types (CERC, 1984):

1. **Non-breaking waves**
   Usually approximated as quasi-static. Load reflective vertical walls in the shape of a standing wave and can lead to impact in confined spaces
2. **Breaking waves**
   Waves in the process of breaking leading to wave impact
3. **Broken waves**
   Waves after breaking resulting in a turbulent mass of water causing impact

Oumeraci et al. (2001) extended the classification adding **slightly breaking waves**, the phase between non-breaking and fully breaking waves. The normalised force-time diagrams per wave type are giving in figure 2.1, in which the standing wave represents the non-broken wave and the plunging breaker the worst case scenario of a breaking wave (further elaborated in section 2.4). Oumeraci et al. (2001) implemented the wave types in a parameter map, which indicates what wave class is most likely to occur in front of a vertical breakwater in terms of the wave height, water depth and berm width B. TAW (2003) adopted the theory and applies the parameter map to determine the wave type with its applicable design formula for Dutch water retaining structures.

In the classification, a distinction is made between impact (impulsive) and non-impacting loads. For example, non-breaking waves on a vertical wall cause a pulsating quasi-static load without impact, i.e. no peaks will be observed in the pressure or force distribution like figure 2.1a. However, even non-breaking waves can cause impact loads when the geometry is not a simple vertical wall, but e.g. a structure with an overhang in which the particle velocities are suddenly stopped in upward direction. The force distributions for the above mentioned wave classes without overhang are observed to be like figure 2.1c.

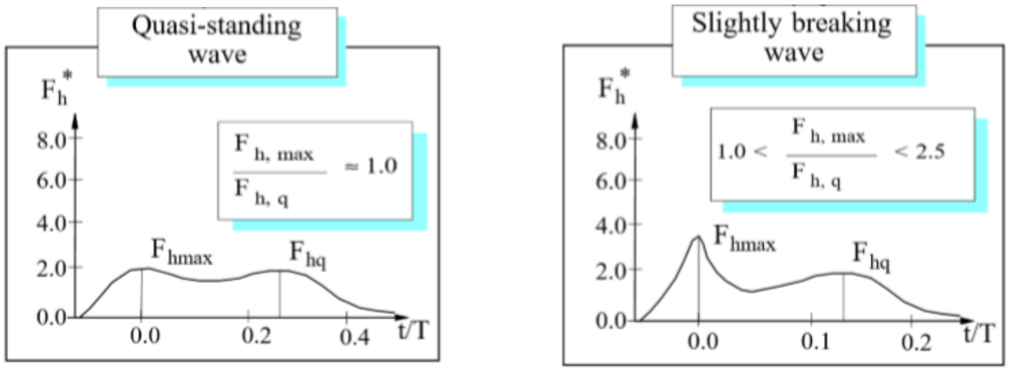

(a) Non-breaking wave loads

(b) Slightly breaking wave loads

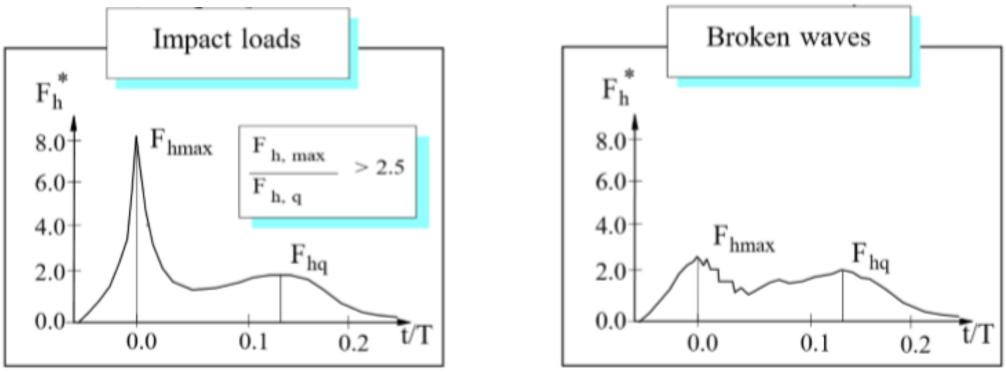

(c) Impact (breaking) wave loads

(d) Broken wave loads

Figure 2.1: Force/time diagrams per wave impact type (Oumeraci et al., 2001)

2.2 Physics of wave breaking

To be able to predict what type of wave hits the structure, it is needed to understand the underlying mechanism of wave breaking. Principally, a wave breaks when the water particle velocity exceeds the wave celerity. The profile of the wave becomes pitched forward until complete breaking occurs, leading to turbulent energy dissipation (Schiereck & Verhagen, 2012). The driving factor of wave breaking is the steepness of the wave, described as the wave height over the wavelength (parameter H/L). This can occur in deep water in the form of white-capping, which is not in the scope of this research, and in shallow water in the form of depth induced breaking.

The wave height limit is described by Miche (1944), who proposed the following general criterion:

$$H_b = 0.142\, L \tanh\left(\frac{2\pi}{L} h\right) \tag{2.1}$$

In which:				
	H_b	=	wave height at breaking	[m]
	h	=	water depth	[m]
	L	=	wavelength	[m]

For deep water, this reduces to $H_b/L = 0.142$. For shallow water, two values are given in literature, namely $\gamma = H_b/h = 0.88$ and, using solitary wave theory, $\gamma = 0.78$ (Holthuijsen, 2007). On a sloped bathymetry or berm, the angle of the slope directly influences the manner in which the wave breaks and thus the magnitude of impact. A dimensionless parameter is introduced named the Irribarren number (Schiereck & Verhagen, 2012), given in 2.2, that describes the wave steepness and slope angle relative to each other.

$$\xi = \frac{\tan\alpha}{\sqrt{H/L_0}} \tag{2.2}$$

In which:
α = angle of slope [°]
H = wave height [m]
L_0 = deep water wavelength [m]

The value of the constant ξ indicates the type of wave breaking, e.g. a value of 0.5-2 results in a plunging breaker with the highest impact (Battjes, 1974). The point of breaking lies around a value of 2.5-3. It should be noted that the transition between various breaker types is gradual and the constant ξ is just an indication.

2.3 Non-impacting wave loads

2.3.1 Linear wave theory

Linear wave theory is considered to be the basis of the mathematical description of coastal waves, firstly introduced by Airy (Airy wave theory (Airy, 1845)). The theory is derived from the linearised mass balance and momentum balance equations and neglects all external forces, such as bed friction and advection, besides the gravitational force. A result of the linearisation is a freely propagating, independent harmonic wave in its simplest form:

$$\eta(x,t) = a\sin(\omega t - kx) \quad \text{with} \quad \omega = \frac{2\pi}{T},\ k = \frac{2\pi}{L} \tag{2.3}$$

In which:
a = Wave amplitude [m]
ω = Angular frequency [rad/s]
k = Wave number [s^{-1}]
T = Wave period [s]

However, the amplitudes of the waves should be small in relation to the wave length and the water depth before the theory can be applied. It should be noted that the water is assumed to be incompressible, to have no viscosity, a constant density and the water particles are assumed to be irrational. Moreover, the waterbody is assumed to be continuous, which leads to the fact that the idealisation is only applicable to non-breaking waves, since air bubbles in breaking waves lead to discontinuities in the waterbody.

According to this theory, the forcing over the vertical plane can be explained by integration over the wave-induced pressures. In case of linear waves, Holthuijsen (2007) states that the analytical expression for wave induced pressure is given by:

$$p_{wave} = \hat{p}_{wave}\sin(\omega t - kx) \quad \text{with} \quad \hat{p}_{wave} = \rho g a \frac{\cosh[k(d+z)]}{\cosh(kd)} \tag{2.4}$$

In which:
p_{wave} = Wave induced pressure [N/mm^2]
$\hat{p}_{wave}$ = Amplitude of wave induced pressure [N/mm^2]
ρ = Water density [kg/m^3]
g = Gravitational constant [m/s^2]
d = Water depth [m]
z = Reference level [m]

The propagating pressure wave is valid for the small-amplitude approximation and can be superimposed with the hydrostatic pressure. However, real waves have a finite amplitude which makes the theory invalid near the surface. Above the waterline, the pressure can be roughly approximated as hydrostatic, as illustrated in figure 2.2.

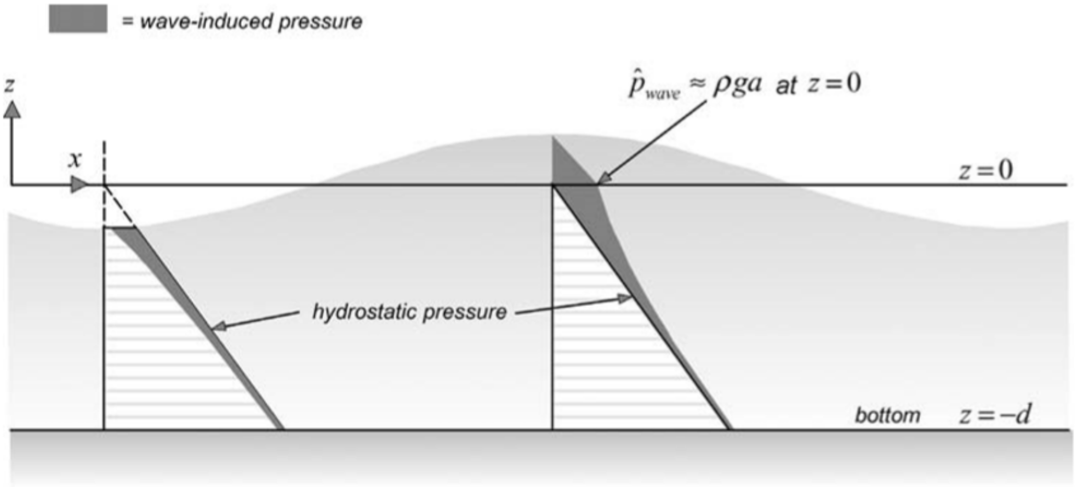

Figure 2.2: Wave induced pressures superimposed on the hydrostatic pressure (Holthuijsen, 2007)

The water particles in a propagating wave move either circular at the water surface elevation or elliptical closer to the bottom. The velocity of the particles is an important factor in the calculation of impulses on a structure and can be found by using equations 2.5 and 2.6.

$$u_x = \hat{u}_x \sin(\omega t - kx) \quad \text{with} \quad \hat{u}_x = \omega a \frac{\cosh[k(d+z)]}{\sinh(kd)} \tag{2.5}$$

$$u_z = \hat{u}_z \cos(\omega t - kx) \quad \text{with} \quad \hat{u}_z = \omega a \frac{\sinh[k(d+z)]}{\sinh(kd)} \tag{2.6}$$

When interaction occurs between the wave motion and a vertical wall, there will be reflection to a certain degree of the incident wave. In case of full reflection, i.e. 100%, a standing wave occurs with double the amplitude of the incident harmonic wave as described in equation 2.3. Using superposition with a reflective wave with an amplitude equal to the incident one (a_i) results in the surface elevation as given in equation 2.7.

$$\eta(x,t) = 2a_i \cos(kx) \sin(\omega t) \tag{2.7}$$

Subsequently, the wave height at the wall is twice the incoming wave height, also denoted as $H = 2H_i$. This principle is used for design formulae for non-breaking waves using linear wave theory. The occurring pressure distribution is sketched in figure 2.3.

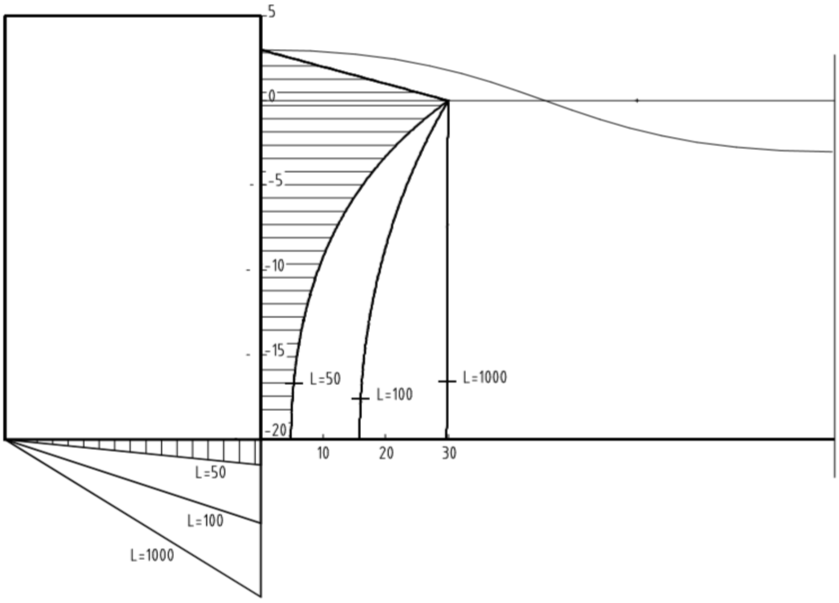

Figure 2.3: Pressure distribution according to LWT (Molenaar & Voorendt, 2016)

The total force can then be calculated by integration of the pressure field:

$$F = \int_{-d}^{0} \rho g H_i \frac{\cosh(k(d+z))}{\cosh(kd)} dz + \int_{0}^{h} \left(1 - \frac{z}{H_i}\right) \rho g H_i dz \tag{2.8}$$

It is evident that the wave pressure can be approximated by the hydrostatic pressure for large wavelengths as shown in figure 2.3 for $L = 1000$. In that case, a conservative upper limit can be given by treating the wave pressure as a static load:

$$F_{max} = \frac{1}{2} \rho g H_i^2 + d \rho g H_i \tag{2.9}$$

2.3.2 Design formulae for non-breaking waves on vertical walls

When the steepness of waves increases the linear wave theory is not valid anymore, because the waves become non-linear. For a mild steepness increase, the wave signal can be corrected by higher order terms (Stokes, 1847). A typical second order stokes' wave is characterised by a steep peak and flattened trough. These wave kinematics are used by the design formula by Sainflou (Sainflou, 1928) and can be used for slightly steeper than linear waves. In this formula, a full reflection is assumed and the pressure acting on the bottom is taken to be linear with the pressure at the top of the wall. However. this leads to an overestimation of the total load when the waves are too steep. The pressure distribution is displayed in figure 2.4.

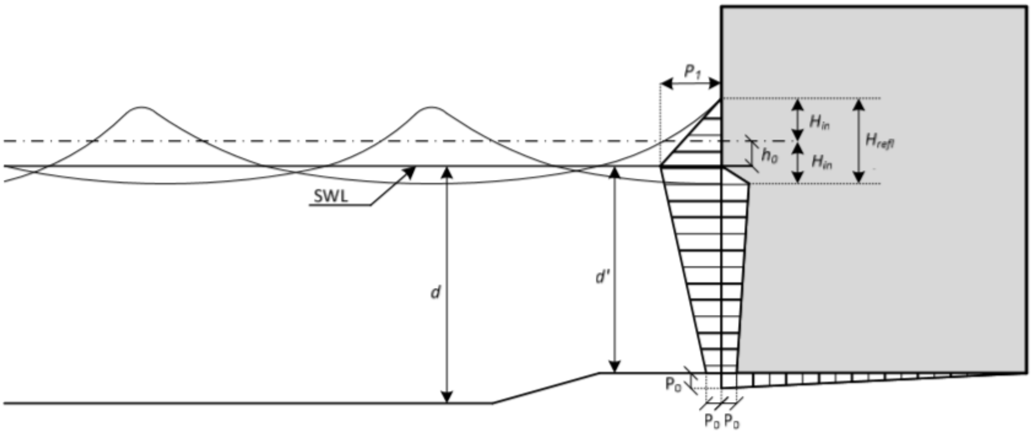

Figure 2.4: Pressure distribution according to Sainflou (TAW, 2003)

The still water level increase is calculated by (TAW, 2003):

$$h_0 = \frac{1}{2} k a_i^2 \coth(kh) \tag{2.10}$$

The parameters p_0 and p_1 are equal to:

$$p_0 = \frac{\rho g a_i}{\cosh(kh')} \quad \text{and} \quad p_1 = \rho g (a_i + h_0) \tag{2.11}$$

In which: p_0 = Pressure at the bed [N/m^2]
p_1 = Pressure at mean water level [N/m^2]
a_i = Half of reflected wave height [m]
h' = Water depth above foundation level [m]

A more modern and widely used design formula for non-breaking (and breaking) waves is developed by Goda (1972). These equations are mainly derived by empirical research. Again, complete reflection is assumed, similar to Sainflou (1928). The formulae were originally applicable to breakwaters on rubble mound sills. Nevertheless, they can be used for water retaining structures without sills as well for non-breaking waves. Tanimoto et al. (1976) improved the theory by adding obliqueness of wave attack. TAW (2003) presents the pressure distribution as illustrated in figure 2.5 with the corresponding pressures given in equation 2.12.

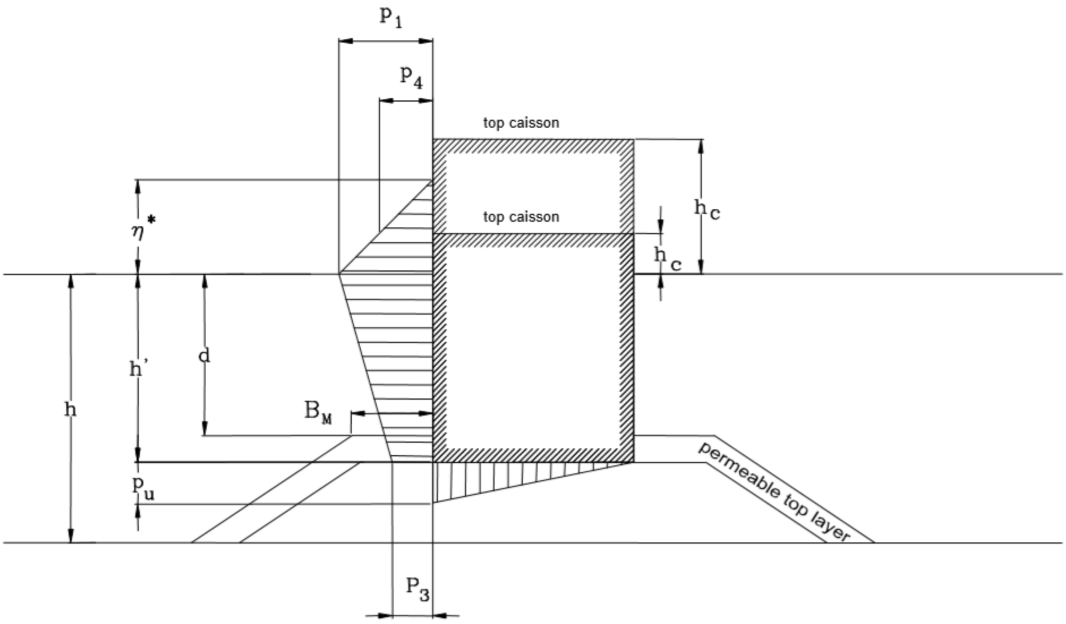

Figure 2.5: Pressure distribution according to Goda (TAW, 2003)

$$
\begin{aligned}
p_1 &= 0.5(1+\cos(\beta))(\lambda_1\alpha_1 + \lambda_2\alpha_2\cos(\beta)^2\rho g H_D \\
p_3 &= \alpha_3 p_1 \\
p_4 &= \alpha_4 p_1 \\
p_u &= 0.5(1+\cos(\beta))\lambda_3\,\alpha_1\,\alpha_3\,\rho g H_D
\end{aligned}
\tag{2.12}
$$

In which:

β = angle incoming wave [°]

$\eta^* = 0.75(1+\cos(\beta))\lambda_1 H_D$ [m]

$\alpha_1 = 0.6 + 0.5\left(\frac{4\pi/L_D}{\sinh(4\pi h/L_D)}\right)^2$ [-]

$\alpha_2 = \min\left(\frac{(1-d/h_b)(H_D/d)^2}{3}, \frac{2d}{H_D}\right)$ [-]

$\alpha_3 = 1-(h'/h)\left(1-\frac{1}{\cosh(2\pi h/L_D)}\right)$ [-]

$\alpha_4 = 1-\frac{h_c^*}{\eta^*}$ [-]

$h_c^* = \min(\eta^*, h_c)$ [m]

$\lambda_{1,2,3}$ = factors based on geometry and wave conditions [-]

h_b = water depth measured at distance $5H_D$ from wall [m]

H_D= design wave height [m]

L_D= design wavelength [m]

d = water depth above top of sill [m]

h' = water depth above foundation [m]

h = water depth in front of sill [m]

B_m= width of berm [m]

2.4 Impulsive impact wave loads

The most violent wave loads on a vertical wall are usually caused by breaking waves, i.e. the wave is in the process of breaking when it hits the obstacle. This leads to high local pressures with an almost instantaneous development. However, wave impact can also occur for non-breaking waves in a confined space. Various models and design formulae are found in literature, which are described in this section.

2.4.1 General description wave impact

A wave impact is defined as the sudden blockage of free water motion. The momentum of the incident wave will transfer into pressures on the subjected obstacle. The magnitude of the load is influenced by the compressibility of the water itself and the air pockets, described in detail in section 2.4.3.

The initial impact pressure at the instant of collision results in a peak pressure. The rise time of this pressure, defined as the time it takes for the peak to develop, is in the order of milliseconds. Subsequently, the peak abruptly drops (decay time) to a more or less constant load, defined as the quasi-hydrostatic load (Kolkman & Jongeling, 2007). The church-roof model is a common parametric representation of wave impact loads, displayed in figure 2.6a and further simplified in figure 2.6b in which t_r =rise time, t_d =decay time, F_p = peak load and F_q = quasi-hydrostatic load.

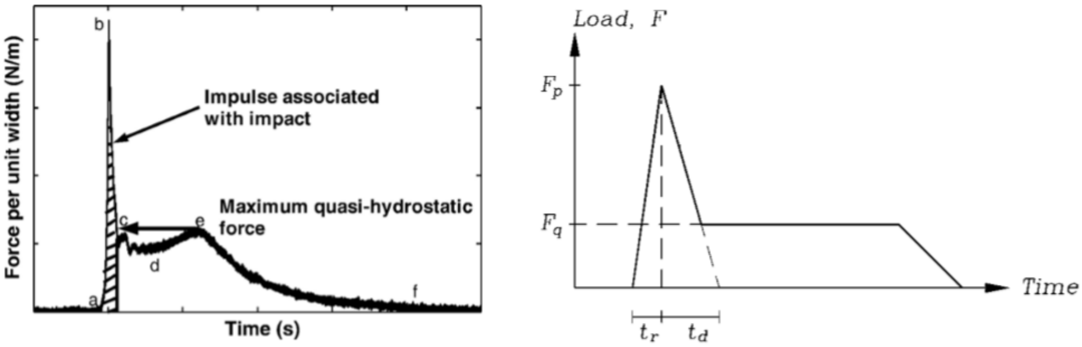

(a) Church-roof model

(b) Simplified church-roof model

Figure 2.6: Church-roof model of wave impact (Bullock et al., 2007; Burcharth, 2003)

The area under the triangular shaped peak is the total impulse load. The horizontal part represents the quasi-hydrostatic load, which remains after the impact.

2.4.2 Wave impact models

Following the work by Lundgren (1969), the impact of waves is described in three mechanisms, namely the ventilated shock, the compression shock and the hammer shock.

When a wave front collides with a vertical wall and (nearly) all the entrapped air can escape, it is called a **ventilated shock**, also referred to as the Wagner type (Wagner, 1932). Figure 2.7a gives an impression of the wave front.

The inclination of the wave front allows the air to escape either vertically upwards or longitudinally.

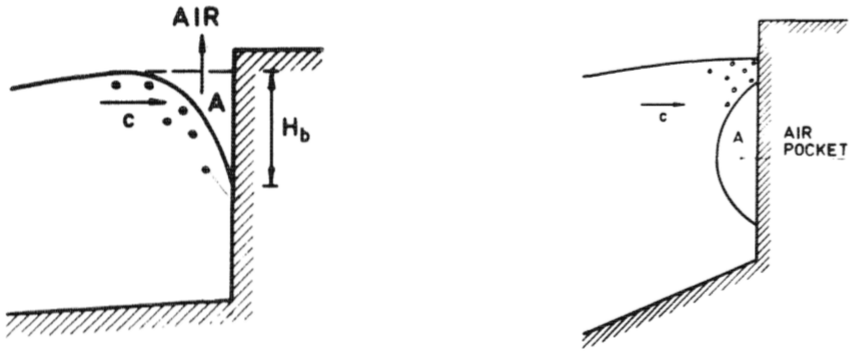

(a) Impression ventilated shock (b) Impression of plunging breaker

Figure 2.7: Impressions of a ventilated shock and plunging breaker

The simplest applicable mathematical model of a ventilated shock is called the flow-pressure model and described in equation 2.13 (Kolkman & Jongeling, 2007).

$$p_{max} - p_0 = K \, (\frac{1}{2} \, \rho \, v_0^2) \tag{2.13}$$

In which: p_{max} = maximum pressure [N/m^2]
p_0 = Pressure in water before shock [N/m^2]
v_0 = Incoming water velocity [m/s]
K = coefficient for magnitude impact pressure [-]

When a breaking (plunging) wave entraps a large volume of air, the wave can be described using a combination of the compression shock and the hammer shock models. An impression of a plunging breaker is given in figure 2.7b.

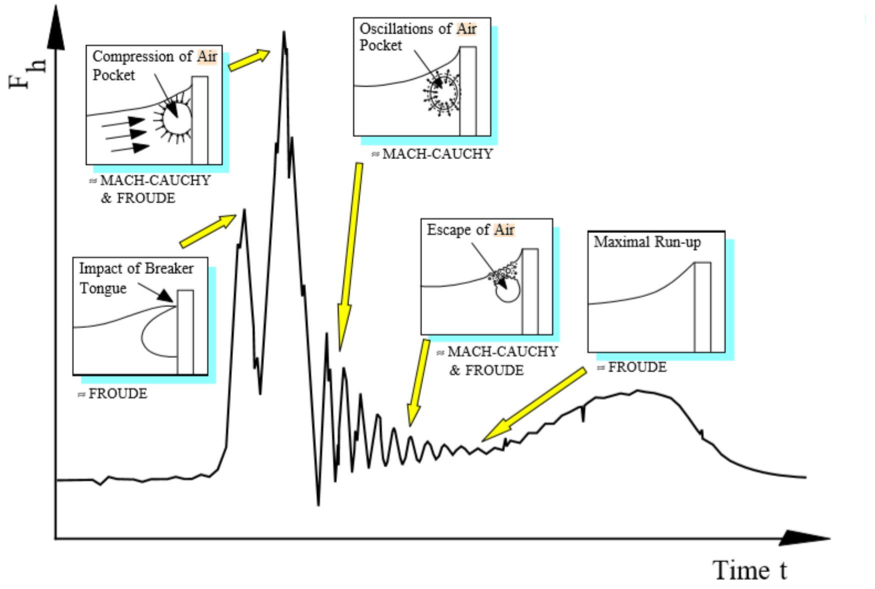

Figure 2.8: Pressure evolution plunging breaker (Oumeraci et al., 2001)

Two main phases of the impact can be distinguished. Firstly, the crest of the wave hits the wall causing a large initial peak in the force distribution, as shown in figure 2.8. This is called the **hammer shock**. Secondly, the air pocket will be compressed causing the second peak, named the **compression shock**. Which peak is the extreme value cannot be established with certainty and differs in observations found in literature (Burcharth, 2003; Oumeraci et al., 2001). Oscillations in the pressure distribution are observed after the second peak, since the air bubbles will oscillate with a natural period. The period between the initial and secondary peak is determined by the size of the air pocket. For large air pockets, the spacing is in the range of tenths of a second. For small air pockets, this is closer to hundredths of a second. This type of wave is referred to as the Bagnold type (Bagnold, 1939), who was the first to observe this behaviour.

A variant of the hammer shock occurs when the wave becomes so steep that the crest and the trough hit the wall simultaneously. This means that there is no air entrapment and that the pressure build-up will be determined by the compressibility of the water and rigidity of the structure. In that specific case, an extremely short rise time and a single extreme pressure peak are observed. However, this type is rare and affects a limited part of the surface area only (Hofland et al., 2010). Cooker and Peregrine (1990) described this type of wave loading as "flip-through" impact, which is illustrated in figure 2.9. The pressure evolution is closely related to that of a ventilated shock with one extreme peak and few oscillations in the hydrostatic part, further explained in section 2.4.3.

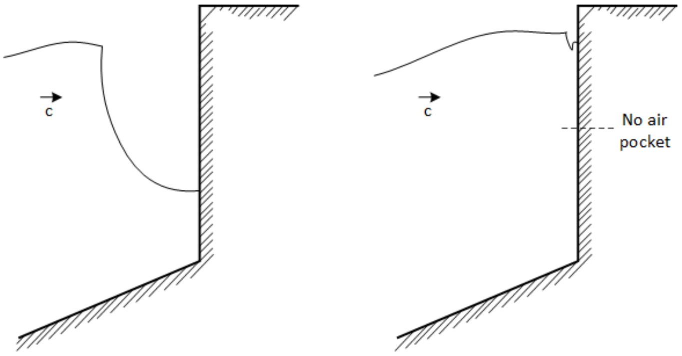

Figure 2.9: Impression of flip-through impact

An upper limit of the peak force on a rigid wall for hammer shock is given by Karman (1929):

$$p_{max} = \rho\, u\, c_e \tag{2.14}$$

In which: u = water velocity [m/s]
c_e = velocity of sound in the water body [m/s]

In reality, this upper limit is only theoretical and could not be reached, due to the compressibility of water, entrapped air and the elastic response of the structure.

In this study, a structure with overhang is considered loaded by non-breaking waves. For this, different physical behaviour is observed as the impact occurs vertically. Therefore, it is opted for a more general approach by classifying the impact by the amount of entrapped air (low and highly aerated impact). This is further explained in the following subsection.

2.4.3 Influence of aeration

As stated, the level of air entrapment is directly correlated with the magnitude and distribution of the pressure field. A higher level of aeration reduces the impact pressure of the wave. This is confirmed by Bullock et al. (2007) and Hofland et al. (2010), who showed this in physical model tests. The air pockets result in a cushioning effect, lowering the pressure peak significantly. This is schematised in figure 2.10.

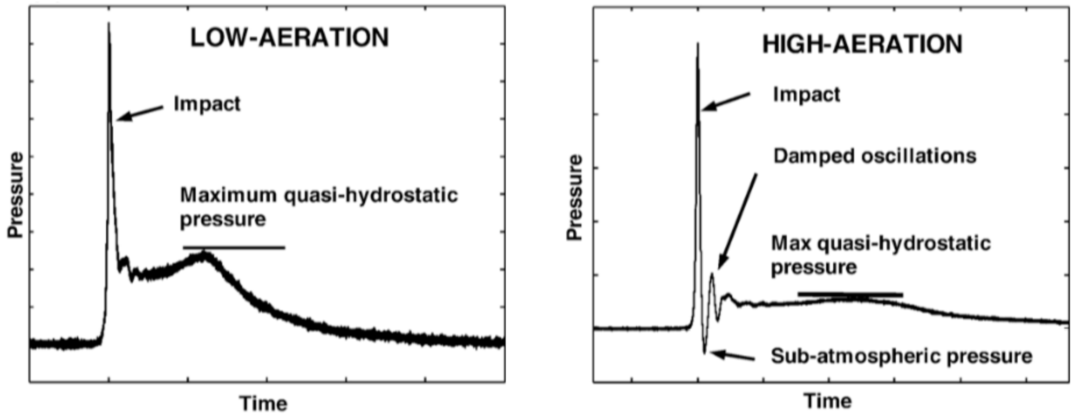

(a) Pressure distribution low-aeration impact (b) Pressure distribution high-aeration impact

Figure 2.10: Influence of aeration on pressure distributions impulsive impact (Bullock et al., 2007)

Clearly, a high-aeration impact has a lower peak and far more oscillations due to the dampening effect of the air pocket. However, the rise time is greater for a high-aeration impact as well. As Hofland et al. (2010) and Bullock et al. (2007) have proven, the low-aerated impact has little spatial and temporal variation. Thus, integrating the pressures including the shorter duration of the impact may result in comparable impulse forces as high-aerated impacts with a longer duration. Therefore, it must be stated that the cushioning effect of higher aeration levels is not naturally a dominant factor in determining the total impact force, though important for the dynamic behaviour of the structure and local damages. Flip-through impact results in the highest peak pressures in all cases, yet having the lowest probability of occurrence and impact duration, whilst high-aeration impact wave occur often. Mai et al. (2019) extended the research by conducting experiments with slightly breaking waves, high-aeration impact, flip-through impact and broken wave impact. Again, it was shown that low-aerated wave impact and flip-through impact resulted in the most severe pressures.

To conclude, it is found that impuslive wave impact can be subdivided in two main categories: **Low aerated impact** and **High aerated impact**. The former with small to none entrapped air pockets result in the most extreme pressures with the lowest impact duration. On the contrary, the latter results in smaller pressure peaks due to cushioning effects, but act over a longer duration. Therefore, both types can result in similar impulses, when the pressures and forces and integrated over the duration.

2.4.4 Dynamic response to impact loads

A large impact on a structure induces a dynamic response, depending on the properties of the impact, such as magnitude and duration of the load and the structural properties of the structure, such as mass (+added water mass), elastic stiffness and damping. During impact, natural movements of the structure are hit resulting in decaying vibrations (Kolkman & Jongeling, 2007). Even though a vertical wall like a lock gate has many degrees of freedom, it may be modelled as a single degree of freedom (SDOF) mass-spring system (figure 2.11) to capture the impulse of the wave impact:

$$m\frac{d^2y}{dt^2} + c\frac{dy}{dt} + ky = f(t) \tag{2.15}$$

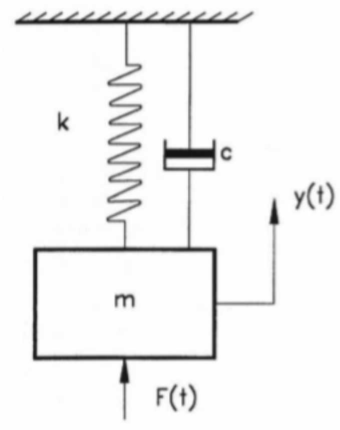

Figure 2.11: SDOF mass-spring system (Jongeling & Erdbrink, 2010)

In which:				
	m	=	mass	[kg]
	c	=	viscous damping coefficient	[Ns/m]
	k	=	stiffness	[N/m]
	f	=	external force	[N]

The solution to an impulse load is generally given in the form of Duhamel's integral:

$$y(t) = \frac{1}{m\omega_1}\int_0^t f(\tau)e^{-\zeta\omega_0(t-\tau)}\sin\left(\omega_1(t-\tau)\right)d\tau \tag{2.16}$$

In which:
$\omega_0 = \sqrt{k/m}$
$\zeta = c/\left(2\sqrt{km}\right)$
$\omega_1 = \omega_0\sqrt{1-\zeta^2}$

Straightforwardly, the triangular impulse load of the church-roof model can be described mathematically and substituted in the Duhamel integral. The dynamic effect becomes clear when defining a dynamic amplification factor (DLF) assuming an undamped system, given by (Cuomo & Allsop, 2005):

$$\Phi = \frac{y(t)_{max}}{y_0} \quad \text{with} \quad y_o = \frac{F(t)_{max}}{k} \tag{2.17}$$

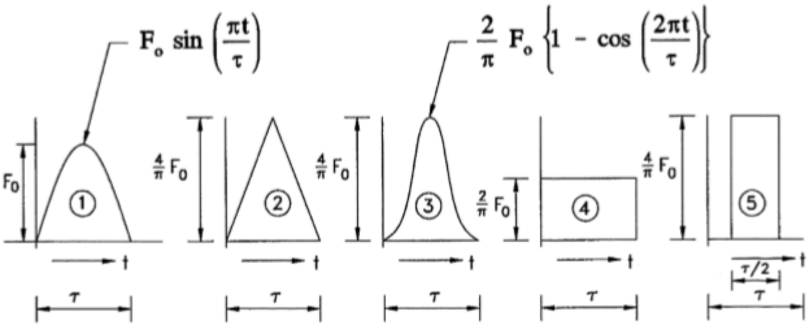

(a) Various impulse load paths

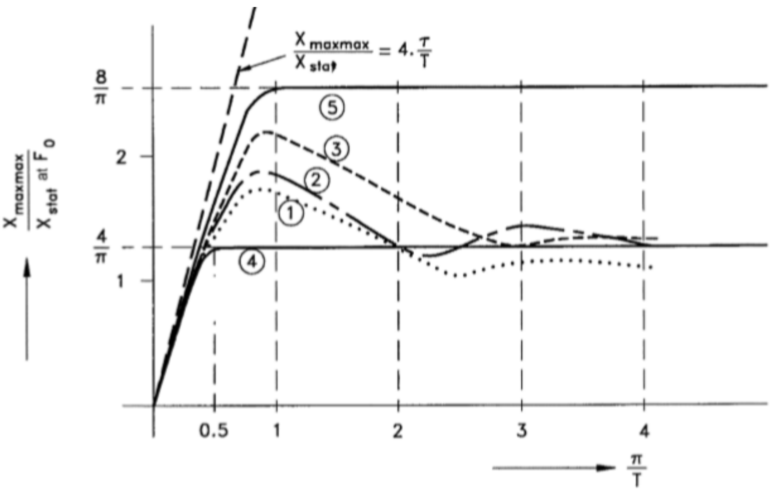

(b) Dynamic amplification factor

Figure 2.12: Dynamic amplification factor for various impulse loads (Kolkman & Jongeling, 2007)

This factor describes the ratio between the maximum displacement y_{max} and the displacement as a result of when the same load is applied statically (y_0). Kolkman and Jongeling (2007) presented the DLF for various impulse loads as illustrated in figure 2.12.

The DLF does not exceed a value of 2 for an undamped system, which act as an upper limit. When the rise time of an impact is short, it is found to be unfavourable for relatively stiff systems. Moreover, the response of a stiff system does not noticeably influence the impact pressures. In any case, the dynamic elastic or elasto-plastic response of the system should be taken into account depending on what failure mechanisms occurs.

In this thesis, impulsive wave impact is regarded with a very short duration. Chen et al. (2019) described the region in which a dynamic analysis is required by stating a relation between the impact duration (T_d) and natural frequency (T_n) of the structure, as illustrated in figure 2.13a, in which the response function (reaction force F_r over impulsive force F_{im}, i.e. the DLF) of the SDOF system to a triangular load is plotted similar to figure 2.12b. After a ratio of $T_n/T_d = 0.25$, a dynamic analysis is required.

Figure 2.13b shows the response function when the DLF is modified by replacing the impulsive force by the force-impulse (I_{im}) multiplied by the natural frequency (ω_n). Interestingly, it can be observed that the response function is overlapping for all values of α, which expresses the ratio of the rise time (T_r) over the impact duration. This means that

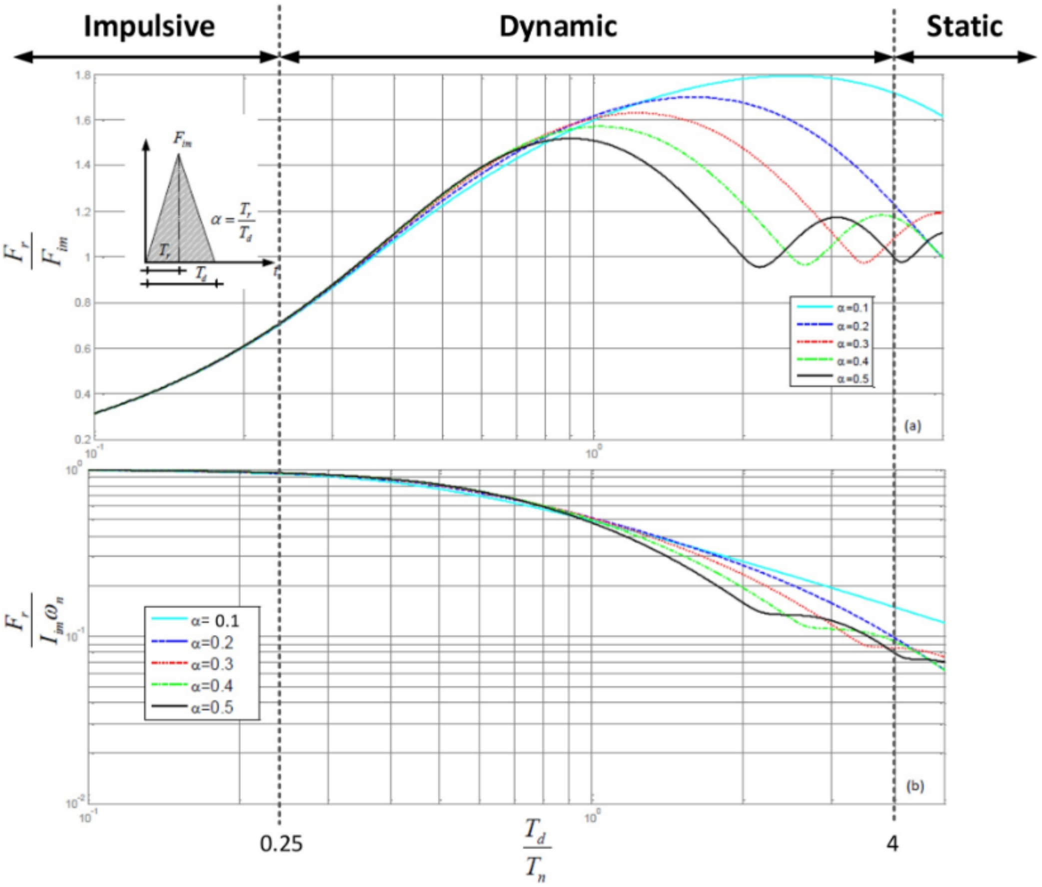

Figure 2.13: Response function as a relation of impact duration and natural frequency of the structure Chen et al. (2019)

the duration and shape of the force peak is not of importance in the impulsive domain, which is a benefit in determining the reaction forces as the impact duration is difficult to obtain. After a value of $T_d/T_n = 4$, the duration of the load becomes so large that a static analysis has to be applied.

Force-impulses can be used to determine the reaction forces on the structure instead of using peak forces. The translation of impulses to a total reaction force ($F_{tot,r}$) can be done by combining the quasi-static force F_{qs+}, the force-impulse, the natural frequency of the structure and the modified DLF (DLF_I) to a design load for the triangular shaped impulse in accordance with Kolkman and Jongeling (2007) for the impulsive load condition, resulting in equation 2.18. Note that dt describes the impact duration T_d.

$$F_{tot,r} = F_{qs+} + I_{im}\,\omega_n\,DLF_I \qquad \text{with} \qquad I_{im} = \frac{1}{2}F dt \tag{2.18}$$

2.5 Wave-induced forces on a structure with overhang

Previous research was mainly focused vertical walls subjected by either impulsive or non-impulsive wave loads. The former is extensively studied by e.g. Cuomo and Allsop (2005), Goda (1972), Minikin (1963), Oumeraci et al. (2001), Takahashi and Hosoyamada (1993) and Cuomo et al. (2010). An overview of the widely used design formulas for breaking wave loads is given in appendix A. When waves encounter structures such as steel gates, the geometry is not a simple vertical wall anymore. The webs and flanges in a gate structure entrap waves and air pockets. Furthermore, lock, sluice and storm surge barrier gates sometimes contain a defensive overhanging beam on which impulsive impact is expected. A practical case is considered in subsection 2.5.1, in which wave impact strongly altered the design choices. In general, impacts on horizontal planes are closely related to impacts on vertical planes and can be described using the models in section 2.4.2.

2.5.1 Practical case: Eastern Scheldt barrier

Korthof (1982a) conducted experimental research on the Eastern Scheldt storm surge barrier for the design of the gate. The gate consisted of steel frame girders connected to a steel plate with a concrete beam. A distinction was made between two types of wave loading as illustrated in figure 2.14, which were frequently observed.

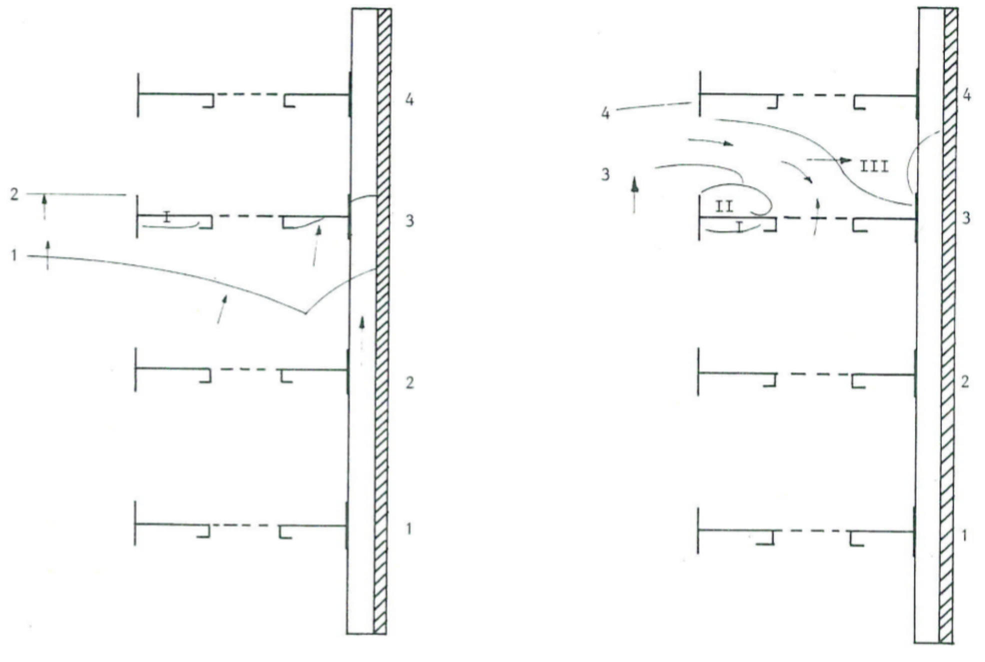

(a) Type 1 impact on steel gate (b) Type 2 impact on steel gate

Figure 2.14: Types of impact on gate (Korthof, 1982a)

A **type 1 impact** (figure 2.14a) is generated by the rise of the still water level induced by the incoming wave, which then hits the bottom of the steel girder. The upward moving water is directly stopped by the girder, resulting in an impact type pressure, analogously to an impulse load on a vertical plane. During this impact, an air pocket arises between the wave, girder and plate.

A type 2 impact happens immediately after a type 1 impact when the top of the wave front dives into the space between the frame girders, leading to downward vertical impact pressures on the girder and horizontal impact pressures on the plate. The overflowing wave has a high velocity and causes a upward jet, slamming against the girder situated above. During the impact, air is entrapped in two places: right after the flange, indicated as II in figure 2.14b and in front of the plate at the point where the upward jet and the overflowing wave front meet, indicated as III. In both type 1 and type 2, the water is highly aerated.

Important to notice is that the highest wave impact was recorded locally and not over the whole length of the gate. There, the measured peak pressures reached values of 2.5 times the design conditions. It was observed that a type 1 impact against the underside of the girder resulted in the highest pressures. This type of impact is attempted to be reproduced by smoothed-particle hydrodynamic modelling.

In this thesis, only the wave loads above the waterline are considered. Under the waterline, loads are mostly current-driven, of which the magnitude is an uncertainty in the design of water retaining steel gates. A typically applied formula is the Morison equation (Morison, 1950), which is out of the scope of this research.

The above mentioned problem can be schematised by a vertical wall with an overhang. Previous research for this configuration based on experimental tests is conducted by e.g. Kisacik et al. (2014) for breaking waves. However, when this type of configuration is encountered by non-breaking waves, there is not only a quasi-static load, but an impact load as well. Figure 2.15 depicts the situation with and without overhang.

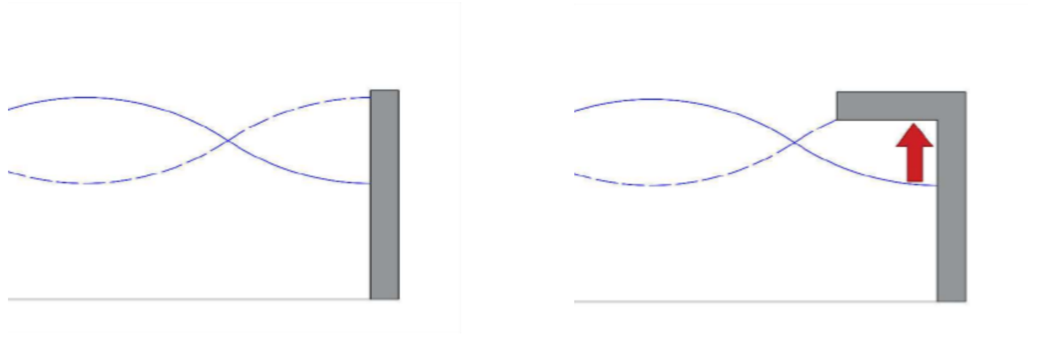

(a) Quasi-static: No overhang

(b) Quasi-static + impulsive: With overhang

Figure 2.15: Schematised configurations with and without overhang (de Almeida Sousa et al., 2019)

2.5.2 Theoretical model: Pressure-Impulse

Pressure peaks caused by wave impact show a lot variation depending on the level of air entrapment. By integrating the pressure over the impact duration, the pressure-impulse can be calculated, which is observed to be a more stable and consistent factor (Bagnold, 1939; de Almeida Sousa & Hofland, 2020). This phenomenon is used as the basis for the theoretical models. The pressure-impulse P is defined as the integral of the impact duration, which is defined as the difference of the points in time before (t_b) and after (t_a) the impact, as stated in equation 2.19.

$$P(x) = \int_{t_b}^{t_a} p(x,t)dt \tag{2.19}$$

Cooker and Peregrine (1990, 1995) developed a theoretical model, called the pressure-impulse model, based on this definition. The Navier-Stokes equation is used as the basis for the theory, which is known as the general equation of motion for fluids (Bistafa, 2018). Equation 2.20 shows the Navier-Stokes equation for incompressible fluids, as assumed in the pressure-impulse theory. The first term describes the change in velocity, i.e. the local acceleration, in terms of the particle velocity u. The second term represents the convective acceleration. The right hand side describes the external forcing with g the gravitational acceleration, $\frac{1}{\rho}\nabla p$ the pressure term and $\nu\nabla^2 u$ the viscous term, with ν the dynamic viscosity. Note that ∇ represents the divergence operator.

$$\frac{\partial u}{\partial t} + u\nabla u = g - \frac{1}{\rho}\nabla p + \nu\nabla^2 u \tag{2.20}$$

The viscous term, hydrostatic-pressure and surface tension are assumed negligible. Since the impact duration is so short compared to the change in velocity, the gravity and convective terms are considered negligible as well. What remains is the equation of motion given in equation 2.21, in which $\vec{u}$ is the velocity vector.

$$-\frac{1}{\rho}\nabla p = \frac{\partial \vec{u}}{\partial t} \tag{2.21}$$

Substitution of equation 2.21 in 2.19 will result in the change of velocity $\Delta\vec{u}$ during impact.

$$-\frac{1}{\rho}\nabla P = \Delta\vec{u} \tag{2.22}$$

Finally, the divergence is taken to find the pressure-impulse model, which satisfies the Laplace equation.

$$\nabla^2 P = 0 \tag{2.23}$$

This homogeneous equation can be solved by stating boundary conditions at the free edges, which is depicted in figure 2.16a.

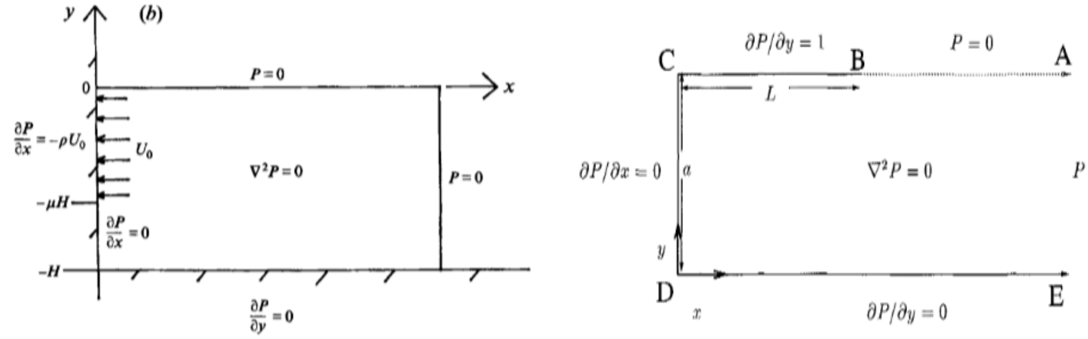

(a) Cooker and Peregrine 1995

(b) Wood and Peregrine (1996)

Figure 2.16: Boundary conditions with and without overhang for pressure-impulse theory

Wood and Peregrine (1996) extended the theory by adjusting the boundary conditions for a structure with overhang as shown in figure 2.16b. Adopting the same constant velocity U_0 in figure 2.16a under the overhanging part, the generalised boundary condition at the overhang becomes $\partial P/\partial y = \rho U$. However, the condition $\partial P/\partial y = 1$ is implemented to obtain a dimensionless case in the form of $\overline{P} = P/(\rho V L)$ in which velocity V and overhang length L are assumed constant and equal to 1.

The vertical impulses on the overhang can readily be calculated by solving the Laplace equation with the newly found boundary conditions. Figure 2.17 depicts the solution in the

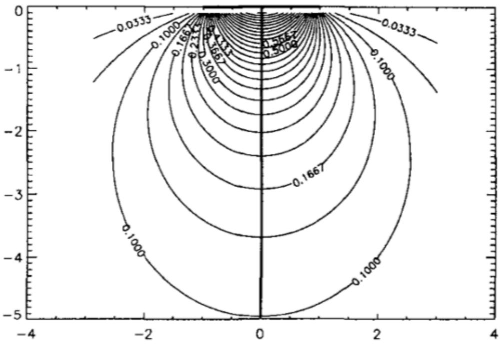

Figure 2.17: Dimensionless impulse distribution on overhang (Wood & Peregrine, 1996)

form of a contour plot when infinite depth is assumed. The axes are made dimensionless by dividing by L. The total dimensionless pressure-impulse is obtained by integration of the circular profile over the overhang, which is equal to $\overline{P} = \pi/4$. The solution dependent on the spatial coordinate z is stated in equation 2.24.

$$\overline{P} = Re\{-iz - \sqrt{1-z^2}\} \tag{2.24}$$

Hofland et al. (2019) reworked the theory by Wood and Peregrine (1996) and obtained a pressure-impulse distribution over the depth, which represents a vertical structure like a gate. This is schematised in figure 2.18.

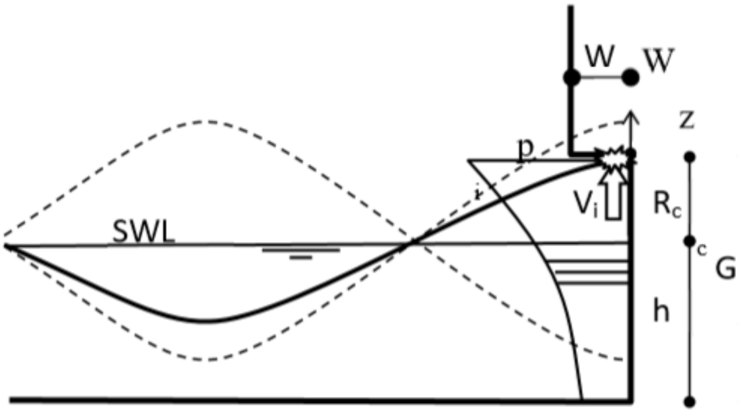

Figure 2.18: Sketch standing wave loading an overhang construction (Hofland et al. 2019)

The parameter R_c describes the freeboard, h de water depth and V_i the upward velocity. Note that the overhang length L is now indicated as W. The dimensionless impulse is derived by integration of the above mentioned Wood and Peregrine solution over the gate height G. The resulting dimensionless pressure-impulse profile is given in figure 2.19.
The total dimensionless force-impulse is calculated by integration of the pressure-impulse over the gate height. (Hofland et al. 2019) fitted a solution through the obtained results for various height over overhang width ratios, as given in equation 2.25. The fitted formula has a given validity of $W/G = 1/5$ to 5 and gives a quick estimation of the expected force-impulse without needing the pressure-impulse distribution.

$$\frac{I}{\rho V W^2} = 0.0053\left(\frac{G}{W}\right)^3 - 0.0713\left(\frac{G}{W}\right)^2 + 0.431\left(\frac{G}{W}\right) + 0.505 \tag{2.25}$$

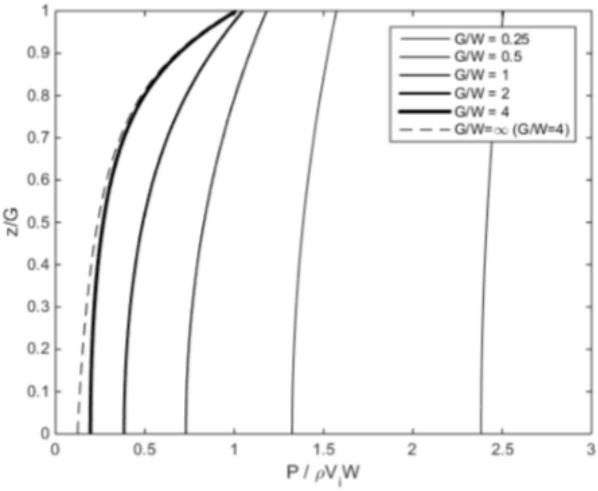

Figure 2.19: Dimensionless Pressure-Impulse profile over gate height for various ratios of height and overhang length (Hofland et al. 2019)

The total vertical force can be approximated by assuming that the impact takes place over the full length of the overhang. This assumption is true for relatively short overhangs defined as $W/L_0 < 0.1$ or $3 < d/W < 6$ in which d is the water depth and L_0 the deep water wave length (de Almeida Sousa et al., 2019). The vertical force on the overhang for a water level at overhang height is found in equation 2.26 by combining the total integrated pressure-impulse on the overhang of $\pi/4$ (Wood & Peregrine, 1996) with the impulse definition from equation 2.18 and multiplication by ρVW to make the outcome dimensional, in which V is the upward reflected particle velocity $u_{z,refl}$. This velocity is assumed constant over a circular profile as schematised in figure 2.20.

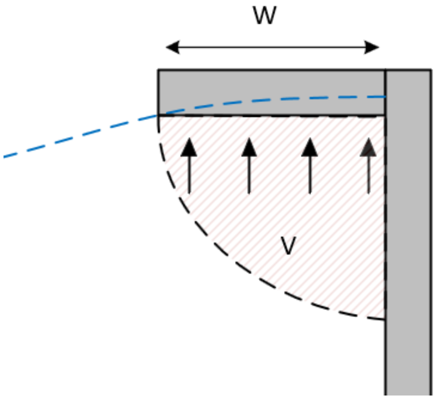

Figure 2.20: Schematised velocity field on overhang for pressure-impulse model

$$F_{overhang} = \frac{\pi \rho W^2 u_{z,refl}}{2dt} \tag{2.26}$$

In which:	W	=	Width overhang	[m]
	$u_{z,refl}$	=	Vertical orbital velocity at the wall	[m/s]
	dt	=	Impact duration	[s]

It should be noted that $u_{z,refl}$ is not equal to equation 2.6. The reflective wave should be added, analogously to the principle as used for equation 2.7 depending on the level of reflection. In case of full reflection, the amplitude a in equation 2.6 simply becomes the total wave height H. The impact duration dt can differ per case and is highly dependent on the level of air entrapment. The value can be found by means of experiment, either physical or numerical, as there is no standardised value available yet.

2.5.3 Conceptual model: Linear wave theory

In this thesis, a conceptual model is introduced, which is derived from linear wave theory (Tuin, 2019). Here, the orbital velocities in horizontal and vertical direction are directly integrated over a control volume to obtain the force-impulse. Figure 2.21 depicts the velocity profiles of which the integrals are derived for a freeboard equal to zero.

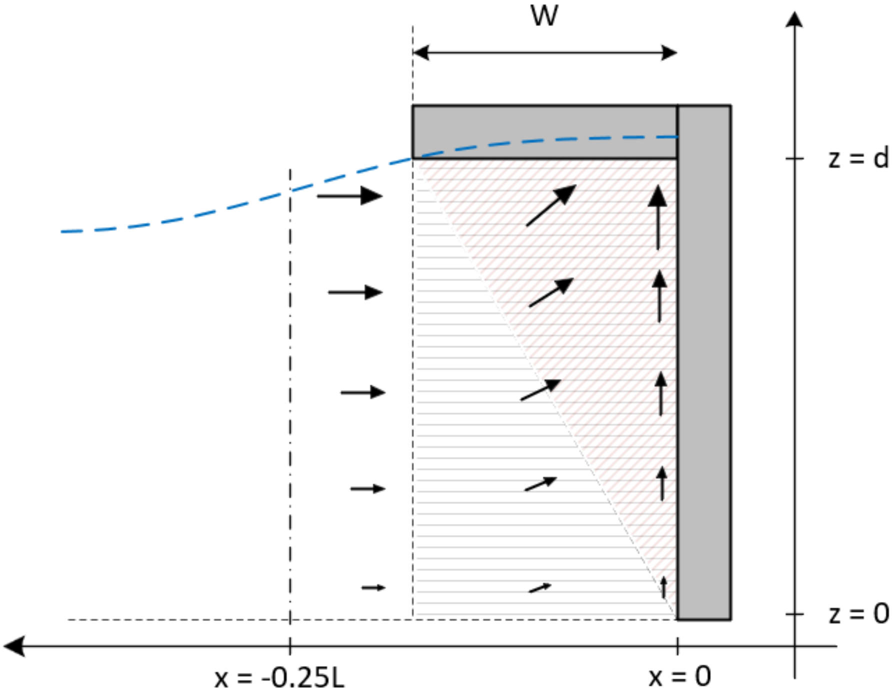

Figure 2.21: Conceptual model

The velocities in x-direction are assumed to have a rectangular profile. The z-direction is assumed to be triangular, in contrast to the circular shape of the pressure-impulse model. The impulses in x and z direction are derived in equations 2.27 and 2.28. The total impulse is found by superposition.

$$I_x = \rho \int_0^z \int_0^{W_{rep}} u_{x,refl}(x,z) dxdz \tag{2.27}$$

$$I_z = \rho \int_0^z \int_0^{W(z)} u_{z,refl}(x,z) dxdz \tag{2.28}$$

In which:				
	W_{rep}	=	Representative width overhang	[m]
	$u_{x,refl}$	=	Horizontal reflected orbital velocity	[m/s]
	$u_{z,refl}$	=	Vertical reflected orbital velocity	[m/s]

The distribution of the reflected particle velocities is obtained similarly to the pressure-impulse model, i.e. in case of full reflection, the amplitude is doubled in equations 2.5 and 2.6. Naturally, the maxima of the horizontal and vertical velocities are out of phase. Therefore, t is set equal to 0, which implies that the vertical velocity reaches its maximum as is the case at the moment of impact, when the water level is equal to the overhang height.

The width $W(z)$, which is dependent on the spatial coordinate z, is equal to 0 for $z = 0$ and W_{rep} for $z = d$ according to the triangular velocity profile. The representative width of the overhang is limited to 1/4 times the wave length, i.e. $W_{rep} = \min(0.25L; W)$. The total force can be found by including the impact duration according to Chen et al. (2019). The assumed areas of integration will be tested in this thesis.

2.5.4 Comparison models

The assumptions of both models and their differences are summarised to provide a clear overview. Pros and cons are mentioned subsequently. Firstly, the pressure-impulse model is considered.

Pressure-impulse model

- Impulse obtained by solving the Laplace equation
- Only vertical impact velocity considered; horizontal impact disregarded
- Circular profile assumed under the overhang with a constant (homogeneous) upward velocity
- Validity range limited to $W/L_0 < 0.1$ or $3 < d/W < 6$
- Relatively difficult to apply due to its mathematical theory
- Theory previously validated by de Almeida Sousa et al. (2019), de Almeida Sousa and Hofland (2020)

Conceptual model

- Impulse obtained by direct integration of the LWT velocities
- Contribution of both the vertical and horizontal impact components
- Rectangular area of integration for the x-velocity and triangular area for the z-velocity over the full height with a width of $\min(0.25L; W)$
- Validity not limited due to the boundary condition of $0.25L$
- Straightforwardly applicable
- Theory not yet validated

Chapter 3

Smoothed Particle Hydrodynamics

In the previous chapter it is described that impulsive wave impact is difficult to predict and highly stochastic. Theoretical models are derived recently and lack extensive validation. Therefore, numerical modelling can be a powerful tool. In this chapter, the methodology and basic formulations of SPH modelling in LS-DYNA® are described. Furthermore, previous research conducted on wave impact with this numerical tool is given.

3.1 Introduction to SPH modelling

SPH is a Lagrangian mesh-free computational method, in which the cells, grids or elements like in traditional Eulerian finite elements (FEM) are replaced by particles. These particles are mathematically linked instead of physically connected. As such, SPH is able to model large hydrodynamic deformations, fragmentation, advection and complex structural interactions in a natural way, while avoiding mesh tangling (Tung, 2018). In more ways, it is advantageous over grid-based models when, for example:

- moving material interfaces with large inhomogeneities are present
- boundaries are deformable
- free surfaces are modelled

However, a significant disadvantage is the fact that a large number of particles are needed for accurate results leading to increased CPU times and expenses. Furthermore, complex boundary conditions or large scale differences are not easily modelled (Filho & Chacaltana, 2017).

The SPH method stores the properties of the fluid, such as mass, density and velocity, locally on the discretised particles, which serve as interpolation points in which the calculation takes place using the weighted properties of the neighbouring particles. This interaction is controlled using a smoothing function, determining the range of the influencing area. The methodology contains a *kernel approximation*, in which the field function is approximated by an integral representation, and a *particle approximation*, in which the integral representation is replaced by the weighted summation of properties of surrounding particles. This is repeated at every time step, called the *adaptation*. Following these steps, the *dynamic analysis* takes place, where an explicit time-integration scheme is applied to the governing equations (Shah, 2010). Figure 3.1 shows an overview of the steps. The kernel and particle approximation are further elaborated in the next section.

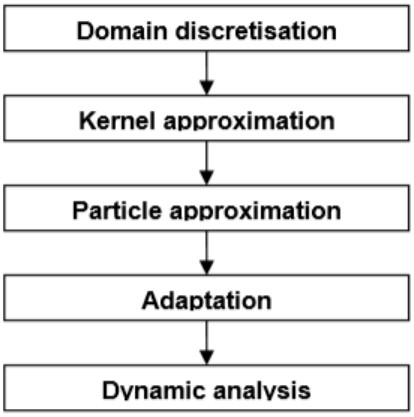

Figure 3.1: Step-wise methodology SPH (Shah, 2010)

To summarise, SPH uses particles to model the fluid domain, which can move freely without the use of a grid. Particles interact with each other depending on the space that they are apart, i.e. the smoothing length. The closer the particle to the point of interest, the more weight the particle gets and the higher the level of interaction.

3.2 Basic formulations

The formulation of SPH method is mainly based on the second and third step in figure 3.1, namely the kernel and particle approximation, which are briefly discussed in this section.

The **kernel approximation** represents a function $f(x)$ and its derivative in an integral form and a smoothing function. The starting point is given in equation (3.1), where Ω is the integration domain and x the position vector (Liu & Liu, 2010).

$$f(x) = \int_\Omega f(x')\delta(x-x')dx' \tag{3.1}$$

in which $\delta(x-x')$ is the Dirac-delta function with properties

$$\delta(x-x') = \begin{cases} 1, & \text{if } x = x'. \\ 0, & \text{otherwise} \end{cases} \tag{3.2}$$

Since the Dirac-delta function only describes one point in the domain and loses too much information to establish a discrete model, it has to be replaced by a smoothing function W, which has a finite spatial dimension h, called the smoothing length. Note that angled brackets are used to indicate the fact that it is an approximation as long as $W(x-x')$ is not equal to $\delta(x-x')$:

$$\langle f(x)\rangle = \int_\Omega f(x')W(x-x',h)dx' \tag{3.3}$$

The smoothing function should satisfy a number of mathematical conditions, namely:

1. Smoothing function is normalised, called the unity condition:

$$\int_\Omega W(x-x',h)dx' = 1 \tag{3.4}$$

2. When the spatial dimension h approaches zero, W approaches the Dirac-delta function, called the delta function property:

$$\lim_{h \to 0} W(x - x', h) = \delta(x - x') \tag{3.5}$$

3. Integration should only take place over the domain of the smoothing function, called the compact condition:

$$W(x - x', h) = 0 \quad \text{if} \quad |x - x'| > \kappa h \tag{3.6}$$

   in which κh defines the spread of W, named the support domain, with κ set as a constant related to the type of smoothing function

Multiple smoothing functions are applicable, for which is referred to e.g. Liu and Liu (2010) and de Koning (2019). An example called the cubic B-spline function is depicted in figure 3.2, which is used in the software LS-DYNA. The width of the support domain is equal to two times the smoothing length.

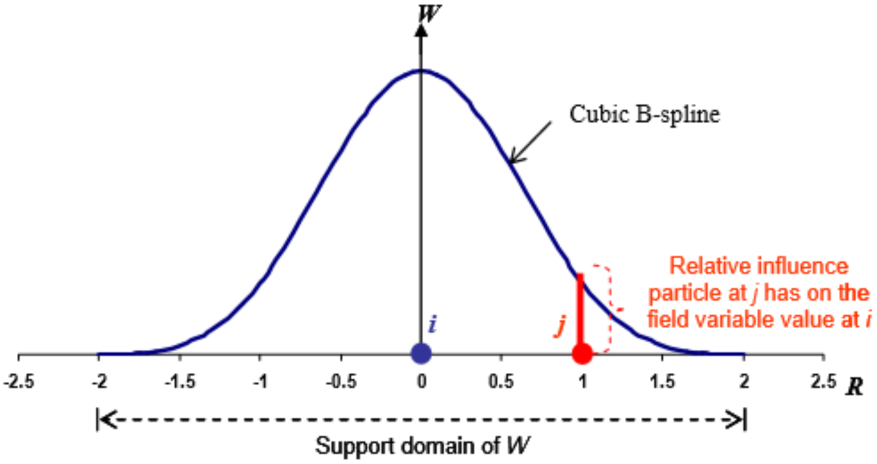

Figure 3.2: Smoothing function (Shah, 2010)

The particle approximation represents the domain Ω with a finite number of particles N and estimates the field variables. The kernel approximation in the form of an integral (equation 3.3) is then rewritten using the weighted summation of the neighbouring particles in its discretised form with m_j and ρ_j being the mass and density of the particle, respectively.

$$\langle f(x) \rangle = \sum_{j=1}^{N} \frac{m_j}{\rho_j} f(x_j) W(x - x_j, h) \tag{3.7}$$

Finally, the fluid pressures are calculated from the particle density using a so called equation of state, given in equation 3.8. Here, a reference density ρ_0 is used and the fluid is considered weakly compressible. c_0 is the speed of sound at the reference density and γ is equal to 7 (Monaghan, 1977).

$$P = B\left[\left(\frac{\rho}{\rho_0}\right)^{\gamma} - 1\right] \quad \text{with} \quad B = \frac{c_0^2 \rho_0}{\gamma} \tag{3.8}$$

Since the mathematical background of the SPH method is not in the scope of this research, only the basic formulations are described above, which is a brief overview of the SPH theory. For a full derivation is referred to Liu and Liu (2010) and Monaghan (1977).

3.3 Literature review SPH modelling of wave impact

To gain insight in what is previously done in the field of SPH modelling of wave-structure interaction, a literature review is conducted. It was found that an often used benchmark test for wave impact loads is a simulation of a dam-break, in which a column of water is released and hits an object. The resulting impact forces are then compared to a physical experiment, whilst varying numerical parameters. An impression of the benchmark test is given in figure 3.3.

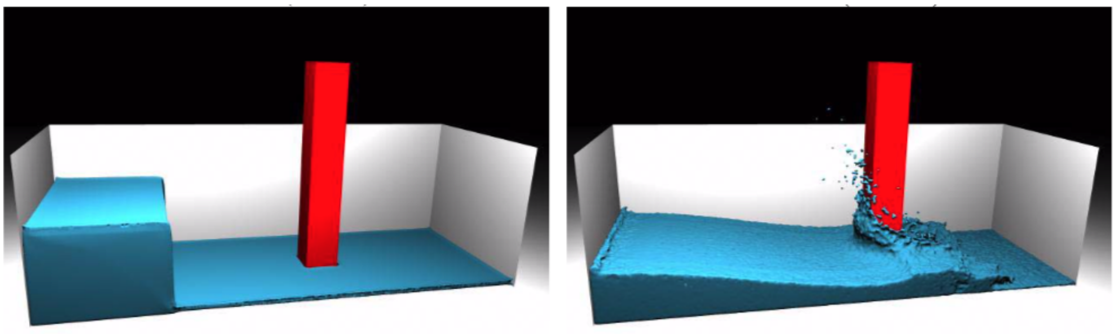

(a) Model at start of simulation (b) Model at moment of impact

Figure 3.3: Dambreak benchmark test on a pillar (Silvester & Cleary, 2006)

Yreux (2018) and Gómez-Gesteira and Dalrymple (2004) performed above mentioned experiment and found that the results of the 3D weakly compressible SPH (WCSPH) model using an equation of state and the physical experiment were in good agreement. The impact forces and the 3D behaviour of the water, such as the movement around and behind the pillar, were according to the observations.

Cummins et al. (2012) and Silvester and Cleary (2006) extended the research by varying the numerical parameters and executing a sensitivity analysis. It was found that the results were practically insensitive to the choice of the kernel function, fluid viscosity and time stepping scheme. The choice of the boundary condition appeared to have the largest influence on the peak loads; a repulsive boundary, pushing the particles from the boundary, led to consistently higher impulse forces.The repuslive boundary condition is further elaborated in section 5.1.1 Overall, the peak forces were overestimated in the results of the above mentioned authors, which is explained by the unrealistic infinite rigidity of the structure in the numerical model. Finally, using a dense particle resolution resulted in the highest accuracy, but naturally increased the computational time.

Niu et al. (2015) and Gui et al. (2014) replaced the pillar by a vertical wall and repeated a dam-break flow simulation with an incompressible SPH (ISPH) model, i.e. replacing the equation of state (equation 3.8) by an incompressible variant. Again, good agreement was found between the numerical and experimental peak values. However, the 2D model was incapable to reproduce an accurate pressure evolution due to the highly 3D behaviour of the water flow. Gui et al. (2014) further analysed the ISPH model by application to broken wave loads on a structure, situated on a sloped beach. Although the calculated pressure curves were realistic, validation lacked with a physical experiment.

Varnousfaaderani and Ketabdari (2015) compared a WCSPH model to experimental data on slightly breaking waves impacting a vertical wall with a sloped berm. Excellent agreement was found in both the pressures and the wave height characteristics. Dao et al.

(2013) attempted to model flip-through impact with a WCSPH model and physical experiments. The wave height time series showed reasonably accurate results. However, the pressures were not validated and no air entrapment was modelled.

Didier et al. (2014) tested SPH for (breaking) wave impact on coastal structures. Physical and numerical models of impact by waves, classified as the 4 different types in Oumeraci et al. (2001), were compared. Good agreement was found in the predicted forces and wave heights. Furthermore, Altomare et al. (2015) compared the design formulae by Sainflou, Goda and Takahashi and to a SPH model with the same conditions in which the formulae were derived. Almost a 1 to 1 correlation was found.

Finally, Rafiee et al. (2013) attempted to include air particles for an accurate representation of the air pocket in breaking wave impacts. The two-phase model returned the physical properties well qualitatively, but no quantification of forces or validation with experiments was performed.

3.4 Gaps in literature

It can be concluded from the literature review that implementation of SPH models to wave impact on coastal structures is not yet extensively studied. Few studies have been executed resulting in promising results for design applications. However, the author is unaware of any studies on standing wave loads on structures with overhang. Furthermore, no literature is found in which numerical models calculate pressure-impulses and force-impulses of impulsive wave impact. No comparison has been made between numerical and theoretical models for pressure-impulse.

Chapter 4

Physical model

Physical experiments have been performed at the Delft University of Technology (TU Delft) in the Hydraulics lab to investigate wave impact of non breaking waves on a vertical wall. Two main geometries have been tested, which are a simple vertical wall and a vertical wall with an overhang. The data acquired in these laboratory tests are used to validate the numerical models in chapter 5. The experiments were executed by de Almeida Sousa et al. (2019) and the results are shared as a courtesy of the TU Delft. This chapter describes the model setup and wave loading conditions.

4.1 Experimental setup

4.1.1 Wave flume

The dimensions of the wave flume are 42 m x 0.8 m x 1 m (L x W x H) with a smooth flat bottom. The waves are generated using a piston type wavemaker, which is equipped with an active wave absorption system (AWAS) to prevent re-reflected waves from disturbing the wave field. This way, wave trains with constant amplitudes are generated for the duration of the experiment. The wave paddle is placed at 30.8 m from the wall. The water surface elevation is measured with wave gauges placed at multiple locations in the flume and one wave gauge right under the overhang. For the two main geometries, these locations are sketched in figure 4.1 with the distances tabulated in table 4.1.

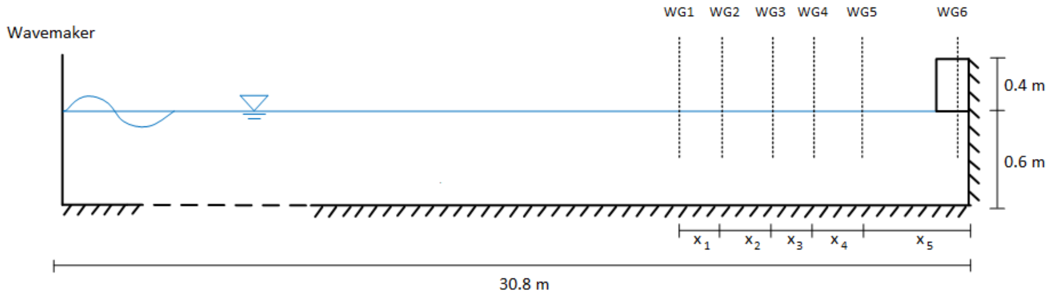

Figure 4.1: Physical model setup

Configuration	x_1[cm]	x_2[cm]	x_3[cm]	x_4[cm]	x_5[cm]
No overhang	29	40.5	29	39	151.5
Overhang	29	41	29	39.5	151.25

Table 4.1: Location wave gauges

4.1.2 Dimensions of test cases

Three different structures are placed in the wave flume, which are

1. Vertical wall without overhang
2. Vertical wall with short overhang
3. Vertical wall with longer overhang

The geometries were constructed by mounting an aluminium structure on a 0.8 m x 0.8 m x 1 m concrete block, providing the stability. The thickness of the structure imitates a rigid boundary for the incident waves. The parameters defining the configurations with an overhang are given in figure 4.2. In the tested conditions the freeboard equals zero as indicated in paragraph 4.1.3, since this situation yields the highest upward velocities.

In all cases, the structures are equipped with pressure sensors (PS) with a sampling frequency of 20 kHz (Kulite HKM-375M-SG with 1 bar range) along the wall. In total, 8 pressure sensors are used to measure the impacts in test case 1. The same setup is used for case 2 and 3 with the removal of PS8 and addition of PS7 placed at 7 and 17 cm from the wall for the short and longer overhang respectively. The dimensions of the structures and placement of the measurement devices are illustrated in figure 4.2

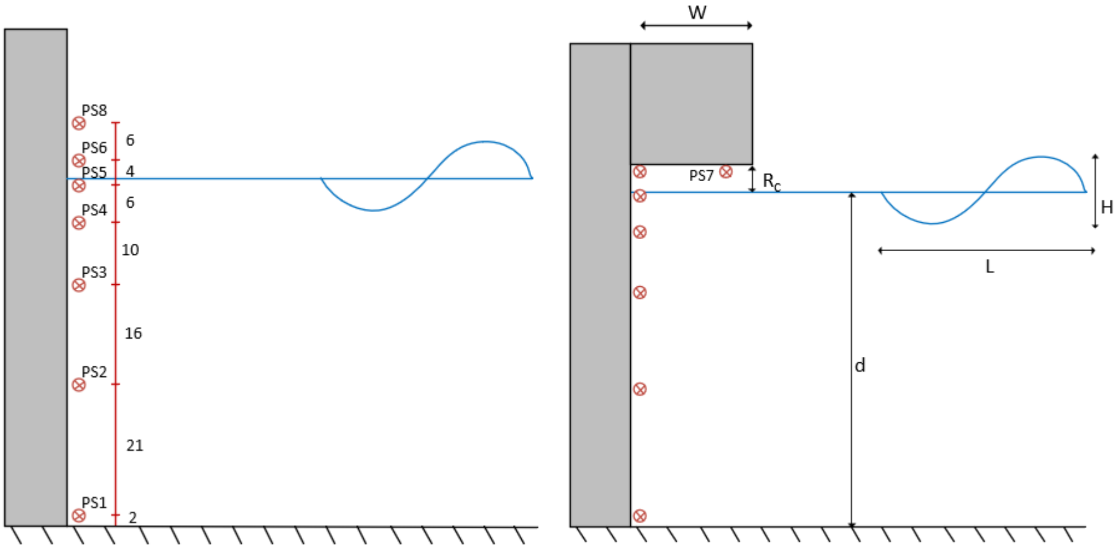

(a) Structure without overhang (b) Structure with overhang

Figure 4.2: Dimensions configurations and locations measurement equipment in [cm]

4.1.3 Applied wave conditions

In total, 6 test conditions are applied in this thesis with varying geometrical parameters, wave heights and wave periods. It should be noted that only regular non-breaking wave conditions are considered. The different cases are labeled and will be referenced as such consequently. The applied wave conditions are summarised in table 4.2. The wave steepness is kept equal to $H/L = 0.024$ for all scenarios. The long overhang configuration is referenced as 'longer', as it still suffices the condition of subsection 2.5.2 for short overhangs.

Configuration	Label	d [m]	H [m]	T [s]	L [m]	W [m]	R_c [m]
Vertical wall	A	0.6	0.06	1.3	2.416	0	-
	E	0.6	0.1	1.9	4.094	0	-
Short overhang	AS	0.6	0.06	1.3	2.416	0.1	0
	ES	0.6	0.1	1.9	4.094	0.1	0
Longer overhang	AL	0.6	0.06	1.3	2.416	0.2	0
	EL	0.6	0.1	1.9	4.094	0.2	0

Table 4.2: Experimental wave conditions

4.1.4 Observed wave impact types

Figure 4.3 shows the observed wave impacts for the conditions as stated in table 4.2, captured by camera recordings.The observations are summarised subsequently.

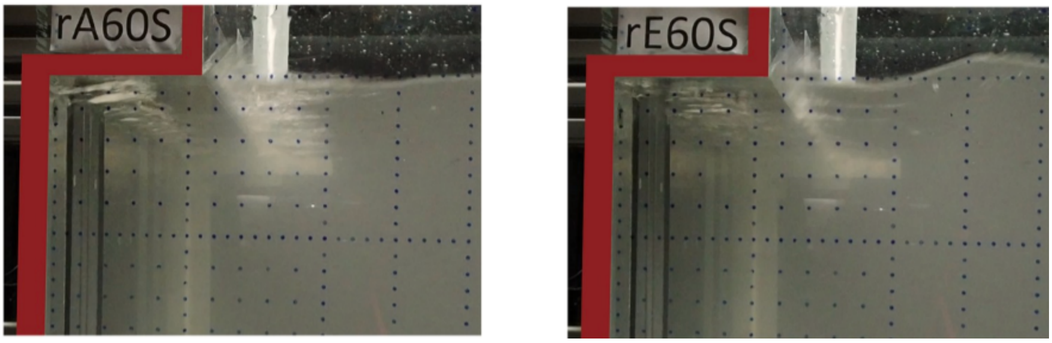

(a) Case AS (b) Case ES

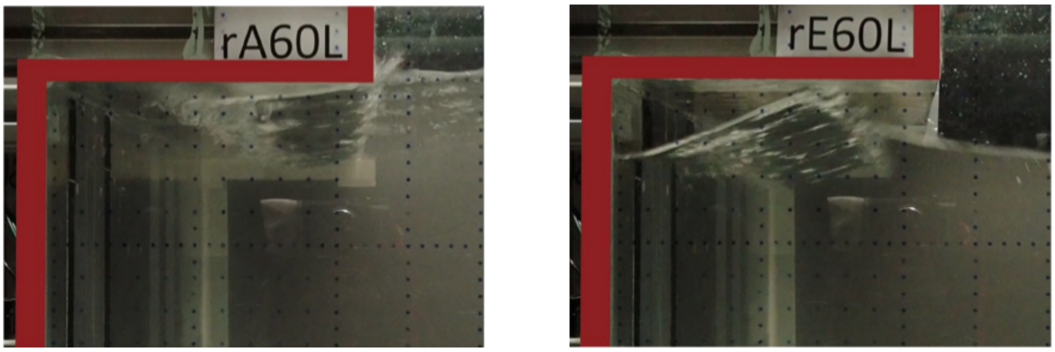

(c) Case AL (d) Case EL

Figure 4.3: Observed wave impact in experiment (de Almeida Sousa & Hofland, 2020)

- **AS**: Wave distributed over the outer first half of the overhang at the moment of impact with an intermediate sized air pocket near the wall
- **ES**: Very little air is entrapped at the moment of impact, so a practically flat wave hits the structure over the entire width. This is a so called flip-through impact
- **AL**: Large air pocket spread out over the entire width of the overhang. Wave impacts at the far outer end of the overhang
- **EL**: A steep wave hits the structure roughly in the middle of the overhang. A second impact is observed at the left inner part

The physical behaviour is largely varying for the different conditions as observed from the images and will be used to explain possible deviations in the numerical model from the experiment further on in this thesis.

4.1.5 Post-processing of results

The experimental pressure data is subjected to low-pass filtering before analysis of the pressure peaks, using a Butterworth 3rd order filter with a cut-off frequency of 150 hz (de Almeida Sousa et al., 2019). As a result, the noise that disturbs the signal, caused by vibrations and other dynamic interactions between the fluid and the structure, is removed. The frequency is chosen in such a way that the wave signal and impulse remain undisturbed. An example of a filtered and unfiltered signal is displayed in figure 4.4. The data in the numerical model is filtered equally to be consistent with the experiment.

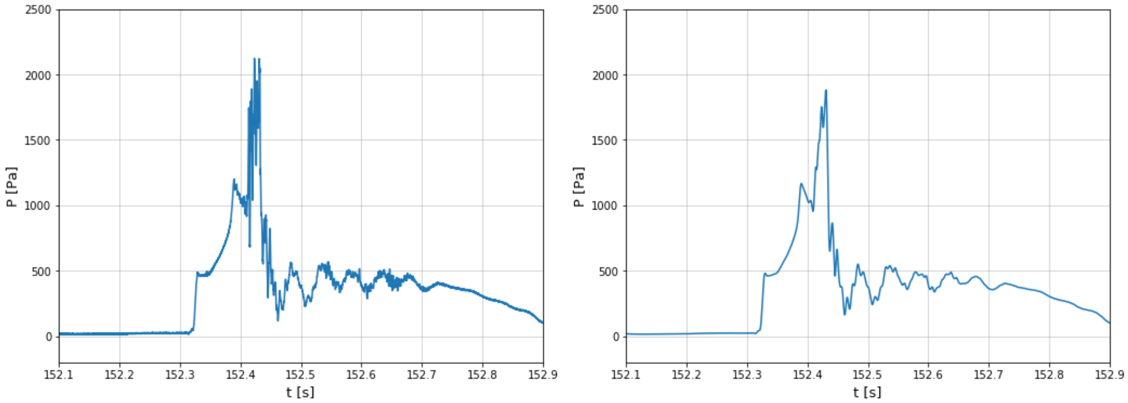

(a) Unfiltered signal (b) Filtered signal

Figure 4.4: Filtered vs unfiltered pressure distribution

Finally, scaling issues are irrelevant in this study as the numerical models have equal dimensions and wave conditions to the experimental setup. Naturally, the experiment itself is subject to scaling effects like the size of the air pockets and geometrical parameters. Therefore, driving factors such as inertia and gravity are carefully chosen to represent the wave motion on full scale.

Chapter 5

Numerical modelling

This chapter deals with the setup of the numerical models to simulate the physical experiment described in chapter 4. In this thesis, two software packages are tested, which use different approaches in the application of SPH. These approaches come with various limitations, of which an overview is given.

5.1 Review applied numerical tools

As stated, two different SPH software packages are used, which are the open source code DualSPHysics and the SPH module of the FEM package LS-Dyna. Both make use of the WCSPH formulation. For a full theoretical description of the different software is referred to Crespo et al. (2015) and Hallquist (2006). The main focus lies on the differences between the two approaches and their current limitations, when applied to a wave impact problem with overhang.

5.1.1 Boundary conditions

In DualSPHysics, the numerical model exists purely of SPH particles, which means that the rigid boundary formulations are described by the use of particles as well. This method, called the dynamic boundary condition, treats the boundary particles as fluid particles, so that the same equations are satisfied. However, the movements induced by the exerted forces remain fixed. Contact between the fluid and boundary is defined by a density increase of the boundary particles, when the fluid particles are within a distance of twice the smoothing length h_s, as given in equation 5.1. This leads to a pressure increase inducing a repulsive force, pushing the fluid particles away from the boundary.

$$h_s = C_h \sqrt{dim \cdot dp^2} \tag{5.1}$$

In which:			
	C_h =	Coefficient (usually between 1 and 1.5)	[-]
	dim=	Dimensions of model (2 or 3)	[-]
	dp =	Particle size	[m]

A drawback of this method is that a gap is created at the boundaries, of which the width is measured to be approximately $1.5h_s$. Figure 5.1 shows the fully developed gaps observed at the moment of wave-boundary interaction. The effect the gap has on the results is described in subsection 5.1.3.

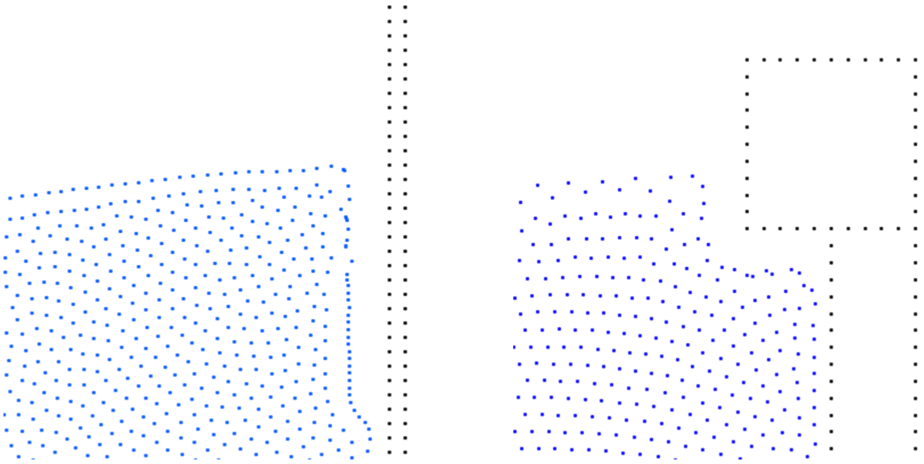

(a) Observed gap vertical wall (b) Observed gap short overhang

Figure 5.1: Gap dynamic boundary condition

In LS-Dyna, the fluids are described by particles and the boundaries by either FEM elements or symmetry planes. The former allows rigid or elastic bodies to be created with shell (2D) or solid elements (3D) with the desired material definitions. The latter creates ghost particles with the same properties as the opposite particles in the domain cancelling their movement. This is useful for parts in the model where no data has to be acquired, e.g. the bottom of the flume, to save computational time, since no contact has to be defined. The contact algorithm between the SPH particles and the FEM elements is based on penetrations of the master segments by the slave particles. The search for these penetrations is performed in every calculation cycle and when found, a proportional counteracting force equal to the penetration depth is applied to the slave particle to eliminate the penetration.

5.1.2 Wave generation

To induce a similar wave field as the observed one in the physical experiments, a piston-type wave maker is applied in the numerical wave tanks. The horizontal motion of the piston is determined by using wave maker theory, which relates the excitation of the piston to the properties of the incident wave as developed by Galvin (1964) in shallow to intermediate water. This so called transfer function is given in equation 5.2. The total displacement of the piston to produce first order waves is given by equation 5.3. The second order harmonics can be left out, since they do not change the piston movement for the applied wave conditions and their relatively short periods.

$$\frac{H}{S} = \frac{2\left(\cosh\left(2kd\right) - 1\right)}{\sinh\left(2kd\right) + 2kd} \tag{5.2}$$

$$x_p(t) = \frac{S}{2}\sin(\omega t) \tag{5.3}$$

In which: S = Piston stroke [m]
x_p = Horizontal motion piston [m]

This translation $x_p(t)$ is applied to a rigid body in both DualSPHysics and LS-Dyna. As aforementioned, the physical wave flume used a wavemaker with an AWAS system. Naturally, this would be feasible to use in the numerical models as well, not only to reproduce the reality, but moreover providing the possibility to limit the length of the model and consequently the number of particles in the flume, lowering the computational time. However, only DualSPHysics allows an AWAS to be implemented , which measures the surface elevation at a distance of 4-10h from the wavemaker and corrects the excitation of the piston to the target surface elevation (Altomare et al., 2017). This ensures a stable wave field with constant amplitudes during the run time of the model. Therefore, a turbulent disturbed wave field is expected to be observed in LS-Dyna after a certain time, depending on the celerity of the waves and the length of the model. This should be taken into account when determining the parameters of the numerical model setup.

5.1.3 Limitations

The above mentioned differences lead to some limitations of the numerical models in both software. Firstly, the pressures and forces at the wall of the structure have to be measured at a distance of $1.5h_s$ from the boundary, when the dynamic boundary condition of DualSPHysics is applied. This is not an immediate issue, as the experimental results can be well reproduced for a simple vertical wall, as will be shown in chapter 6. However, for a simple vertical wall the gap only occurs horizontally. When an overhang is constructed, the gap will be observed both horizontally and vertically (figure 5.1b, which disturbs the results. Furthermore, the repulsive forces induced by the density increase are amplified, resulting in the particles to 'bounce' too much when interacting with the rigid boundary. This causes a second and third peak in the hydrostatic part of the force distribution. Therefore, DualSPHysics in its current version (v4.4) is unable to reproduce the physical behaviour of impulsive standing wave impact at an overhang construction, as depicted in figure 5.2 compared to LS-Dyna..

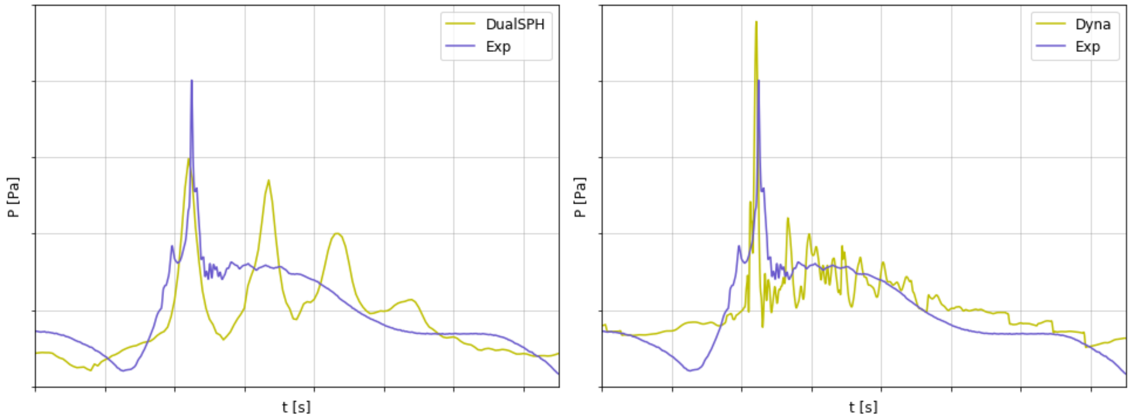

(a) DualSPHysics (b) LS-Dyna

Figure 5.2: Pressure distribution per software for arbitrary impact

Secondly, the observed wave fields are varying depending on the used software. As previously stated, only DualSPHyics has the option to apply an AWAS. This has a drastic influence on the stability of the wave field and resulting pressure peaks. Figure 5.3 shows the measured water surface elevation at WG3 for case A in both software with the same conditions: a numerical domain length of 7.7 m and a particle size dp = 0.01 m.

It is evident that DualSPHysics is well able to produce a stable wave field while actively eliminating re-reflections and preventing them from disturbing the domain, which allows for longer run times of the simulations. Therefore, a clear steady state is reached at t = 10 s and waves with constant amplitudes are recorded close to the impact zone. On the contrary, the wave field observed in LS-Dyna will not reach the desired steady state.

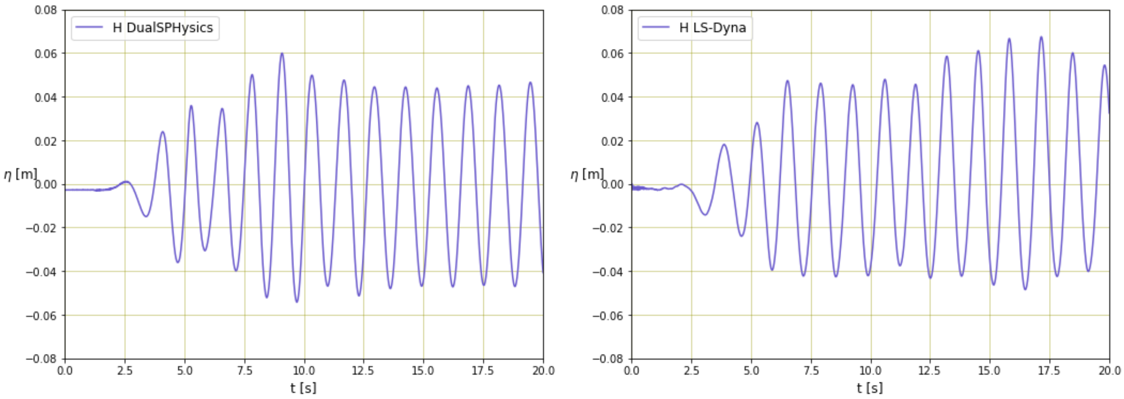

(a) DualSPHysics water surface elevation

(b) LS-Dyna water surface elevation

Figure 5.3: Measured water surface elevation with and without AWAS for case A

At t = 13 s, re-reflected waves are measured at the wave gauge. Naturally, this directly impacts the force distributions. It is attempted to create an AWAS manually in LS Dyna by extracting the movement of the piston in DualSPHysics, though without a good result. The difference in the formulation of SPH in both software (i.e. artificial viscosity, time stepping, numerical diffusion) does not allow one to one implementation. Therefore, a trade-off should be made in the domain length of the model, the computational time and the number of wave impacts, as further explained in section 5.2.

Thirdly and finally, numerical diffusion in the SPH formulation is observed when wave heights are recorded at several locations in the domain, which influences the validity of the wave maker theory. The amount of dissipation is dependent on the particle resolution. Altomare et al. (2017) recommends a ratio of $dp = H/10$, which is not always manageable for small wave heights, since it may drastically increase the computational time. Nonetheless, the excitation of the wave maker has to be manually corrected to produce the target wave heights.

It can be concluded that both software come with their limitations. The boundary conditions in DualSPHysics prevents its use for the overhang configurations and LS-Dyna is unable to produce stable wave fields for longer simulations. However, LS-Dyna currently has the superior boundary condition formulation. Therefore, it is chosen to apply DualSPHysics to cases A and E, i.e. the simple vertical walls, and LS-Dyna for cases AL, AS, EL and ES.

5.2 Setup numerical models

The setup for the 6 numerical models is chosen to be a trade-off between the stability of the wavefield, the number of recorded impacts according to the target wave height and the computational time. These considerations follow directly out of the limitations as described in subsection 5.1.3. The particle size is equal to dp = 0.01 m initially. A sensitivity analysis is performed in section 5.3 to further explain the chosen particle size. All models are 2D and constructed in the XY-plane. The coefficient C_h is set equal to 1.2, providing the average between the smoothing length and the computational time.

The models for Case A and E are only minimally subject to disturbances in the wavefield, due to the implementation of an AWAS. Therefore, the domain length can be shortened to decrease the computational time. To ensure that the waves can fully develop before reaching the rigid boundary, the length of the model will adjusted to satisfy the condition $L_x/L \approx 2$, i.e. proportionally to the wave length. Figure 5.4 displays the dimensions of the numerical domain with the parameters tabulated in table 5.1.

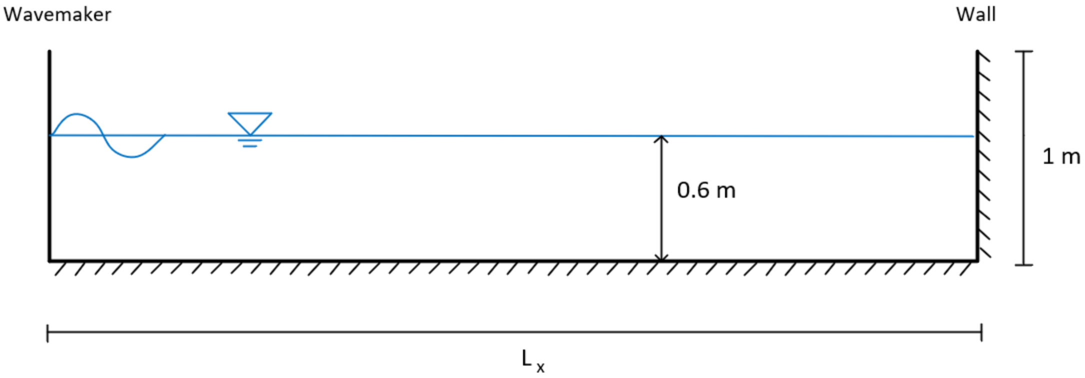

Figure 5.4: Numerical domain vertical wall

Case	L$_x$[m]	#Particles
A	5	30445
E	7.7	46643
AL/AS	15.4	95604
EL/ES	15.4	95604

Table 5.1: Dimensions numerical domain

The cases with an overhang (AL, AS, EL and ES) are modelled without an AWAS. Therefore, the main consideration for the domain length is the number of wave impacts that can be recorded in a stable wave field with a feasible computational time. A prediction can be made when the disturbances will take place using the wave celerity and an arbitrary domain length. The wave celerity can be calculated from the parameters in table 4.2. For cases AL and AS, this is equal to c = 1.86 m/s. For EL and ES, the wave celerity is equal to c = 2.15 m/s. Taking this into account, a numerical domain length equal to half the physical experiment is chosen, equal to $L_x = 15.4$ m. Re-reflected waves will arrive at the structure approximately after t = 25 s for cases AL, AS and t = 22 s for cases EL, ES. Naturally, the wave gauges will record the disturbances earlier in the simulation due to their placements away from the wall and the time it takes to produce the first wave with the goal wave height. As a result, around 5-6 wave impacts will be comparable to the experimental results.

Figure 5.5 shows the final dimensions of the numerical models with an overhang, with the parameters added to table 5.1. The overhang is roughly meshed with shell elements and the bottom and vertical wall are modelled with symmetry planes. The choice for these boundary conditions is elaborated in appendix B, where a variant study is carried out for different model setups.

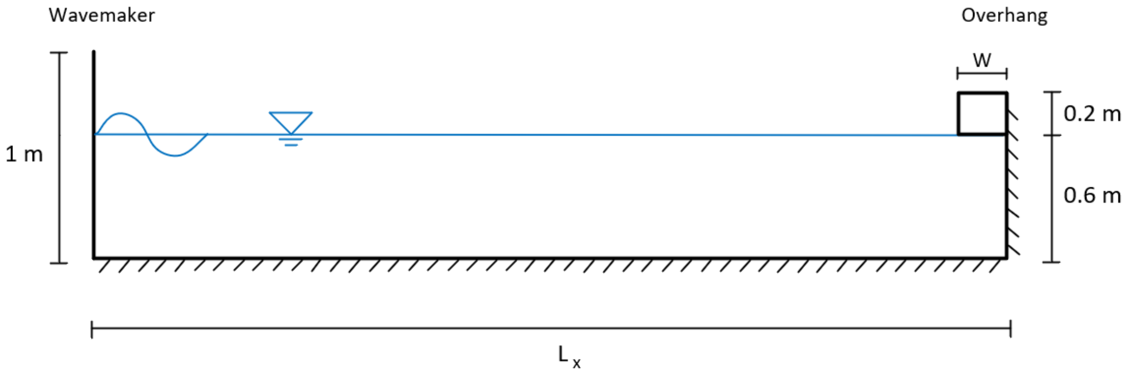

Figure 5.5: Numerical domain structure with overhang

An impression of the final model during wave impact is given in figure 5.6 in its final form, i.e. symmetry planes as boundary conditions, a particle size of 0.01 m and an overhang roughly meshed with shell elements.

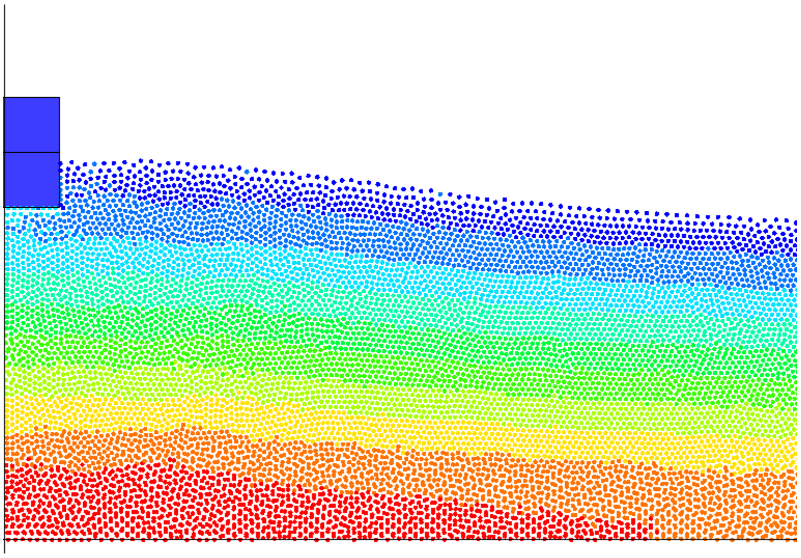

Figure 5.6: Impression of SPH model with short overhang

5.3 Sensitivity analysis

A sensitivity analysis of the particle size, smoothing length and sampling frequency is performed to determine the best variations to be applied in this study. Starting with the particle size, the logical options based on model size and wave height are $dp = 0.02$ m, 0.01 m and 0.005 m. The overhang configurations AL and EL will be used as a reference case. The analysis consists of an accuracy check of the wave generation at WG3 and the force estimation on the overhang compared to the computational times. The total number of particles are 24704, 95604 and 376004, resulting in computational times of 5, 58 and 606 minutes respectively for a run time of $t = 25$ s. Furthermore, the sampling frequency is chosen by analysing a solitary wave impact for various frequencies for the model dp.

5.3.1 Wave generation

According to subsection 5.1.3, it is expected that a smaller particle size results in less diffusion of the wave height and so a smaller numerical error. Figure 5.7 shows the measured water surface elevation for the different particle sizes for case AL and EL.

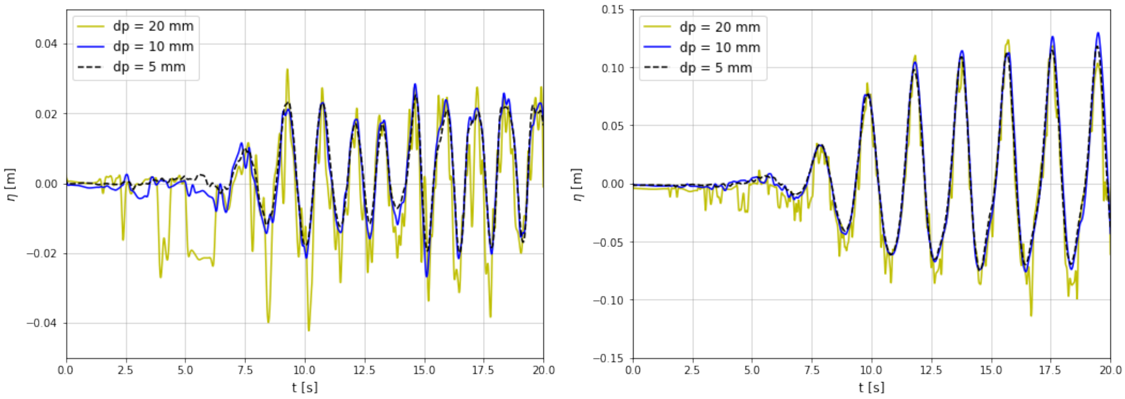

(a) WG3: Case AL

(b) WG3: Case EL

Figure 5.7: Results for different particle sizes at WG3

It is evident that a *dp* of 0.02 m is too coarse for the models due to the noisy surface elevation it generates, especially for case AL and its small wave height (0.06 m). Clearly, this particle size can be disregarded. A stable solution is found for the particle sizes $dp =$ 0.10 mm and $dp = 5$ mm. The differences between the particle sizes are strengthened for a smaller wave height. However, in terms of wave generation it is not needed to maintain the smaller particle size, as the differences in evolution and magnitude of the wave height are negligible. A computational (CPU) time increase of magnitude 10, does not justify the smaller diffusion error and slightly less noisy wave field.

5.3.2 Force estimation

Figure 5.8 depicts the difference in the reaction force output of the model for the two remaining particle sizes on the overhang.

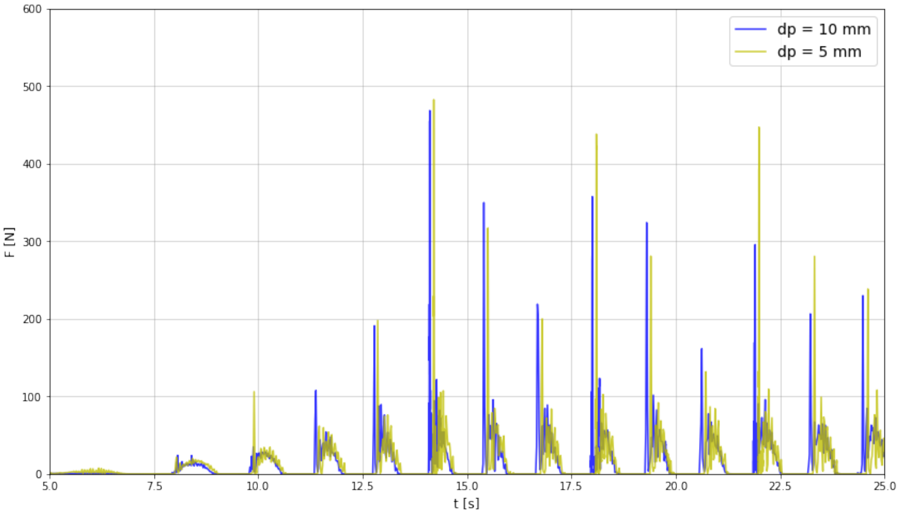

Figure 5.8: Force comparison for particle sizes on overhang (LS-Dyna)

From the figure it follows that the consistency of force peaks is more or less equal. This is quantified by calculating the mean and standard deviation of the peak forces for the fully developed stable wave field between t = 13-21 s before re-reflected waves are observed, as tabulated in table 5.2.

dp [mm]	μ [N]	σ [N]
10	313.46	99.59
5	308.43	123.15

Table 5.2: Comparison peak forces per particle size

Evidently, a small deviation is found of 1.6% for the peak forces. However, the fluctuation in forces is increased for dp = 5 mm with 20%. That said, a particle resolution of 10 mm does give a good estimate and is found suitable for further analysis, taking into account the extremely lowered computational times. The error margin between the particle sizes is deemed not critical.

5.3.3 Dependency on sampling frequency

In the experiment, a sampling frequency of 20 kHz is applied to determine the pressures and a sampling frequency of 100 Hz for the wave gauges. In the numerical model, a sampling frequency of 20 kHz would lead to result files of multiple terabytes, which is far too large for post-processing. Therefore, multiple runs are performed with various time steps to determine what frequency is necessary to obtain an optimum between simulation time, file size and reliability of data. To measure the water surface elevation, an equal frequency of 100 Hz is chosen as applied in the experiment. Figure 5.9 shows a solitary wave impact on the overhang with a sampling frequency of 50 Hz, 100 Hz, 1 kHz and 2 kHz.

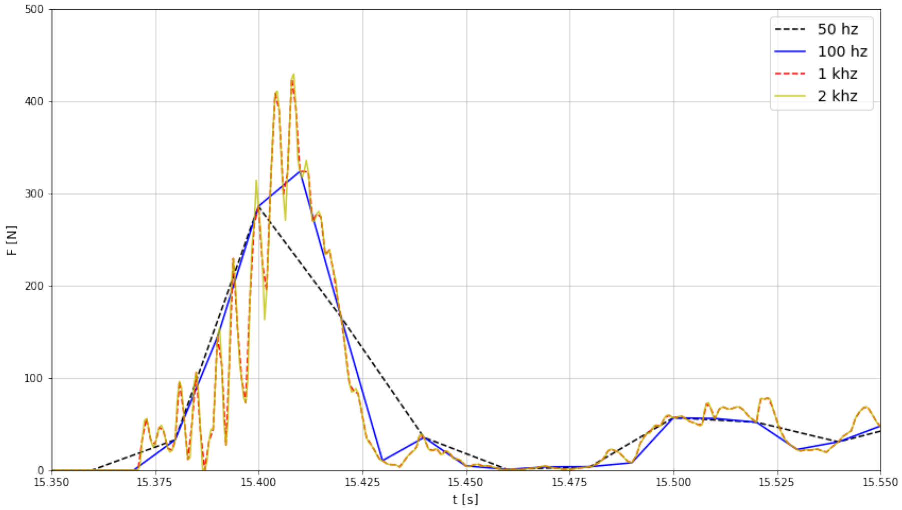

Figure 5.9: Solitary wave impact on overhang for various sampling frequencies (LS-Dyna)

It can be observed that the peak of the force is not recorded for frequencies below 1 kHz. For 2 kHz, no higher force peak is observed than for 1 kHz. In fact, exactly the same force distribution is obtained. Therefore, it is chosen to use a sampling frequency of 1 kHz for all numerical models with an overhang.

5.3.4 Dependency on smoothing length

As stated in chapter 3, the smoothing length determines the domain of interaction of the particles. Equation 5.1 presented the constant C_h, which can be changed between the values 1 and 1.5 (boundaries given by the software) to determine the length of this domain, as the particle size and dimension of the model are a given. The smoothing length has to be a compromise between the stability of the model and the CPU time. The higher the value of C_h, the more interaction occurs resulting in an increase in CPU time. However, using a smoothing length that is too large can result in instability at the boundaries. In this section, the effects of the constant are treated and a final value is chosen to implement in the models.

Ideally, a large smoothing length is desired to have the least amount of numerical diffusion possible. As such, the wave generation will be closest to the target wave height when equation 5.2 is applied. However, when values are chosen larger than 1.2, instabilities occur near the boundary surface. As the particles under the overhang are in a confined space, and the boundary surface is exerting too much weight in the interaction, the particles 'shoot' away as illustrated in figure 5.10a for the first timestep in the simulation. Therefore, it is infeasible to use values larger than 1.2.

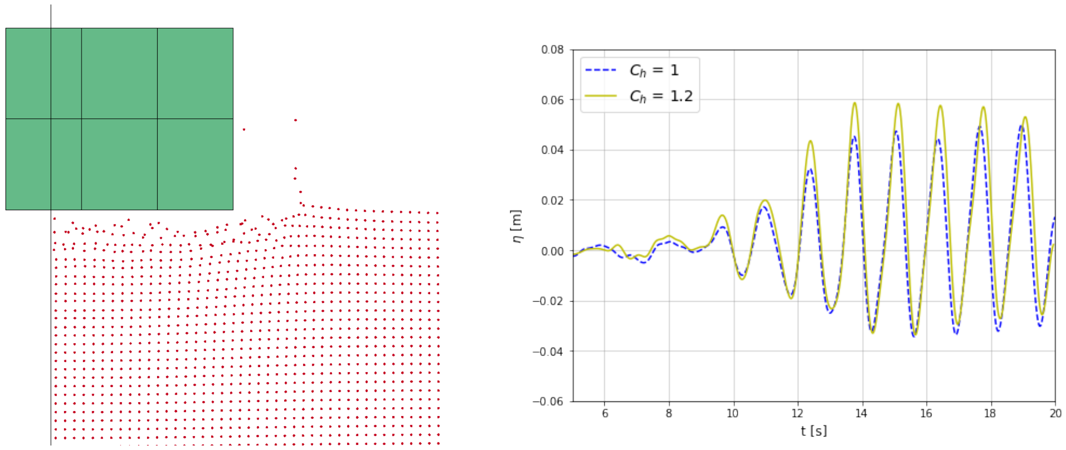

(a) Instabilities near the boundary surface (b) Wave height at 1 m from overhang

Figure 5.10: Sensitivity of smoothing length; factor C_h

Values smaller than 1.2 would speed up the CPU time slightly, in the order of ∼ 10%. Though, more numerical diffusion will be present, which will not only affect the wave generation, but also the transmitted pressure in the particle domain. Figure 5.10b shows the measured surface elevation at 1 m from the longer overhang for $H = 0.06$ m and $T = 1.3$ s with C_h equal to 1 and 1.2. It is concluded that the numerical diffusion is too large to simulate the experiment realistically for a $C_h = 1$. Therefore, the value is set equal to $C_h = 1.2$.

5.4 Post-processing of results

The results from the models are obtained using a Python tool developed for this thesis, to extract the data stored on the particles. This was done to omit the deficiencies in post-processing tools as provided by LS-Dyna. Namely, no numerical wave gauges; only separate particles could be selected causing inaccuracy due to their horizontal translation, and no accurate pressure measurements, as further explained in appendix B. The methodology of the tool is explained in this section.

The output of the software consisted of a file with the location of each particle for every time step including the stored data per particle. By filtering out the nodal coordinates for the locations of interest, e.g. the location of a pressure sensor, data could be extracted at point precise locations. In doing so, a buffer of half a particle size was applied in all directions to ensure measurements for every time step. Then, data could be extracted such as the water surface elevation (η), pressures (P) and velocities (u). Finally, the data is filtered according to a 3rd order Butterworth filter with a cut-off frequency equal to that of the experiment. The process is depicted in figure 5.11 in the form of a flow chart.

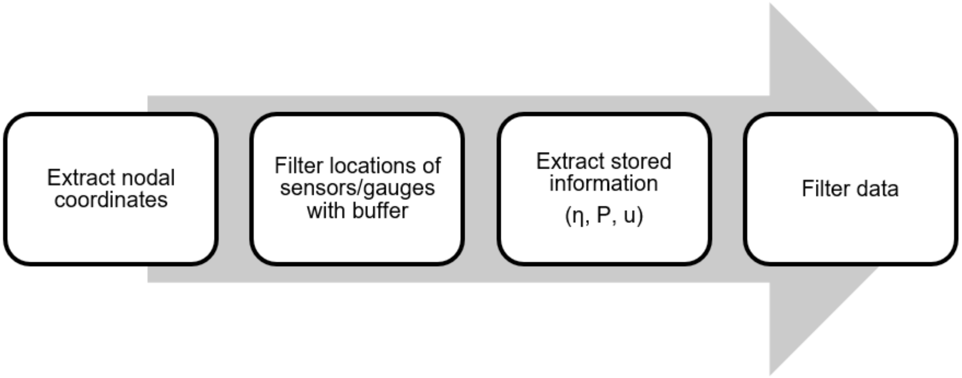

Figure 5.11: Flow chart Python tool

Chapter 6

Comparison numerical and experimental results

This chapter treats the results returned by the numerical models. All cases are considered with the setup and dimensions of the models according to section 5.2. The location of the wave gauges and pressure sensors can be found in section 4.1. Firstly, the wave heights and pressure distributions are compared to the experimental results. Thereafter, the impulses are compared and the methodology of the impulse calculation is elaborated. All results are obtained by using the Python tool as explained in the previous chapter. As stated in subsection 5.1.3, the cases without overhang are modelled in DualSPHysics and the cases with overhang in LS Dyna. This is indicated in the legends for clarity.

6.1 Wave generation

The water surface elevation measured at wave gauges 1 through 6 are treated in this section for both the experiment and numerical models in a qualitative and quantitative manner, starting with the cases without overhang, followed by the short and longer overhang configuration. The locations of the wave gauges for a structure without overhang are shown again in figure 6.1.

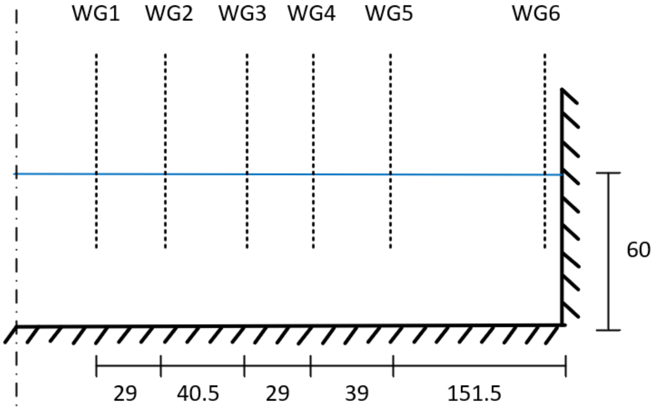

Figure 6.1: Location wave gauges without overhang in [cm]

6.1.1 No overhang

The results of wave gauges (WG) 1, 3, 4 and 6 are given in figure 6.2, starting with the recorded wave heights for case A, i.e. $H = 0.06$ m, $T = 1.3$ s. The results of the remaining wave gauges are depicted in appendix C.1.

The SPH results show excellent agreement with the experiment. The wave field is observed to be stable, even after reflection occurs due to the AWAS, and the magnitude of the peaks and the troughs of the waves are well reproduced. Only WG1 and WG3 show some deviation to the experimental wave height, which are also the smallest recorded surface elevations in the domain. Therefore, the amplified elevation in WG1 and dissipation in the wave peak of WG4 are assumed to be caused by the relatively coarse particle size to wave height ratio, i.e. $H/dp < 10$.

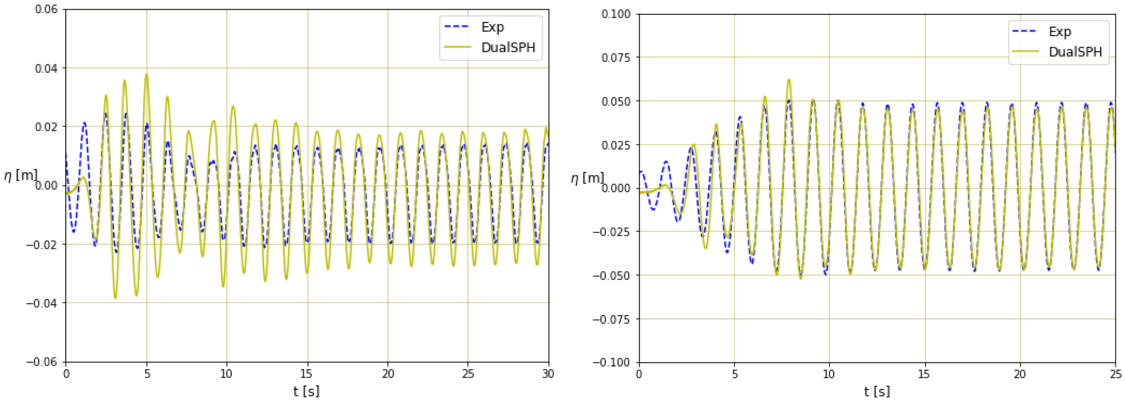

(a) Case A: WG1

(b) Case A: WG3

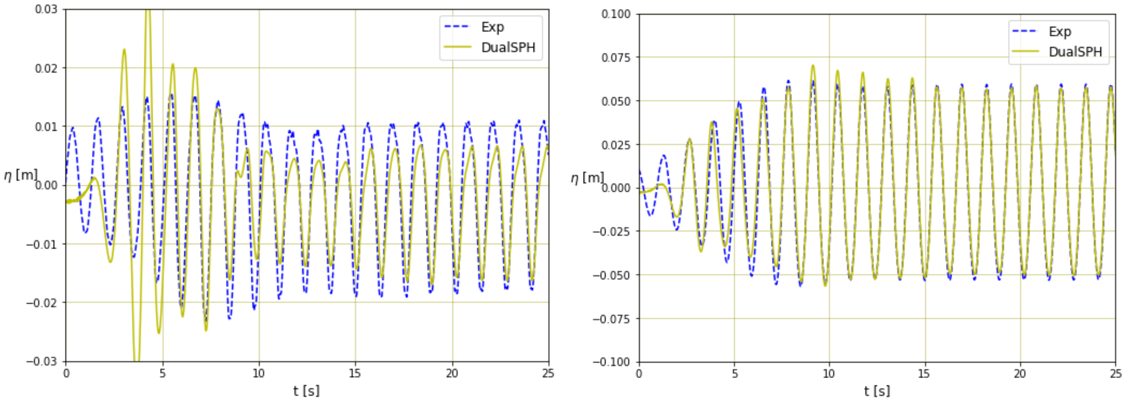

(c) Case A: WG4

(d) Case A: WG6

Figure 6.2: Wave height comparison case A: $H = 0.06$, $T = 1.3$ s

The level of accuracy of the model is quantified by calculating the relative errors in wave heights and by means of the statistical parameter R^2; the coefficient of determination. This parameter describes the fit of the numerical wave field to the experimental one from 0 to 1, in which 1 means a perfect fit. The values in table 6.1 are obtained for the surface elevation after $t = 11$ s, as this is the point in time where the steady state is reached for both SPH and the experiment. For this region, the mean values of the troughs and peaks are selected and added to obtain the total wave height. The relative error is calculated by (SPH-Exp)/Exp * 100%.

WG	R^2 [-]	H_{Exp} $[m]$	H_{sph} $[m]$	Error [%]
1	0.81	0.033	0.046	37.9
2	0.98	0.097	0.108	11.2
3	0.99	0.096	0.093	-3.6
4	0.83	0.029	0.023	-22.3
5	0.99	0.077	0.084	0.09
6	0.99	0.112	0.108	-0.04

Table 6.1: Quantification wave field case A: $H = 0.06$ m, $T = 1.3$ s

The relative errors in total wave height confirm the observed behaviour in the graphs and show the largest deviation in WG1 and WG4 due to the ratio $H/dp = 10$ not being sufficed. In general however, there is excellent agreement and the remaining wave gauges show a near perfect overlap.

This process is repeated for case E, i.e. $H = 0.1$ m and $T = 1.9$ s. The numerical and experimental wave fields are depicted in figure 6.3 for wave gauges 1, 2, 4 and 6. The results of the remaining wave gauges are depicted in appendix C.1.

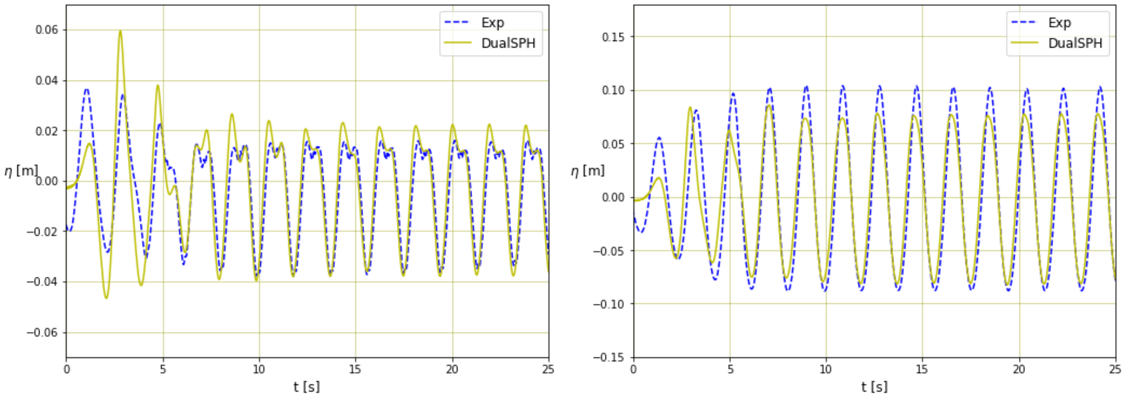

(a) Case E: WG1 (b) Case E: WG3

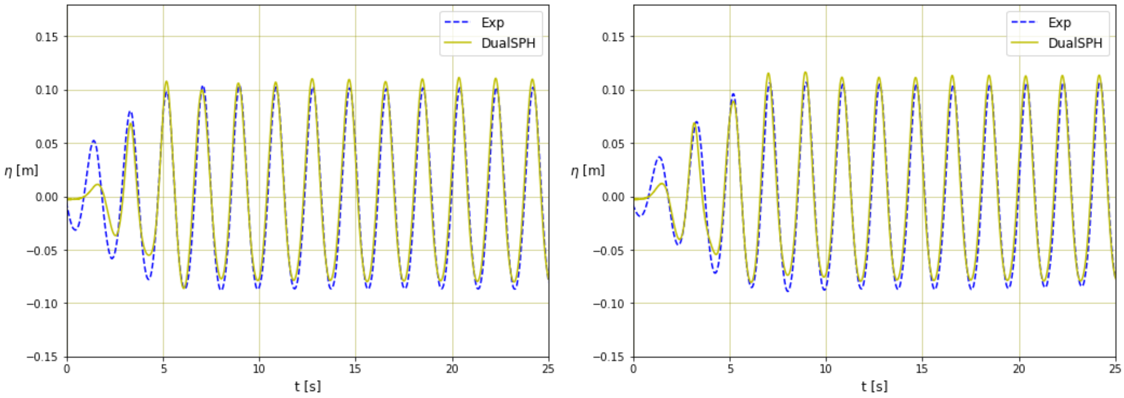

(c) Case E: WG4 (d) Case E: WG6

Figure 6.3: Wave height comparison case E: $H = 0.1$ m, $T = 1.9$ s

Again, excellent agreement is found between the model and the experiment. Even the irregularities in the standing wave pattern caused by the reflected wave for WG1, as shown in figure 6.3a, are well captured by the SPH model. WG3 shows some dissipation in the peak of the wave height, albeit less than for case A. The quantification as tabulated in table 6.2 are obtained for the surface elevation after $t = 7$ s.

WG	R^2 [-]	H_{Exp} $[m]$	H_{sph} $[m]$	Error [%]
1	0.95	0.045	0.054	19.6
2	0.96	0.190	0.159	-16.5
3	0.99	0.188	0.192	0.03
4	0.99	0.189	0.190	0.01
5	0.99	0.126	0.122	-0.04
6	0.99	0.191	0.193	0.01

Table 6.2: Quantification wave field case E: $H = 0.1$ m, $T = 1.9$ s

The quantification shows a very high overlap with the experiment. Compared to case A in table 6.1, with $H = 0.06$ m, it is evident that the accuracy improves when the ratio of the particle size to the wave height is equal or over 10, as explained in subsection 5.1.3. However, it is concluded that SPH performs very well for both cases.

6.1.2 Short overhang

For the structures with overhang the software is switched to LS-Dyna for the reasons provided in chapter 5. This will be indicated in the legends of the figures. There is a minor change in the location of the wave gauges for all overhang conditions as again illustrated in figure 6.4.

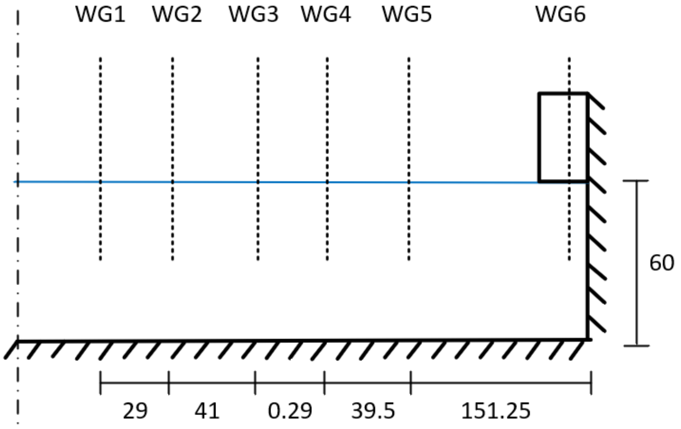

Figure 6.4: Location wave gauges with overhang in [cm]

The wave heights obtained at wave gauges 1, 2, 4 and 6 are presented in figure 6.5 starting with case AS for the short overhang, i.e. $W = 0.1$ m, $H = 0.06$ m, $T = 1.3$ s. Clearly, a less stable wave field is observed now that an overhang is attached to the wall. The standing wave pattern cannot freely develop and thus higher order harmonics are observed and reflected waves show out of phase behaviour for multiple wave gauges, e.g. WG4. SPH seems to reproduce this behaviour up to a certain extent, unless small wave heights are in order resulting in a large inaccuracy as shown in figure 6.5c. Right under the overhang there is an underestimation of the impacting wave height. Moreover, the stability of the wave field is compromised due to the lack of an AWAS. Therefore, it is chosen to analyse a capped wave field between t = 13 s, where the waves are fully developed, and $t = 23$ s, after which the re-reflected waves cause disturbances. The relative errors and goodness of fit are quantified in table 6.3 for this field of interest.

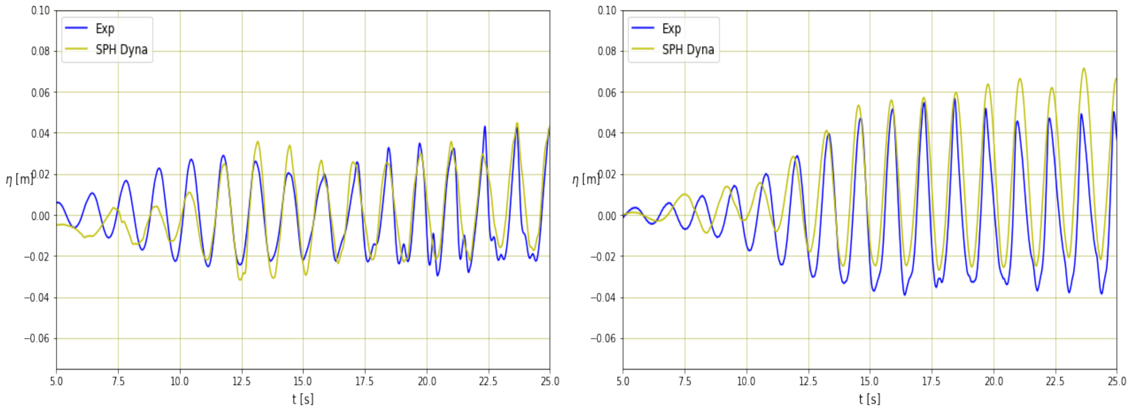

(a) Case AS: WG1 (b) Case AS: WG2

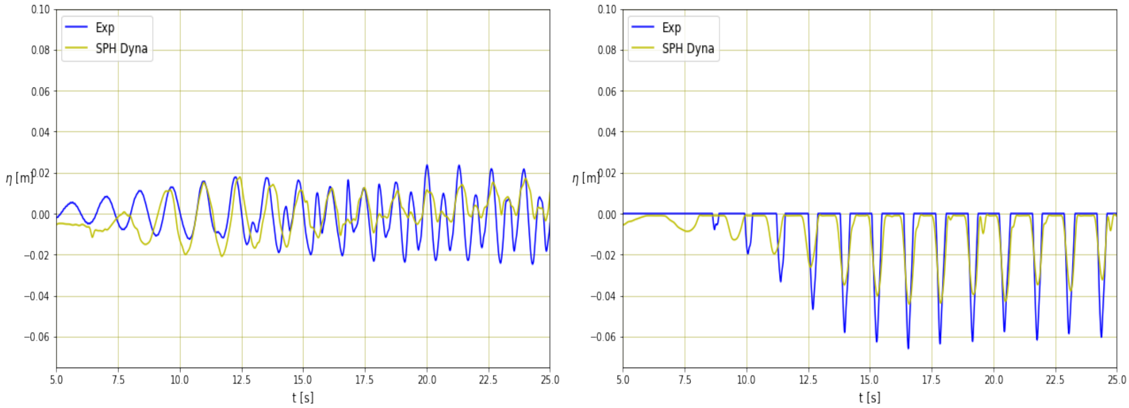

(c) Case AS: WG4 (d) Case AS: WG6

Figure 6.5: Wave height comparison case AS: $H = 0.06$ m, $T = 1.3$ s, $W = 0.1$ m

WG	R^2 [-]	H_{Exp} $[m]$	H_{sph} $[m]$	Error [%]
1	0.67	0.054	0.061	12.15
2	0.61	0.085	0.085	0.81
3	0.63	0.084	0.052	-37.1
4	0.14	0.041	0.021	-49.0
5	0.84	0.099	0.081	-18.0
6	0.74	0.059	0.046	-23.4

Table 6.3: Quantification wave field case AS: $H = 0.06$ m, $T = 1.3$ s, $W = 0.1$ m

From table 6.3 it is concluded that the wave heights are only moderately well reproduced. WG4 shows a bad agreement with the SPH model, which again is caused by the coarse particle size compared to the local surface elevation. Only WG1 and WG2 output an overestimation of the average wave height. Right under the overhang, the wave height is underestimated by approximately 1 particle (0.01 m). A possible explanation for the disagreements is the level of reflection in the model and experiment. Too much energy seems to be lost by the SPH particles impacting the overhang, leading to dissipation of the reflected waves. This results in an underestimation for the gauges closest to the overhang.

To check if the wave field improves with a smaller particle size, the model is rerun using a particle size of $dp = 5$ mm, resulting in a ratio $H/dp = 12$. Figure 6.6 shows the results for WG4, as this returned the worst level of fit, and WG6 as this location determines the impacting wave.

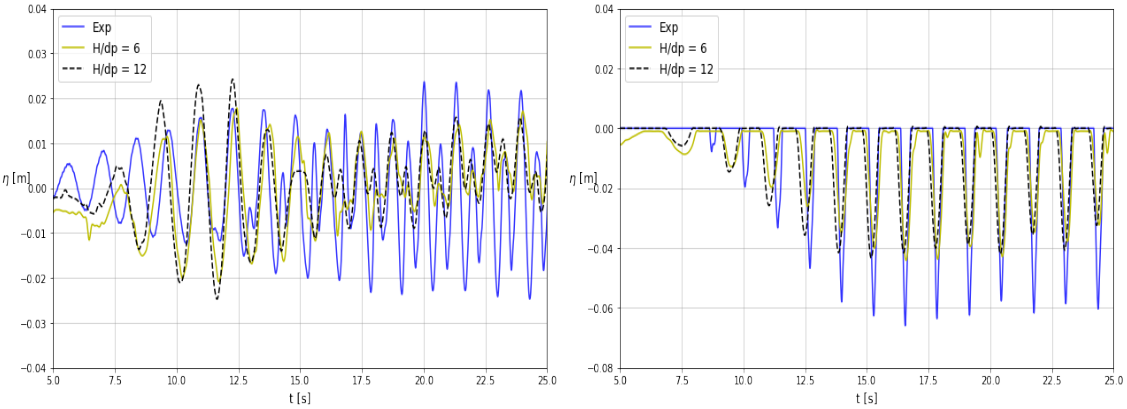

(a) Case AS: WG4

(b) Case AS: WG6

Figure 6.6: Case AS: Comparison WG4 and WG6 for $H/dp = 6$ and 12

Evidently, similar performance is found, which means that both sizes are too coarse to simulate the very small wave height at WG4 (locally, H/dp is smaller than 10). Moreover, the impacting wave at WG6 has an equal wave height and thus it is concluded that pressures at impact will not increase in accuracy for $dp = 5$ mm, in line with the sensitivity analysis of section 5.3. Finally, to obtain the pressures, a sampling frequency of 1 kHz has to be used (section 5.3.3). This will lead to result files that are too big to process in the order of terabytes, which makes further decreasing the particle size infeasible.

When increasing the wave height for case E to 0.1 m, it is expected that the SPH model performs better in the wave generation as the ratio of particle size to wave height of 10 is satisfied. The results for wave gauges 1, 2, 5 and 6 are depicted in figure 6.7.

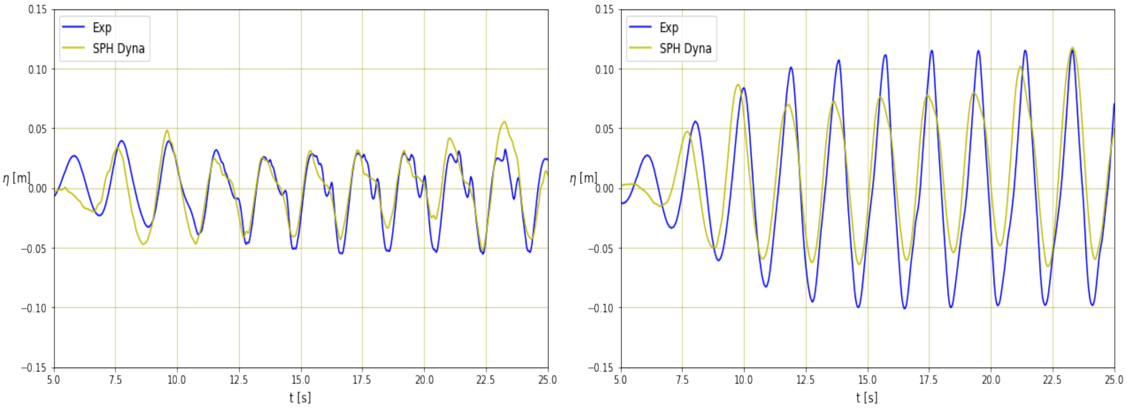

(a) Case ES: WG1

(b) Case ES: WG2

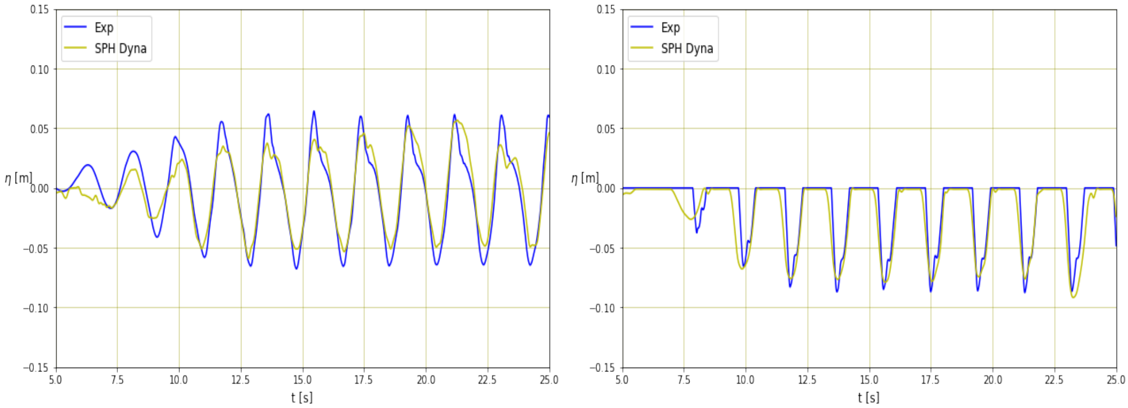

(c) Case ES: WG5 (d) Case ES: WG6

Figure 6.7: Wave height comparison case ES: $H = 0.1$ m, $T = 1.9$ s, $W = 0.1$ m

As anticipated, a better performance is observed in the reproduction of the wave fields. However, re-reflected waves disturb the domain earlier in time due to the increased wave celerity. Now, instead of $t = 23$ s, an amplification of the elevation is observed after $t = 21$ s, which is most clearly visible in wave gauges 1 and 2. Subsequently, the wave field of interest is capped by 2 seconds extra, from $t =$ 13-21 s, for which the model fit and errors are given in table 6.4.

WG	R^2 [-]	H_{Exp} $[m]$	H_{sph} $[m]$	Error [%]
1	0.87	0.078	0.070	-10.5
2	0.74	0.204	0.115	-44.8
3	0.95	0.202	0.166	-20.0
4	0.95	0.185	0.157	-15.3
5	0.92	0.124	0.096	-22.6
6	0.83	0.086	0.077	-10.2

Table 6.4: Quantification wave field case ES: $H = 0.1$ m, $T = 1.3$ s, $W = 0.1$ m

The same behaviour in dissipation is observed, resulting in an underestimation of the surface elevation. However, overall the model performance is more accurate than for case AS with decreased wave height. Right under the overhang, there is still a smaller (by 1 particle size) impacting wave recorded in the model, yet with less of a relative error. Since the particle size now satisfies the desired ratio, it is expected that the underestimation is caused by the loss of energy during the impact of the wave on the overhang, decreasing the level of reflection. Thus, the behaviour at the boundary condition and overall dissipative behaviour of SPH seems to lead to an underestimation of the wave heights. That said, it is concluded that the SPH models show good agreement with the experiment for the majority of the wave gauges.

6.1.3 Longer overhang

In this subsection the configurations with a longer overhang will be treated, where the overhang is lengthened from 10 cm to 20 cm. Starting with case AL, i.e. $H = 0.06$ m and $T = 1.3$ s, the water surface elevations are plotted for wave gauges 1, 2, 4 and 6 in figure 6.8.

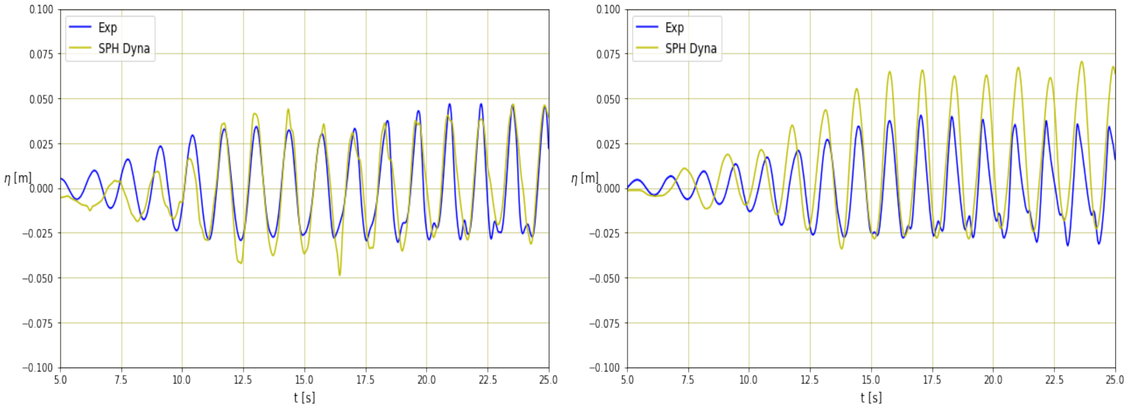

(a) Case AL: WG1 (b) Case AL: WG2

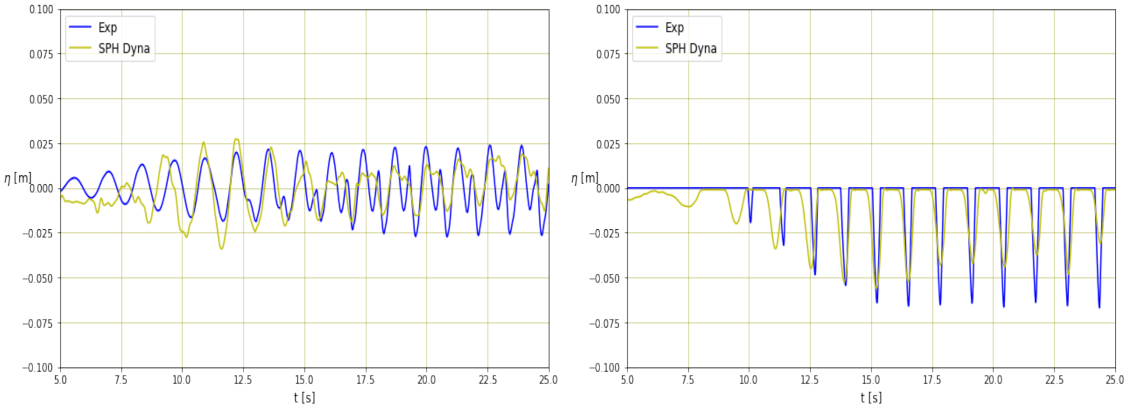

(c) Case AL: WG4 (d) Case AL: WG6

Figure 6.8: Wave height comparison case AL: $H = 0.06$ m, $T = 1.3$ s, $W = 0.2$ m

The surface elevation is only moderately well reproduced, similar to the case with the short overhang. Furthermore, very similar patterns in the shape of the surface elevation are observed in all wave gauges. However, the same disagreement is found as well, with WG4 not being able to accurately capture the irregular and out of phase behaviour of the incoming and reflected waves, WG2 showing and overestimation in the peaks of the waves and WG6 showing a lower numerical impacting wave. Table 6.5 shows the quantification of the wave fields for t = 13-23 s.

WG	R^2 [-]	H_{Exp} $[m]$	H_{sph} $[m]$	Error [%]
1	0.78	0.066	0.071	7.2
2	0.48	0.064	0.087	35.3
3	0.61	0.063	0.042	-33.8
4	0.36	0.045	0.031	-31.4
5	0.87	0.10	0.089	-11.1
6	0.65	0.062	0.048	-22.5

Table 6.5: Quantification wave field case AL: $H = 0.06$ m, $T = 1.3$ s, $W = 0.2$ m

It is observed that the results are rather spurious. Comparing the fits and errors to table 6.3 for the short overhang, it shows very similar behaviour. The impacting wave under the overhang is repeatedly underestimated by one particle size and WG4 shows the least agreement in the model fit. The order of magnitude of the errors is more or less equal, with the exception of WG2, which for this case is significantly overestimated. The 4 wave gauges closest to the overhang are lower than the experimental values.

Finally, the wave height and period are increased once more for the longer overhang configuration. The qualitative comparison between the numerical and experimental values is presented in figure 6.9 for wave gauges 1, 3, 5 and 6.

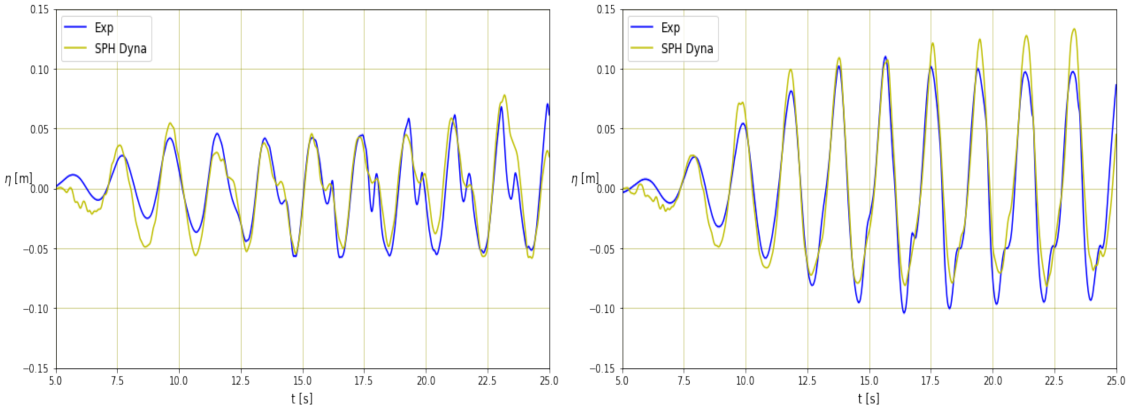

(a) Case EL: WG1 (b) Case EL: WG3

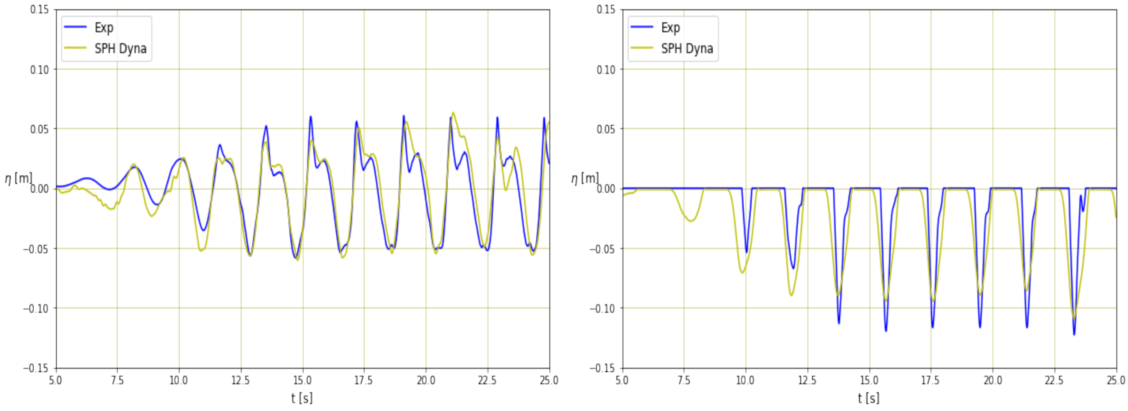

(c) Case EL: WG5 (d) Case EL: WG6

Figure 6.9: Wave height comparison case EL: $H = 0.1$ m, $T = 1.9$ s, $W = 0.2$ m

The level of accuracy of the model fit is drastically increased for the increased wave height. The irregular shape of the elevation is numerically reproduced, best visible in wave gauges 1 and 5. Though interestingly, the impacting wave under the overhang seems to be equally underestimated to the case with reduced wave height. The observations are quantified in table 6.6 for t = 13-21 s.

WG	R^2 [-]	H_{Exp} [m]	H_{sph} [m]	Error [%]
1	0.89	0.103	0.091	-12.4
2	0.73	0.205	0.130	-36.0
3	0.95	0.202	0.193	-4.8
4	0.94	0.191	0.165	-13.8
5	0.91	0.11	0.103	-6.8
6	0.63	0.12	0.092	-21.0

Table 6.6: Quantification wave field case EL: $H = 0.1$ m, $T = 1.9$ s, $W = 0.2$ m

It is evident that the SPH model is in good agreement with the experiment and performs better than case AS for $H = 0.06$ m. The relative errors are lower and the model fit show a strong correlation with the experiment, specifically for wave gauges 3, 4 and 5. However, right under the overhang the surface elevation is deviating by more than one particle size, which is not the behaviour seen in the cases with a short overhang. Apparently, having a wider overhang, causing more particles to interact, results in more dissipation of energy and thus a stronger decrease in the measured surface elevation than for a short overhang.

6.2 Pressure distribution along the wall

In this section, the results of the pressure distributions over the vertical are given and compared to the SPH models. The mean and standard deviation of the peak pressures are calculated to quantify the level of accuracy of the numerical pressures. Additionally, the coefficient of variation is given. For SPH, the values are calculated after the point in time where stability of the pressure distribution is reached. For the experiment, the simulation time lasted multiple minutes. Therefore, a total number of **70 fully developed waves** is chosen to compute the quantification. The hydrostatic pressure is removed for all pressure distributions to isolate the wave induced pressure.

6.2.1 No overhang

The pressure distributions for case A without overhang, i.e. $H = 0.06$ m, $T = 1.3$ s, are shown in figure 6.10 for sensor 1, 4, 6 and 7. The remaining sensors are displayed in appendix C.2. The results are obtained by placing numerical pressure probes at $1.5h_s$ from the wall to omit the effect of the boundary gap on the results, as explained in section 5.1.3)

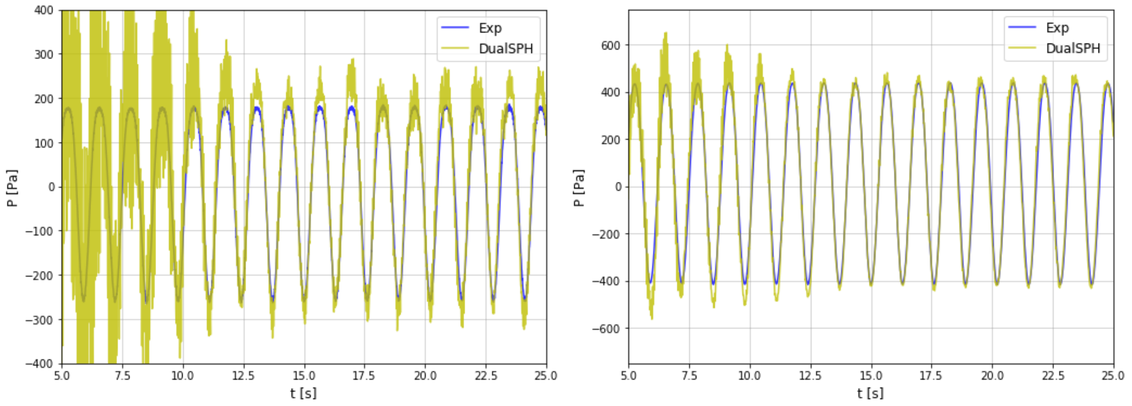

(a) Case A: PS1 (b) Case A: PS4

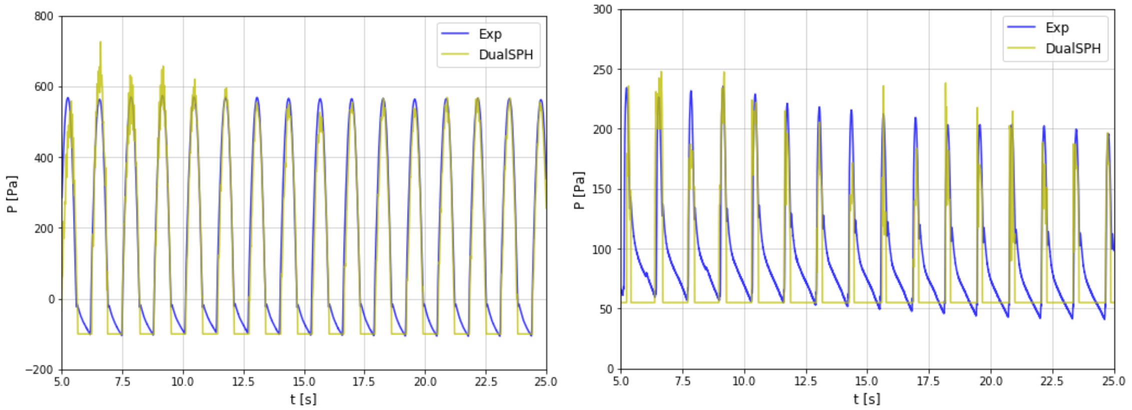

(c) Case A: PS6 (d) Case A: PS7

Figure 6.10: Pressure comparison case A: $H = 0.06$ m, $T = 1.3$ s

A clear generation of noise is observed at the beginning of the simulation, which is more evident for probes placed closer to the bottom. The noise dissipates upwards and thus is less visible in PS4 and only barely noticeable in PS6. This disturbance is caused by the gravity force that is instantly applied at t = 0, shaking up the numerical domain.

DualSPHysics does not provide a ramp function to use a more gradual application of the gravity forcing. However, the pressure does converge and remains stable from t = 12 s and onward. As a result however, an overestimation is observed in PS1. This inaccuracy and noisy response is explained based on the location of the probe, which is slightly below $1.5h_s$ from the bottom, namely at h_s. Therefore, it is located inside the boundary gap, leading to amplified noise and inaccuracy. Note that the bottom parts of figure 6.10c and 6.10d differ, to the water slowly moving down in the experiment resulting in a gradual decrease in pressures, while the particles use an 'On-Off' principle. Table 6.7 shows the quantification of the maximum pressures per sensor (PS).

PS	μ_{exp} [Pa]	σ_{exp} [Pa]	μ_{sph} [Pa]	σ_{sph} [Pa]	σ_{exp}/μ_{exp}	σ_{sph}/μ_{sph}
1	184.83	6.19	259.77	15.63	0.06	0.03
2	304.77	17.98	321.11	12.15	0.06	0.04
3	332.84	22.14	329.55	9.42	0.07	0.03
4	434.45	36.68	464.53	12.29	0.08	0.03
5	493.14	5.97	515.71	18.81	0.01	0.04
6	562.69	6.38	561.16	17.88	0.01	0.03
7	174.23	16.00	204.9	17.87	0.09	0.09

Table 6.7: Maximum pressures case A: $H = 0.06$ m, $T = 1.3$ s

PS1 and PS7 stand out, as these sensors registered the largest deviation between the experiment and model.The former is explained by the noisy distribution due to the aforementioned reasons, of the probe being located inside the earlier specified boundary gap. The latter might be caused by the simulation time. As figure 6.10d shows, there is good agreement between the peak pressures for the domain t = 5-25 s. However, further on in the experiment ($t \approx 50$ s) the pressure drops significantly and reaches a steady state around 175 Pa as further explained in appendix C.3. For the quantification, the average value of 70 fully developed waves are used that produce the pressure of the steady state. This value is chosen as it is considered the most reliable, since the magnitude of the temperature shock is unknown. Overall, very good agreement is shown after the initial noise is dissipated at PS3 and up. Finally, the variation in results is low, proving stable and consistent results.

The same measuring points and number of waves are taken for case E, where the wave height is increased to 0.1 m . The wave period is increased as well to 1.9 s, resulting in an equal wave steepness according to table 4.2. Figure 6.11 depicts the comparison between the numerical and experimental pressure distributions after $t = 11$ s to be consistent with the observations of the wave gauges.

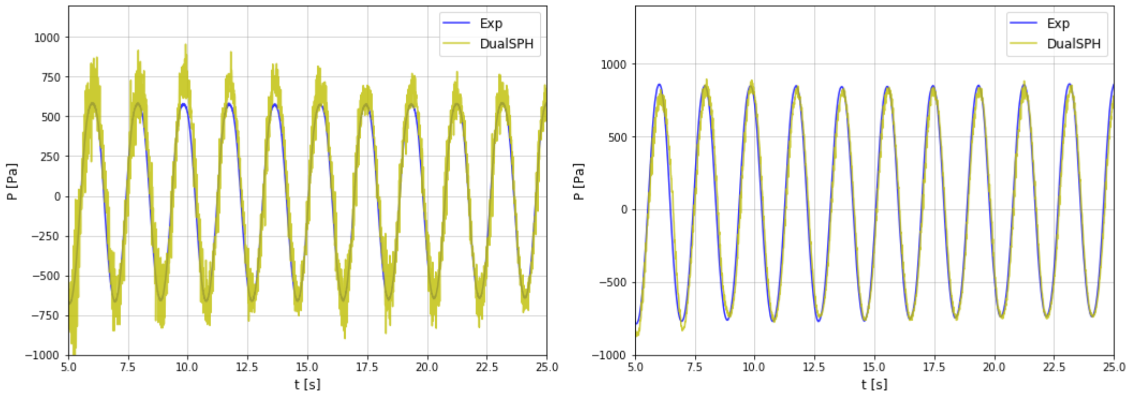

(a) Case E: PS1 (b) Case E: PS4

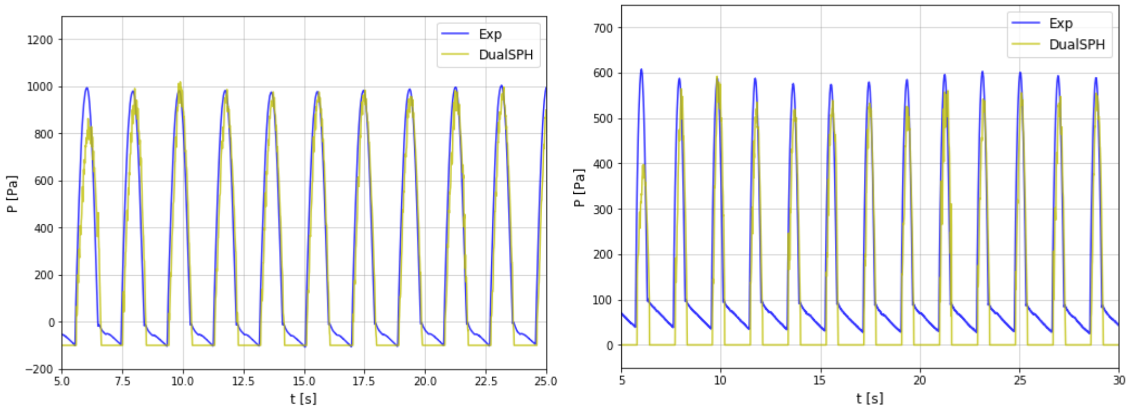

(c) Case E: PS6 (d) Case E: PS7

Figure 6.11: Pressure comparison case E: $H = 0.1$ m, $T = 1.9$ s

The initial noise for PS2 that was so apparent in figure 6.10a seems to be reduced for an increased wave height, which is explained by the higher particle to wave height ratio. Nonetheless, the noisy overestimation is still present, which is caused by the placement of the virtual sensor in the boundary gap. For the other sensors, excellent agreement is once again found between the numerical results and the measurements, which is quantified in table 6.8 after $t = 7$s, in accordance with the observed water level elevations.

PS	μ_{exp} [Pa]	σ_{exp} [Pa]	μ_{sph} [Pa]	σ_{sph} [Pa]	σ_{exp}/μ_{exp}	σ_{sph}/μ_{sph}
1	620.86	11.82	750.10	36.63	0.02	0.05
2	735.90	10.37	779.59	25.55	0.01	0.03
3	769.40	9.19	796.42	16.34	0.01	0.02
4	881.39	9.00	849.60	14.12	0.01	0.02
5	936.72	7.97	956.41	17.0	0.01	0.02
6	1015.27	8.14	989.47	16.73	0.01	0.02
7	572.60	18.85	549.54	5.75	0.03	0.01

Table 6.8: Maximum pressures case E: $H = 0.1$ m, $T = 1.9$ s

The mean maximum pressures confirm the level of accuracy as observed in the graphs, with PS1 being the least precise and having the largest standard deviation. The standard deviation of the model results in about double the coefficient of variation for all sensors besides sensor 9, though this value is still very low. Despite this, stable results are obtained and overall it is concluded that SPH performed accurately. It should be noted that for this case, no pressure drop is observed in the experiment for sensor 8, which increased the accuracy of the SPH model dramatically. A comparison between both experimental results for sensor 8 is presented in appendix C.3.

6.2.2 Short overhang

For the structures with overhang the software is switched to LS-Dyna for the reasons provided in chapter 5. This will be indicated in the legends of the figures. The resulting pressure distribution along the wall, as found by the model and experiment, are displayed in figure 6.12 for the top sensors 3, 4, 5 and 6. Sensor 1 is disregarded in all future analyses, as the model produced unusable results as explained in appendix B.

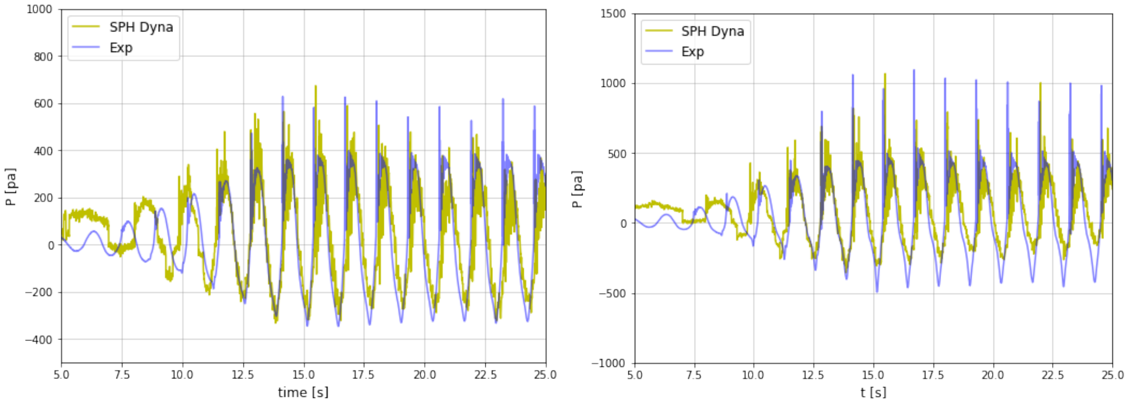

(a) Case AS: PS3

(b) Case AS: PS4

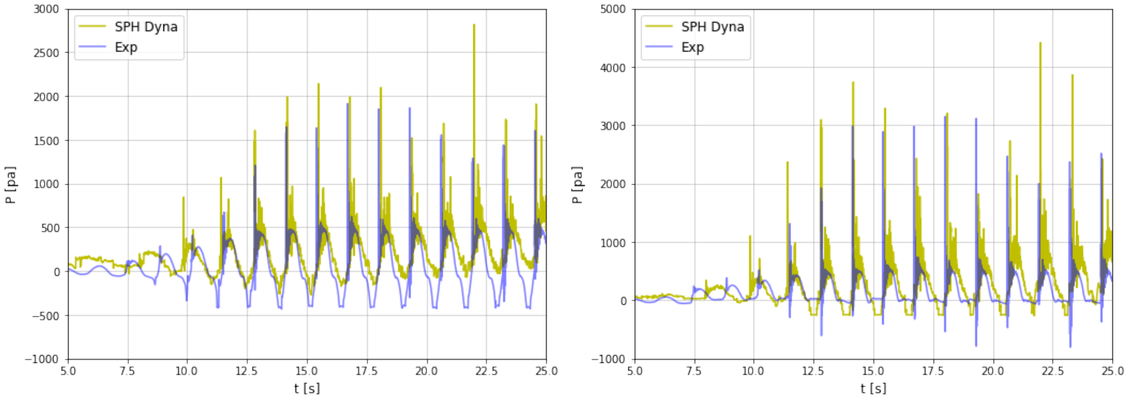

(c) Case AS: PS5

(d) Case AS: PS6

Figure 6.12: Pressure comparison case AS: $H = 0.06$ m, $T = 1.3$ s, $W = 0.1$ m

It is evident that the numerical sensors record significantly more in noise when they are placed closer to the bottom, subject to the highest hydrostatic pressures. Close to the impact region, the noise reduces. It should be noted that LS-Dyna provides a ramp function to gradually apply the gravity force, and so there is no severe initial shake-up of the numerical domain. Furthermore, the experiment will show more impacts at the start of the simulation as the generation of the target wave height happens more gradually compared to SPH. This is corrected by synchronising the time series for the fully developed wave trains. Overall, the physical behaviour of an impact, that is an extreme peak followed by oscillations, is well reproduced by the model. In accordance with figure 6.5, 6-7 peaks can be identified before the domain is disturbed by re-reflections. For these peaks, it is clear that the pressures are overestimated by the numerical model, though provide good agreement with the experiment. The mean peak pressures, standard deviations and coefficient of variation is calculated and tabulated in table 6.9 for 6 peaks in the stable wave field between t = 13-21 s. For the experiment, these values are again computed using 70 fully developed waves.

PS	μ_{exp} [Pa]	σ_{exp} [Pa]	μ_{sph} [Pa]	σ_{sph} [Pa]	σ_{exp}/μ_{exp}	σ_{sph}/μ_{sph}
2	320.00	34.47	352.14	59.63	0.11	0.17
3	461.17	50.11	480.20	73.34	0.11	0.15
4	727.49	91.64	712.83	113.32	0.13	0.16
5	1154.89	180.59	1606.61	218.03	0.16	0.13
6	1912.28	319.85	2497.90	200.50	0.17	0.08

Table 6.9: Maximum pressures case AS: $H = 0.06$ m, $T = 1.3$ s, $W = 0.1$ m

The results show a much stronger variation in the peak pressures than without an overhang, which emphasises the stochastic behaviour of impulsive impact. The coefficient of variation is for both the model and experiment a full order of magnitude greater. Comparing the mean pressures and standard deviation, it can be seen that SPH and the experiment show excellent agreement. For the top two sensors however, a rather strong overestimation is observed in the order of 30%. This is most likely caused by the model being 2D, having rigid boundaries and lacking air, which can provide a cushioning effect.

The pressure distributions for the same upper sensors are depicted in figure 6.13 for case ES, with an increased wave height and wave period.

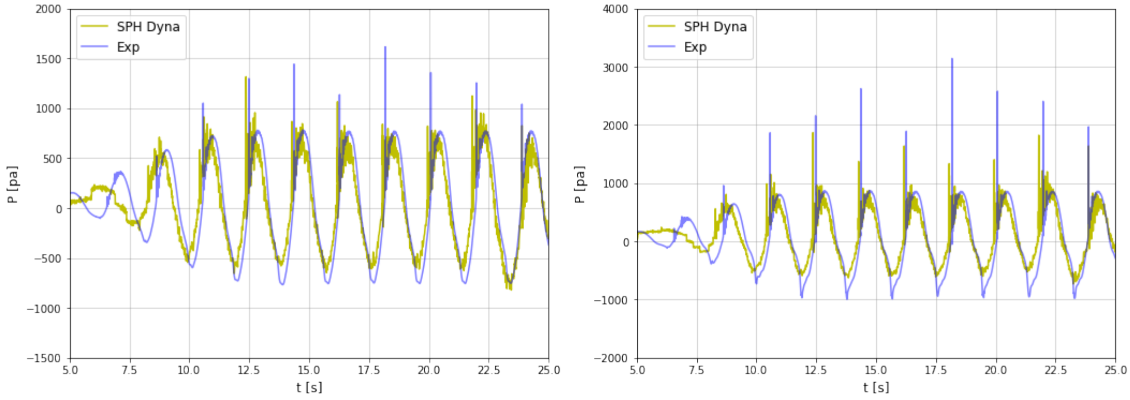

(a) Case ES: PS3 (b) Case ES: PS4

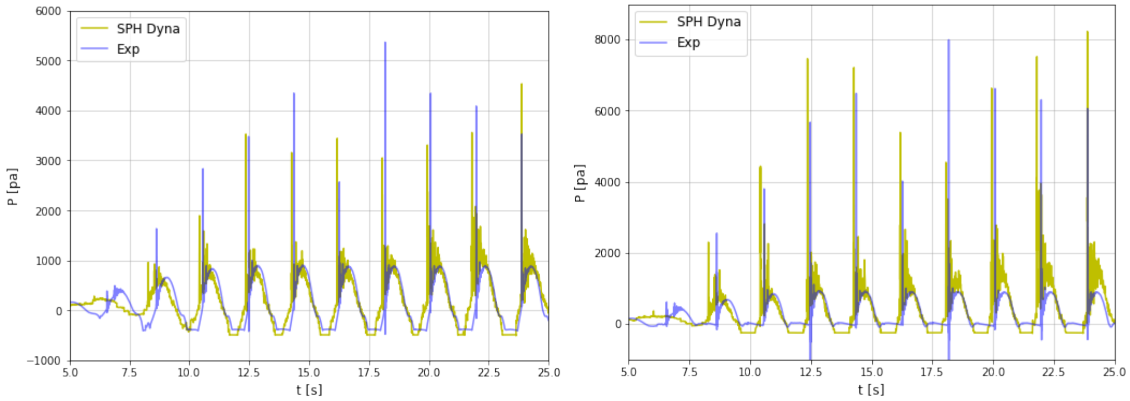

(c) Case ES: PS5 (d) Case ES: PS6

Figure 6.13: Pressure comparison case ES: $H = 0.1$ m, $T = 1.9$ s, $W = 0.1$ m

The pressure distributions show a similar behaviour in terms of noise as for a vertical wall without overhang. When increasing the wave height, less noise is recorded at the lowest senors, which is explained by the increase in particle velocity leading to more movement of the water body. Therefore, there is less vibration like pressure around the sensor. Furthermore, it seems that the SPH model underestimates the peak pressures for all sensors, but the upper most sensor. The maximum pressures of 5 peaks are quantified in table 6.10 for t = 13-21 s.

PS	μ_{exp} [Pa]	σ_{exp} [Pa]	μ_{sph} [Pa]	σ_{sph} [Pa]	σ_{exp}/μ_{exp}	σ_{sph}/μ_{sph}
2	661.10	33.75	598.3	83.75	0.05	0.14
3	1089.97	74.31	780.45	69.24	0.07	0.09
4	1934.32	159.18	1231.10	111.03	0.08	0.09
5	3091.29	300.71	2801.73	305.88	0.10	0.11
6	4488.94	518.11	5231.00	895.73	0.12	0.17

Table 6.10: Maximum pressures case ES: $H = 0.1$ m, $T = 1.9$ s, $W = 0.1$ m

Table 6.10 quantifies the underestimation of the peaks as observed in the pressure distributions. The middle sensors 3 and 4 show the largest error in the order of 30 %. Further up, the pressure converges to the experimental pressure until the top sensor records a peak pressure that is about 15% too high, likely caused by the aforementioned reasons. Furthermore, it is evident that variation of the peak pressures is higher for the SPH models. The increase in variation and underestimation of the peak pressures under the top sensor could be explained by the particle size to overhang ratio. Possibly, there is not sufficient interaction between the complete water body under the overhang and the short overhang itself, leading to dissipation of pressures downwards. Alternatively, the smoothing length could be too small, which results in the few particles interacting with the short overhang not transmitting enough pressure to neighbouring particles.

6.2.3 Longer overhang

Finally, the pressures for the configuration of the longer overhang are compared to the experiment. The results for sensors 3-6 are depicted in figure 6.14.

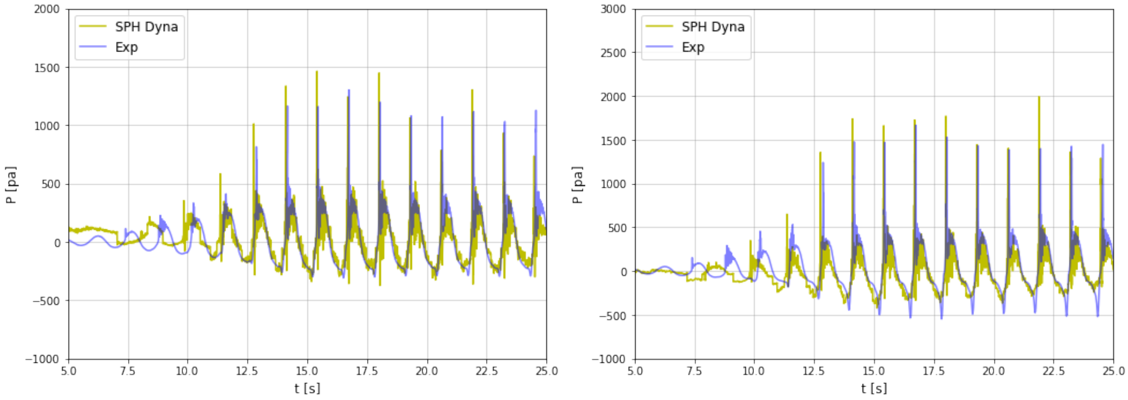

(a) Case AL: PS3 (b) Case AL: PS4

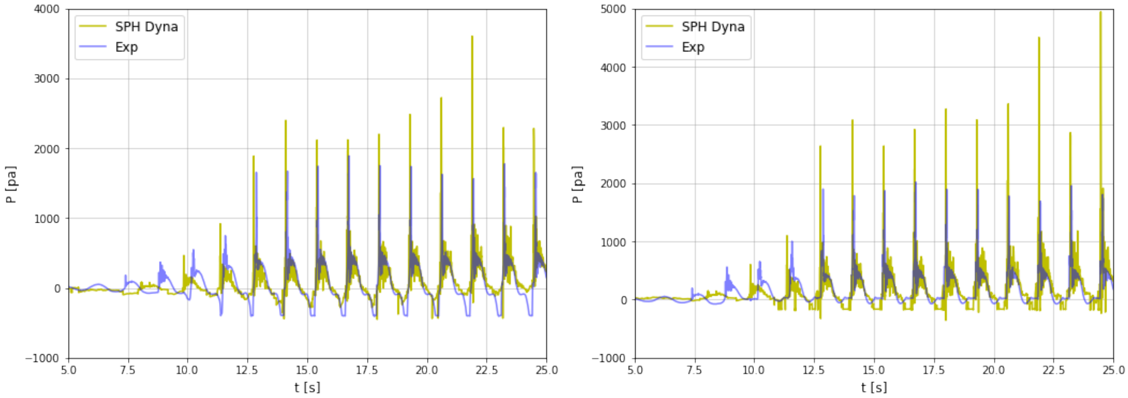

(c) Case AL: PS5 (d) Case AL: PS6

Figure 6.14: Pressure comparison case AL: $H = 0.06$ m, $T = 1.3$ s, $W = 0.2$ m

The numerical and experimental distributions show a very high overlap for the sensors 3 and 4. Excellent agreement is found in both the peaks as the quasi-static component of the distribution, though some noise is recorded for the lowest sensor. On the contrary, a large overshoot is found for the top sensor. The findings are quantified in table 6.11 for t = 13-23 s.

The models reproduced the mean peak pressures for sensor 2-4 accurately, yet show a higher standard deviation leading to more variation. Sensor 5 shows a normal overshoot of approximately 25%, in the range of earlier analysed cases for the short overhang. On the contrary, a large overestimation (about 50%) is observed for the top sensor. A natural reason is the large air pocket that was entrapped for this case in the experiment, as

PS	μ_{exp} [Pa]	σ_{exp} [Pa]	μ_{sph} [Pa]	σ_{sph} [Pa]	σ_{exp}/μ_{exp}	σ_{sph}/μ_{sph}
2	844.68	46.23	1055.39	99.12	0.05	0.09
3	1099.23	64.87	1235.30	145.39	0.06	0.12
4	1407.71	86.85	1536.69	108.69	0.06	0.07
5	1637.58	108.82	2053.55	161.83	0.07	0.08
6	1773.34	124.45	2796.99	201.25	0.07	0.07

Table 6.11: Maximum pressures case AL: H = 0.06 m, T = 1.3 s, W = 0.2 m

described in section 4.1.4, providing a cushioning effect, while the numerical model does not include aeration effects. Furthermore, it stands out that the magnitude of the recorded peaks for the upper two sensors are more stable showing less variation for these conditions. This is also found in the model output, as confirmed by the lower coefficients of variation compared to table 6.9 and 6.10.

Figure 6.15 shows the final pressure distributions as found for case EL, i.e. with an increase of the wave period and wave height.

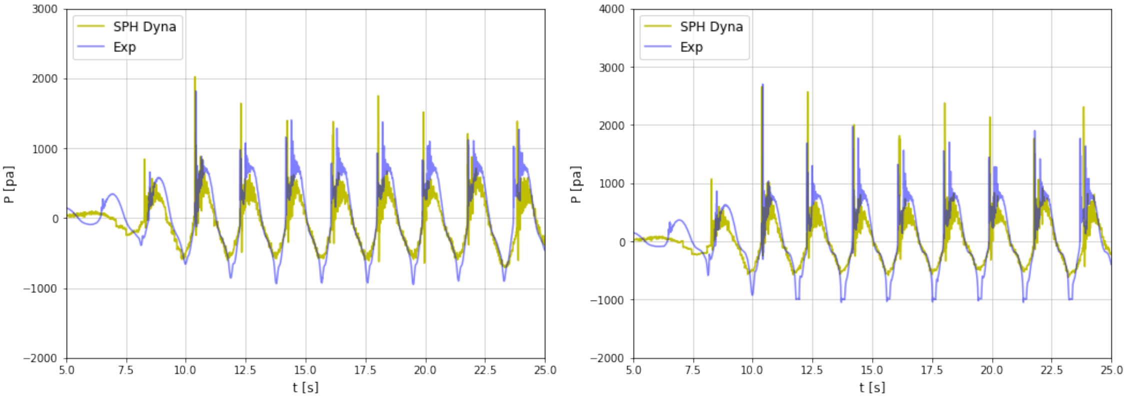

(a) Case EL: PS3

(b) Case EL: PS4

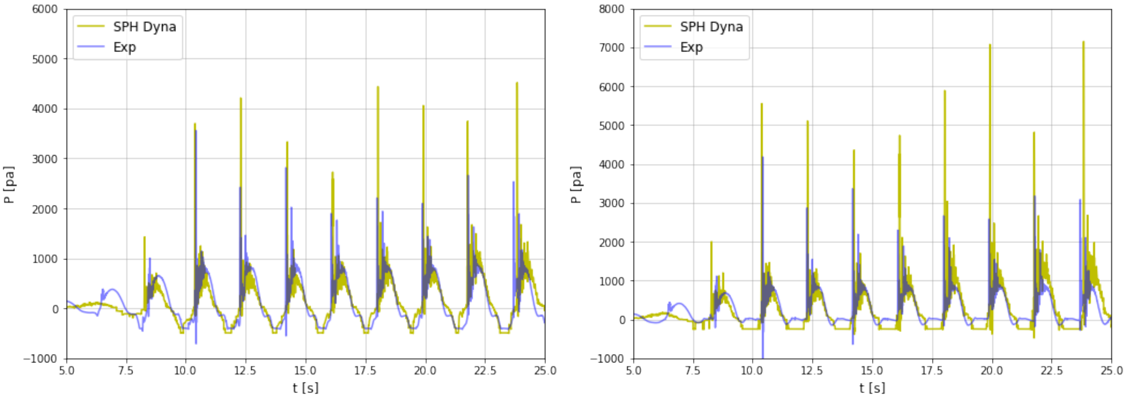

(c) Case EL: PS5

(d) Case EL: PS6

Figure 6.15: Pressure comparison case EL: H = 0.1 m, T = 1.9 s, W = 0.2 m

The first observation that is made is the double peaked distribution in the experiment. This is expected as the observed physical impact, as shown in section 4.1.4, predicted this behaviour. The SPH model did not capture this feature, as the wave hits the surface in a flat manner over the entire width of the overhang, regardless of the wave condition. No air entrapment of variety in the shapes of the impacting waves were observed. This is further elaborated on in section 6.3.4, in which the shapes of the impacting waves is compared. Secondly, a high level of variation is seen for both results, while the upper 2 numerical sensors show pressures which are structurally too high. The maximum pressures for the initial impact (first peaks) are compared in table 6.12 for t = 13-21 s.

PS	μ_{exp} [Pa]	σ_{exp} [Pa]	μ_{sph} [Pa]	σ_{sph} [Pa]	σ_{exp}/μ_{exp}	σ_{sph}/μ_{sph}
2	675.79	133.45	1243.80	190.05	0.20	0.15
3	1002.94	212.58	1542.25	218.40	0.21	0.14
4	1633.48	346.70	2133.07	326.53	0.21	0.15
5	2328.27	458.67	3471.62	527.73	0.20	0.15
6	2830.62	526.02	4878.06	660.27	0.19	0.14

Table 6.12: Maximum pressures case EL: H = 0.1 m, T = 1.9 s, W = 0.2 m

Clearly, this configuration shows by far the highest level of variation, both in the experiment and the model. However, since the total incoming energy in the experiment is spread over two impacts instead of one, it is difficult to fairly compare the outcomes. As an example, the first peak of the experiment of sensor 2 shows only a small initial impact, while the second peak is much larger, namely 1004.11 Pa when recalculated, and almost equal to the SPH model. Therefore, it is more convenient to compare the impulses, which are calculated in the following section.

6.3 Pressure-impulse along the wall

In this section, the impulses, defined as the integral of the impulsive pressure over the impact duration, are calculated over the vertical for the conditions with a short and longer overhang. Firstly, the methodology is explained how the integral is calculated from the experimental and numerical data including a sensitivity analysis. Then, the calculated impulses are compared and quantified.

6.3.1 Methodology impulse calculation

To calculate the impulses, the method proposed by de Almeida Sousa and Hofland (2020) is adopted and applied to the data. In this method, a 3rd order low pass Butterworth filter is applied to isolate the impulsive and quasi-static distribution from the data set. The great benefit of this method is that only the data set directly of the structure with overhang is required, since no model or experiment for the same conditions without overhang to obtain the quasi-static loading is needed. Moreover, any synchronisation issues of using two data sets are avoided, which is crucial to impulsive wave impacts and their short duration. Figure 6.16 shows the determining factors of the pressure-impulse calculation method for any arbitrary case.

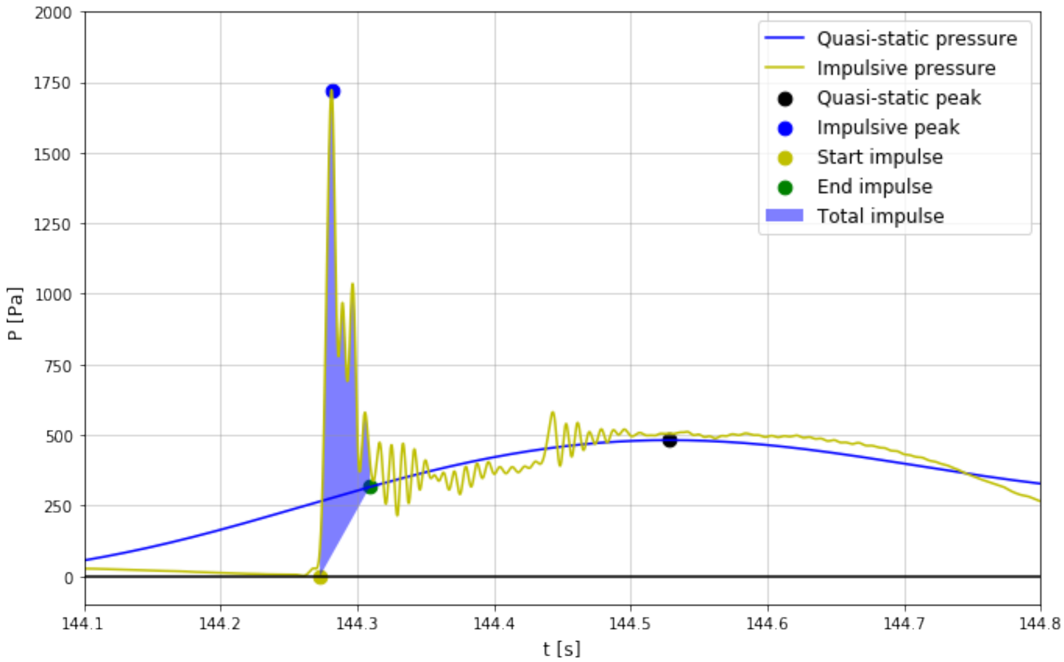

Figure 6.16: Calculation of pressure-impulse

The impulsive pressure (yellow line) is obtained by filtering the data with a cut-off frequency of **100 Hz**. This value is applied to more conveniently obtain the start and end of the impulse without altering either the magnitude of the pressure-impulse or the duration of the impact. The quasi-static part, shown as the blue line is obtained by applying a cut-off frequency of **2/T**, i.e twice the frequency of the wave period of the incident waves. The start and end of the impulse is defined to be dependent on the quasi-static peak, indicated with the black dot. Namely, when the impulsive pressure becomes greater than 20% of the quasi-static peak. Then, the zero pressure value on the black line directly under this point is used as the start of the impulse, as shown with the yellow dot. Similarly, the end of the impulse is defined as the point where the impulsive pressure becomes smaller than 20% of the **difference** between the impulsive and quasi-static pressure, shown as the green dot. Finally, the integral is calculated between the impulsive pressure and the line connecting these start and end points to obtain the pressure-impulse, shown with the shaded area in the figure.

The above mentioned method is applied only for the uppermost sensor directly under the overhang. Hence, the global impact duration obtained from this sensor is governing and applied to all sensors located below on the vertical wall. In other words, the start of the impact of sensor 6 is equal for sensors 1-5. Generally, the end of the impact is equal to the top sensor as well, but only if the condition is valid in which the **difference** between the impulsive and quasi-static pressure is smaller than 20% of the impulsive peak of the impact of interest.

6.3.2 Sensitivity filtering technique

The filtering technique as explained in the previous section, is established using a conditional value of 20% and a cut-off frequency of 100 Hz to obtain the start and end of the impact. A frequency of $2/T$ is used to obtain the quasi-static pressure. Naturally, alternative values can be chosen to obtain the pressure-impulse. In this section, a sensitivity analysis is performed to justify the methodology used in this thesis.

Starting with the cut-off frequency for the impulsive pressure, values are assessed between 150 and 50 Hz. The former is chosen as the upper limit, since this is the cut-off frequency used in the pressure comparisons to remove signal noise. Using values lower than 50 Hz is considered infeasible as the signal would be altered too drastically to represent the impulsive time series. Figure 6.17a depicts the pressure-impulse profiles along the wall for one of the experimental cases (case AS) when the conditional percentage remains 20% and the cut-off frequency is varied.

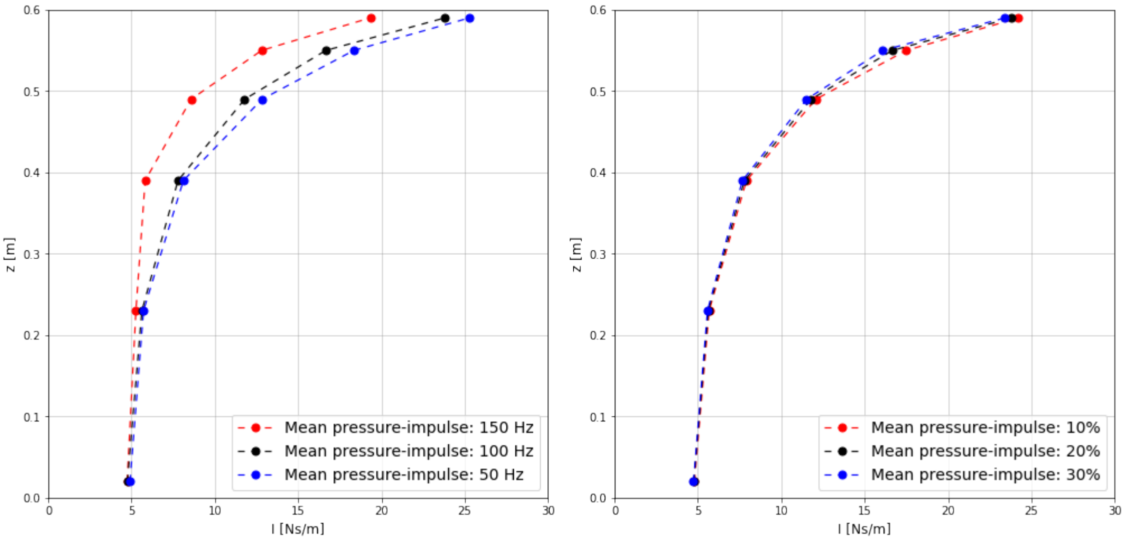

(a) Sensitivity cut-off frequency

(b) Sensitivity conditional percentage

Figure 6.17: Sensitivity pressure-impulse profile to filtering of impulsive time series

The profiles for cut-off frequencies 100 Hz and 50 Hz show a very similar distribution of the pressure-impulse. Due to the similarity in pressure-impulse, 50 Hz is disregarded as it is preferred to alter the original time series as little as possible. For 150 Hz, the profile starts to deviate strongly. For this frequency, the impulsive time series is too noisy to accurately obtain the end of the impact. This issue is resolved when the value is decreased to 100 Hz. Figure 6.18 illustrates a comparison of the two filters, clearly showing the difference in noise. Therefore, it is concluded to use a cut-off frequency of 100 Hz for the optimum results.

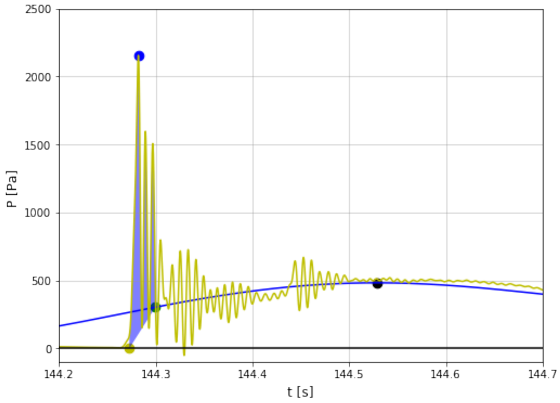

(a) Cut-off frequency of 150 Hz

(b) Cut-off frequency of 100 Hz

Figure 6.18: Difference in noise per cut-off frequency of impulsive time series

Figure 6.17b shows the profiles for various conditional percentages. Evidently, the pressure-impulse remains rather equal when the percentage is either decreased or increased to 10% and 30% respectively. However, for the smaller percentage, difficulties can arise for the time duration as some initial noise can wrongly determine the start of the impact, mostly for the numerical time series. Using a mildly increased value of 20% is more robust for all particularities in different wave loading. For the 30% value, the impact duration will start to become less realistic. Therefore, it is concluded that the conditional percentage of 20% leads to the best results.

Finally, the cut-off frequency of $2/T$ is assessed with the goal to closely approximate the quasi-static wave pressure by means of varying the cut-off frequency.

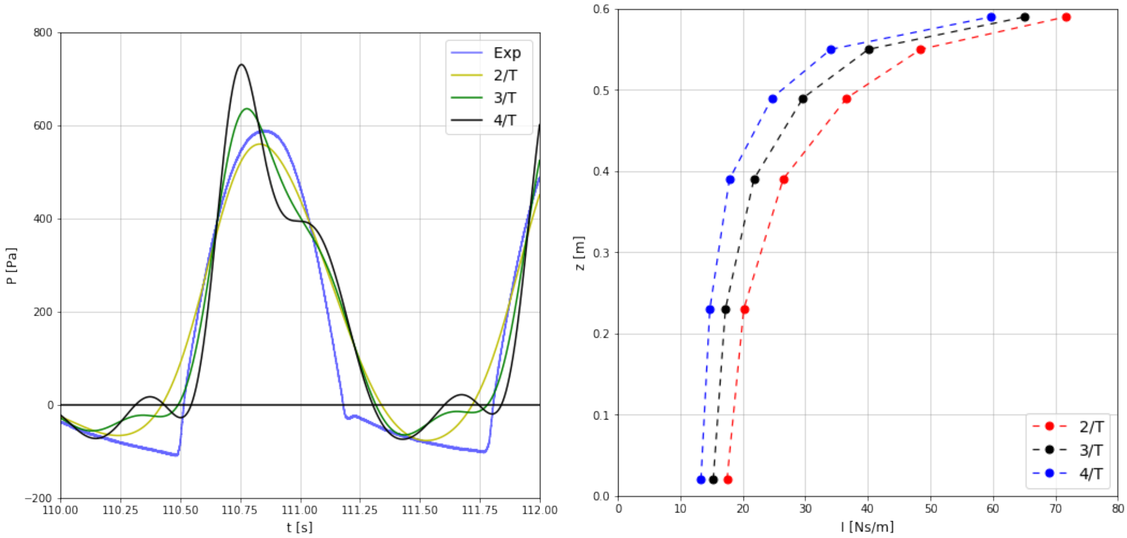

(a) Sensitivity quasi-static pressures

(b) Sensitivity pressure-impulse profile

Figure 6.19: Sensitivity of cut-off frequency quasi-static pressure

The quasi-static pressures for case AS are plotted and compared to the experiment, with the same wave condition without overhang (indicated as EXP). Furthermore, the pressure-impulse profiles along the wall are calculated using the earlier established filter conditions. The results are depicted in figure 6.19. From figure 6.19a, it is clear that frequencies of $3/T$ and over result in an unrealistic representation of the quasi-static time series. Furthermore, the higher frequencies will approach the slope of the impulsive peak pressure, which leads to an earlier end point of the impact. That is why in figure 6.19b, the pressure-impulse profile decreases for a higher cut-off frequency. Therefore, it is concluded that $2/T$ is best suited for the filter technique.

It has to be noted that the shape of the quasi-static time series is an approximation of the true pressure distribution. Especially at the left side of the impact (t = 144.2 - 144.27 s, figure 6.18) the curve is smoothed as a result of the filtering technique. Nonetheless, this has little effect on the magnitude of the pressure-impulse as the determining factors are the distribution of the quasi-static pressure between the start of the impact and the quasi-static peak, and the quasi-static peak itself.

6.3.3 Comparison pressure-impulse results

The pressure-impulse distribution is calculated for all conditions based on the method as described in the previous subsection. The mean values and standard deviations are obtained for 70 fully developed waves in the experiment and 5 to 6 stable impacts in the model to be consistent with section 6.1 and 6.2.

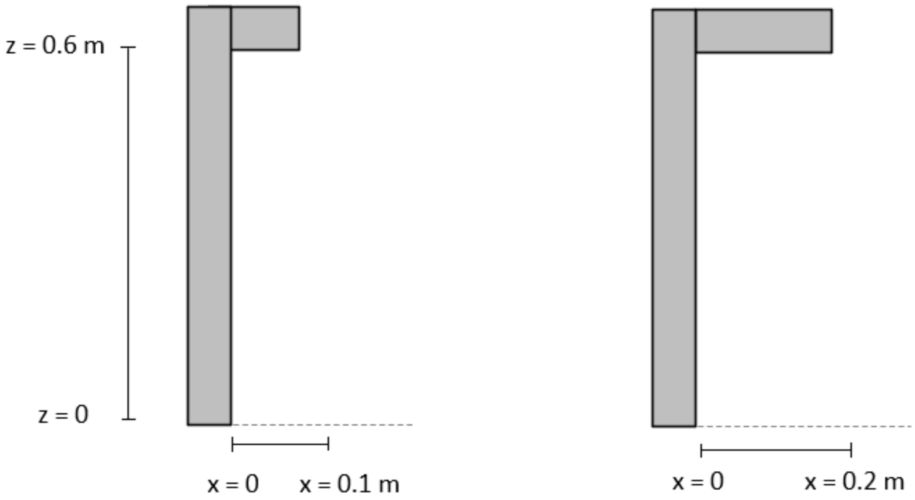

(a) Cross-section short overhang (b) Cross-section longer overhang SPH

Figure 6.20: Cross-sections of overhang configurations

A solution in the form of a powerlaw is fitted through the results to plot the profiles of the mean pressure-impulse along the vertical, which are displayed in figure 6.21 according to the cross sections sketched in figure 6.20. This type of fit best described the obtained data, but is an assumption to be representative of the true profile. The upper figures represent the short overhang configurations and the bottom figures show the longer overhang configurations with H = 0.06 m, T = 1.3 s (left) and H = 0.1 m, T = 1.9 s (right).

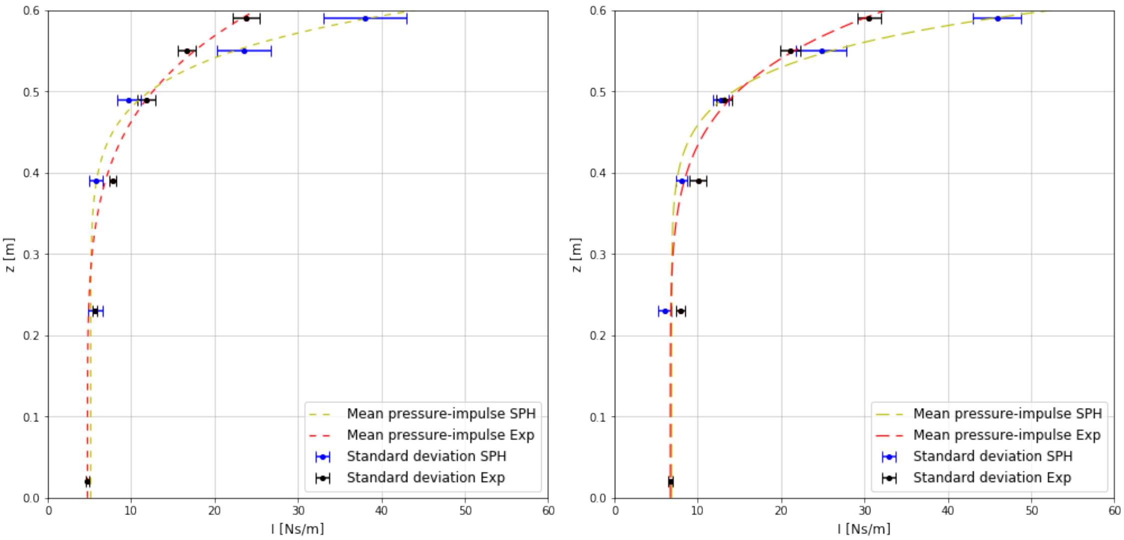

(a) Case AS (b) Case ES

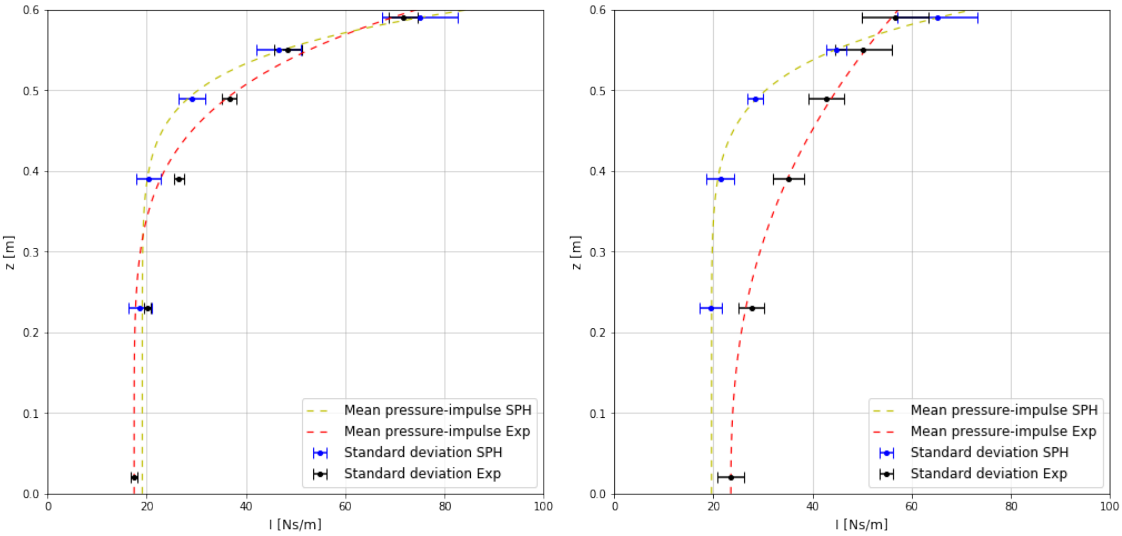

(c) Case AL (d) Case EL

Figure 6.21: Pressure-impulse comparison along the wall

The numerical pressure-impulse profiles show mixed agreement with the experiment. The model shows a very linear distribution until sensor 3 at $z = 0.39$ m. This matches the experimental profiles, except case EL (figure 6.21d). For the short overhang configurations, the same behaviour is observed for both conditions. That is, a mild underestimation between $z = 0.39$ m and 0.49 m and a large overestimation of the top sensor in the order of 50%. For the longer overhang conditions, case AL shows excellent agreement. On the contrary, case EL shows bad agreement for the complete region below $z = 0.55$ m, which is caused by the contribution of the double impact peaks which were absent in the models. That is why the deviation is much stronger in the lower regions of the wall as there, the combined experimental peaks return a higher impulse than just one moderate SPH peak. In conclusion, it is observed that cases AS and ES show good agreement besides the top sensors, case AL shows the highest agreement and case EL the lowest. To understand why this happens, it is vital to analyse the impact duration per case as this defines the pressure-impulse. However, for all cases except EL, SPH would return a reliable force-impulse as analysed in chapter 7.

6.3.4 Physical behaviour of observed impacts

The magnitude of the pressure-impulse is influenced by the shape of the impulsive pressure time series and the width of the pressure-impulse area, which is equal to the impact duration. Moreover, there is a direct correlation between the level of air entrapment and the duration of the impact , as explained in section 2.4.3. Since the SPH model does not include air, it explains the differences in the observed maximum pressures in comparison with the pressure-impulse profiles. The duration per impact is tabulated in table 6.13. Figure 6.22 shows the differences in shape for the longer overhang configurations by plotting a solitary impact. The upper figures show the small wave height condition (H = 0.06 m) and the bottom figures the wave height condition $H = 0.1$ m for the experiment (left) and the SPH models (right).

Case	H [m]	T [s]	W [m]	t_{exp} [ms]	t_{sph} [ms]
AS	0.06	1.3	0.1	31	35
ES	0.1	1.9	0.2	14	31
AL	0.06	1.3	0.1	111	43
EL	0.1	1.9	0.2	39	33

Table 6.13: Impact duration experiment and SPH

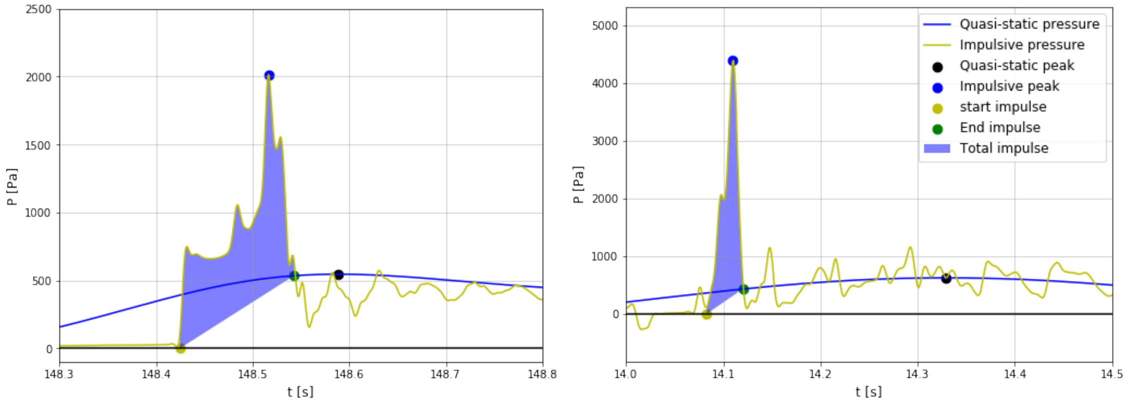

(a) Exp: Case AL (b) SPH: Case AL

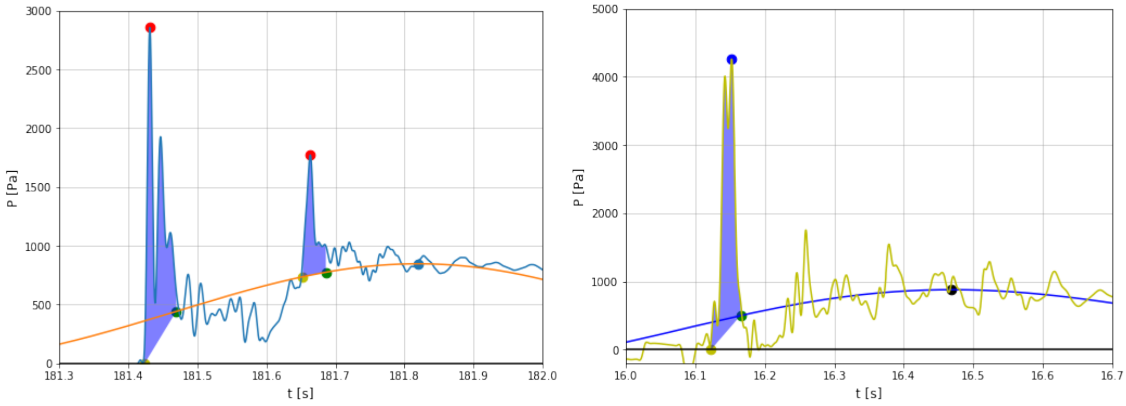

(c) Exp: Case EL (d) SPH: Case EL

Figure 6.22: Physical behaviour of impacts for longer overhang conditions

Evidently, there is a difference in the two conditions for the experiment, while the SPH models both show a very similar impact shape. The large air pocket that was entrapped in case AL is very noticeable in figure 6.22a, stretching out the impact duration leading to a wide pressure-impulse area. In the SPH model, the impact duration is much smaller, which explains why even though the pressure peak is doubled, the pressure-impulse is nearly equal as figure 6.21c showed. Figure 6.23 shows the shape of the impact of the SPH model, compared to the experiment for case AL. For all other cases, SPH showed a similar and nearly flat impact shape, which results in the little variation in impact duration compared to the experiment.

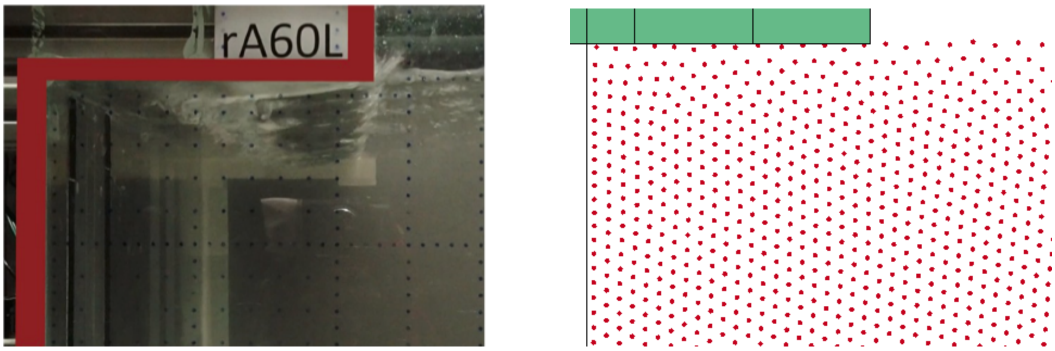

(a) Impact experiment

(b) Impact SPH

Figure 6.23: Difference in impact case AL; Large air pocket vs no air

Analysing case EL, it is observed that the first peak is similar to the SPH model. For the two uppermost sensors, the second peak has only a small contribution to the total impulse. Hence why the corresponding pressure-impulses are similar as well as seen in figure 6.21d. However, the second peak contributes significantly to the total impulse area for the sensors placed lower on the wall, and so it explains the large deviation for z = 0.23-0.55 m.

The short overhang configurations showed the same behaviour for both wave conditions in terms of the pressure-impulse profiles; good agreement for the lower parts along the wall and an overshoot for the top sensor. The overestimation for the top sensors can easily be explained by the difference in impact duration. For case AS, the peak pressures for sensor 5 and 6 were significantly larger in the model than in the experiment as shown in table 6.9. Because the impact duration of the model and experiment is equal, it directly translates the overestimated peak pressures in an overestimation of the pressure impulse. For case ES, the peak pressures of sensor 5 and 6 were very well estimated in the SPH model as seen in table 6.10, yet underestimated for sensors 2-4. However, the impact duration is much shorter in the flip-through type impact in the experiment and so the pressure-impulse 'corrects' itself along the vertical for the underestimating lower sensors.

What is interesting to note is the difference in variability between the mean peak pressures and the corresponding pressure-impulses, when the wave height is increased for the same overhang configuration. Large variation is observed for the peak pressures, while the pressure-impulse seems to be more constant. The absolute differences are calculated for sensor 6, as the highest values are observed here, using tables 6.9 through 6.12 and figure 6.22, and tabulated in table 6.14 per overhang case when the wave height is increased from 0.06 m to 0.1 m. The pressure is indicated as P, the pressure-impulse as PI.

Configuration	$\Delta_{P,exp}$	$\Delta_{PI,exp}$	$\Delta_{P,sph}$	$\Delta_{PI,sph}$
Short	134.7	28.3	109.4	20.8
Longer	60.6	-21.0	74.4	-13.2

Table 6.14: Sensor 6: Variability pressures (P) vs pressure-impulses (PI) in [%]

The differences in variability are far more extreme for the peak pressures, even in the order of 100% for the numerical models. Interestingly, the longer overhang configuration shows a decrease in pressure-impulse for the higher wave height. To gain further insight in the variability, the total mean variability is averaged (indicated with angled brackets) and given in table 6.15 for both overhang configurations.

Configuration	$\left\langle \frac{\sigma_{P,exp}}{\mu_{P,exp}} \right\rangle$	$\left\langle \frac{\sigma_{PI,exp}}{\mu_{PI,exp}} \right\rangle$	$\left\langle \frac{\sigma_{P,sph}}{\mu_{P,sph}} \right\rangle$	$\left\langle \frac{\sigma_{PI,sph}}{\mu_{PI,sph}} \right\rangle$
Short	10.7	6.2	9.1	6.9
Longer	11.5	7.2	13.7	9.2

Table 6.15: Total averaged mean variability pressures (P) vs pressure-impulse (PI) in [%]

Clearly, the averaged mean variability is decreased for both SPH and the experiment for the pressure-impulses, which is in line with de Almeida Sousa and Hofland (2020), where a mean variability of 5.7% was found for the force-impulse, whereas 11.4% was found for the force peaks. Therefore, It is concluded that the pressure-impulses are a more consistent tool, subject to less variance than the peak pressures. Moreover, the influence of air is mitigated, which makes the numerical model more reliable. This is based on the fact that a large air pocket drastically decreases the peak pressure, but increases the duration, leading to a similar pressure-impulse as a flip-through type impact with no air pocket, but a very short duration.

6.4 Pressure-impulse on overhang

This section analyses the obtained pressure distribution and the calculated pressure-impulse on the overhang for all 4 conditions. In the experiment, only one sensor was placed directly on the overhang, i.e. sensor 7 at a 7 cm and 17 cm offset from the wall for the short and longer overhang respectively. The top sensor on the wall (sensor 6) will be used as the representative upward pressure on the overhang since pressure behaves omnidirectionally. However, in reality the pressure might slightly differ directly under the overhang due to expansion and entrapment of air pockets.

6.4.1 Pressure distribution

Figure 6.24 shows the numerical and experimental results for sensor 7 on the short overhang (upper figures) and longer overhang (bottom figures) for wave condition A (left) and E (right).

Interestingly, an underestimation is now observed for cases ES (figure 6.24b), and AL (figure 6.24c), while for the uppermost sensor on the wall for the same cases, an overestimation was found, especially for case AL. This can be explained by how and where the wave hits the structure. In the numerical model, the point of impact is similar for all configurations, which is in the corner of the wall and overhang. That is where most of the pressure accumulates and where the maximum impact velocity is found. Further away from that point, some pressure dissipates, the impact velocity reduces, and so lower

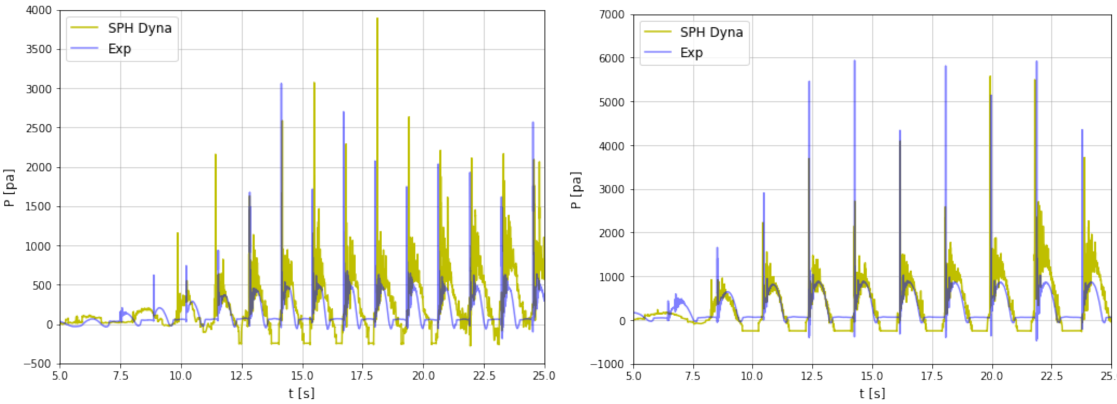

(a) AS: $H = 0.06$ m, $T = 1.3$ s, $W = 0.1$ m (b) ES: $H = 0.1$ m, $T = 1.9$ s, $W = 0.1$ m

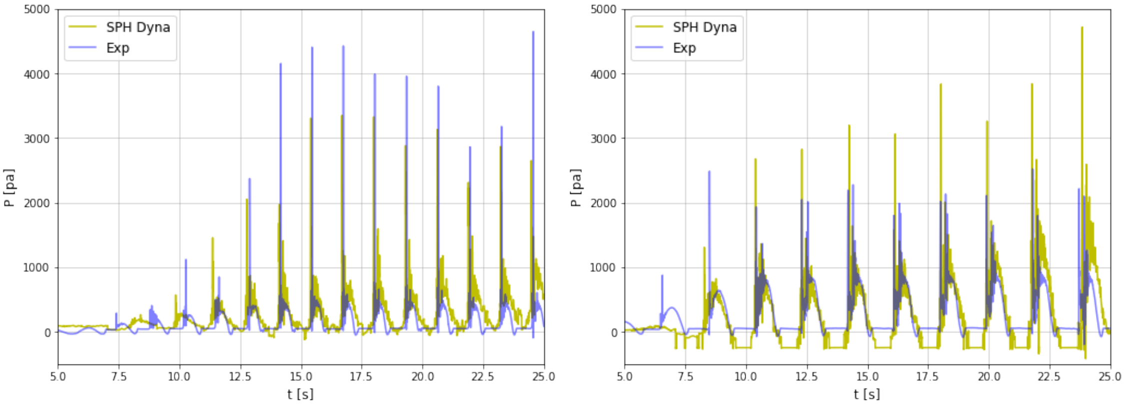

(c) AL: $H = 0.06$ m, $T = 1.3$ s, $W = 0.2$ m (d) EL: $H = 0.1$ m, $T = 1.9$ s, $W = 0.2$ m

Figure 6.24: Pressure comparison on overhang for sensor 7

values are found for sensor 7. Naturally, this effect is amplified for a longer overhang. The numerical velocity fields during impact are further analysed in section 6.5. In contrast to the model, all cases in the experiment have different wave impact types. Reasoning for the observed deviations per case is given below in order of figures 6.24 a through d, keeping in mind the decrease in observed numerical pressures for sensor 7 compared to sensor 6.

- **Case AS**: Wave was observed to hit the end of the overhang first with only a small air pocket at the wall. As a result, the pressure measured at sensor 7 is very similar to sensor 6, and so the overestimation by the SPH model is slightly reduced compared to table 6.9
- **Case ES**: Flip-through type impact observed in experiment with all air expelled. Hence, very equal pressures are found for sensor 6 and 7, while the SPH model shows largely reduced values. Hence why an overestimation is observed
- **Case AL**: Wave impacts far end of the overhang creating a large air pocket over the entire width. Therefore, higher pressures are observed for sensor 7 close to the impact being the least affected by the cushioning effect, and so an underestimation of the model is observed
- **Case EL**: A steep wave hits roughly in the middle of the structure, creating a second but almost equally strong impact near the wall. Subsequently, the reduced values of the SPH model show less of, but still an overestimation of the double peaked experimental distribution

The findings are supported by calculating the mean maximum pressures, standard deviations and coefficients of variation for 70 fully developed waves for the experiment and 4-5 stable impacts for the model, depending on the wave period.

Case	μ_{exp} [Pa]	σ_{exp} [Pa]	μ_{sph} [Pa]	σ_{sph} [Pa]	σ_{exp}/μ_{exp}	σ_{sph}/μ_{sph}
AS	1848.17	368.62	2362.53	465.41	0.19	0.20
ES	4226.34	413.55	3534.11	478.51	0.10	0.14
AL	3475.99	481.16	2840.09	501.96	0.14	0.18
EL	2328.27	458.67	3035.06	451.07	0.20	0.15

Table 6.16: Maximum pressures on the overhang for sensor 7

The coefficients of variation seem to be in the same order as sensor 6, as could be expected since both are located in the impact region. A clear decrease is visible in the SPH models for all cases compared to sensor 6.

6.4.2 Pressure-impulse

The impulsive pressures and impact duration are integrated for sensor 6 and 7 for the experiments and numerical models to obtain the pressure-impulses, with an extra numerical pressure probe placed halfway the overhang to obtain a more reliable profile. Then, a solution in the form of a powerlaw is fitted through the data once the mean values and standard deviations are computed, similar to the profiles along the wall, with zero pressure-impulse as a starting point at $x = 0.1$ m and $x = 0.2$ m for the short and longer overhang respectively. This profile is an assumption of the true solution and a result of the fit function. The results are depicted in figure 6.25.

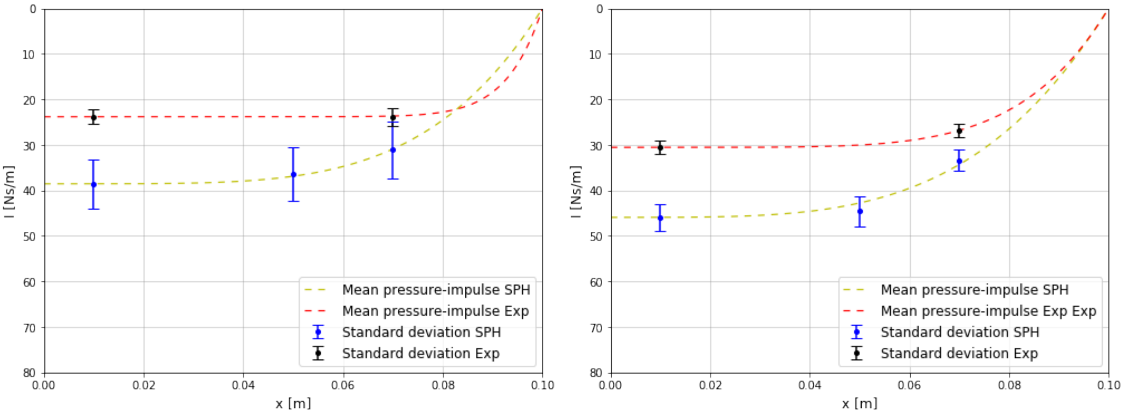

(a) Case AS (b) Case ES

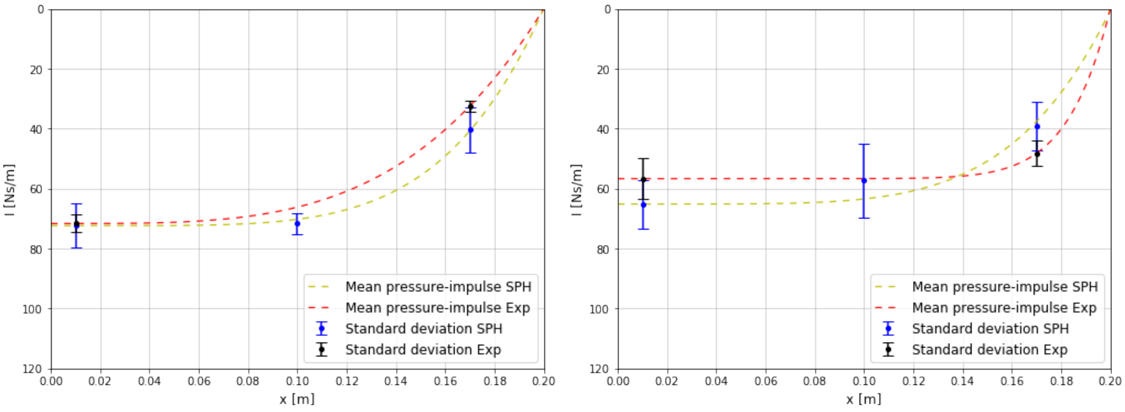

(c) Case AL (d) Case EL

Figure 6.25: Pressure-impulse comparison on overhang

From the figure, it is evident that mixed agreement is found, similar to the pressure-impulse along the wall. For the shorter overhang configurations (top figures), it is logical that the experimental values show little variation, as the impact acts almost instantaneously over the entire width. In case of EL, a double impact was observed, with the first hit being close to sensor 7. Therefore, little variation is found between the values. For case AL, significantly higher pressures were found for sensor 7 on the overhang compared to sensor 6, close to the wall, since the wave impacted the far end of the structure first. However, the duration was found to be almost halved, i.e. 79 ms, which explains the decrease in pressure-impulse. For the numerical models, the same trend is observed for all cases, which is a decrease in magnitude along the width of the overhang. This decrease is amplified for the longer overhang configurations

6.5 Analysis of velocity fields

In section 6.4.1, it was observed that the SPH pressures decreased noticeably stronger than the experiment for the sensors placed further away from the wall under the overhang. In this section, an explanation is sought by analysing the velocity fields during impact. Furthermore, the assumptions of the theoretical models in terms of velocity (circular, constant upward velocity for pressure-impulse model, no horizontal impact. Split x- and z-contribution for conceptual model over rectangular and triangular area under overhang) are compared to SPH to either validate or to propose modifications.

6.5.1 Numerical velocity field during impact

The decrease in pressure over the width of the overhang is dependent on the impact velocities. As aforementioned, it was observed in the model that the point of wave impact is consistently located in the corner near the transition of the wall into the overhang, while for the experiment varying impact points are observed. At this moment, no experimental data is available of the velocity fields. Therefore, the analysis is conduced numerically. Table 6.17 presents the average of the maximum numerical velocity per wave impact and its comparison to the theoretical velocities as derived from LWT.

Case	H [m]	T [s]	W [m]	V_{SPH} [m/s]	V_{LWT} [m/s]
AS	0.06	1.3	0.1	0.278	0.289
ES	0.1	1.9	0.2	0.340	0.331
AL	0.06	1.3	0.1	0.281	0.289
EL	0.1	1.9	0.2	0.324	0.331

Table 6.17: Numerical and theoretical impact velocities

Evidently, it is found that the numerical upward impact velocities at the waterline are very close to the theory for all cases. In determining the impulses on the wall and overhang, it is important to analyse how the body of water is stopped against the structure and with what magnitude. In doing so, a distribution of velocities is obtained which can explain the behaviour of the model. In this analysis, the overhang configurations are used with wave condition E ($H = 0.1$ m). The stoppage of the water column at impact is determined by subtracting the velocities just after impact occurred from the velocity just before the impact. In simpler words, the difference in velocity is calculated caused by the impact. This method is applied for a grid with a resolution equal to the particle size, i.e. for x- and z-coordinates with a spacing of 0.01 m. Figure 6.26 presents contour plots of the difference in velocity before and after impact for the longer overhang, split up in x- and and z-direction. The results for the short overhang are given in appendix C.4. Note that the plots are extended to twice the overhang width and that the velocities are denoted with u.

The results are compared to the circular profile of the pressure-impulse model (Wood & Peregrine, 1996), in which only the z-velocity is considered and assumed constant, as depicted in figure 2.20, and the conceptual model (Tuin, 2019) in which the contribution of the x-velocity is assumed rectangular and of the z-velocity triangular, after which these control volumes are integrated for the velocities described by LWT as depicted in figure 2.21.

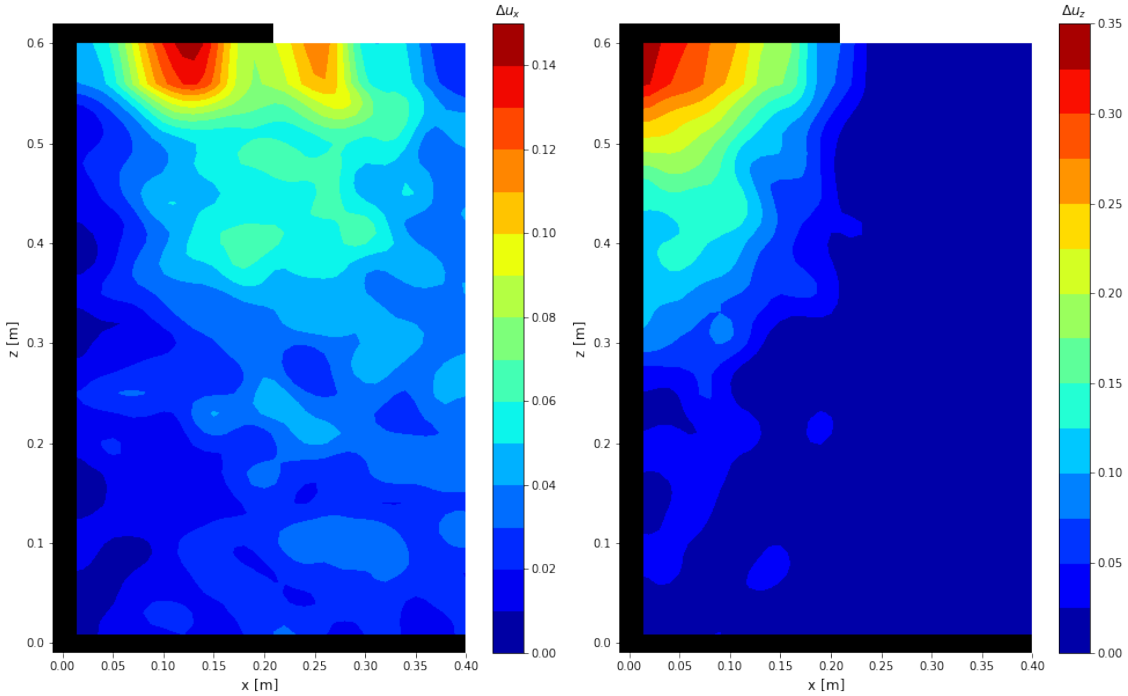

(a) Δu in x-direction [m/s] (b) Δu in z-direction [m/s]

Figure 6.26: Stoppage of velocities at impact for case EL

Clearly, not only the z-velocity is obstructed during impact. A contribution of the x-velocity to the impulse is observed, which is concentrated at around $x = 0.15$ m. This contribution is not just limited to the width of the overhang, but extents past it. Note that some noise is observed right next to the overhang at $x = 0.25$ m, which is explained by the particles 'feeling' the hit on the side of the overhang. For the shorter overhang, this sideways impact dominates the contour plot in x-direction, which makes it difficult to determine how the water is stopped for the x-directional velocities. However, the longer overhang shows that the contribution of the x-velocity becomes more or less insignificant past $x = 0.30$ m, which is at $1.5W$.

For the vertical velocity, the figure supports the earlier observation that the point of impact is indeed in the corner of the wall and overhang, as here the velocity is stopped in its entirety. Interestingly, a clear reduction is observed over the width of the overhang, until zero is found right next to it, which is logical as no z-directional velocity is abruptly stopped without an overhang present. The observed distribution explains the decrease in pressures over the overhang width as found in section 6.4.1.

In section 2.5.2, it was discussed what velocity fields are assumed in the pressure-impulse and conceptual model. The pressure-impulse model assumes a circular area with a constant vertical impact velocity over the entire width of the overhang, and disregards any contribution of the horizontal velocity. This assumption is only partly supported by the numerical model, as a clear decrease in upward velocity over the overhang width and depth is observed. The contour lines do show an approximately semi-circular profile for the highest velocities. For the short overhang width, the same observation is made in figure C.9b, i.e. circular shaped upward velocities decreasing just below the overhang and a contribution is found of the x-velocity to the total impulse. In the conceptual model, the impulse is split into a contribution of the x-velocities and z-velocities, which is supported by the numerical model. However, the triangular area of integration over the full height is too conservative as this is not found in the contour plots. Exploratory calculations by means of direct integration of the numerical velocity field is carried out in the next subsection to optimise the areas of integration for the conceptual models.

6.5.2 Numerical velocity field before impact

To propose a new area of integration to modify the conceptual model, it is vital to first analyse the velocity fields just before impact occurs to compare them with the theoretical velocities derived from LWT. These can be obtained by applying the grid dimensions to equations 2.5 and 2.6. Figure 6.27 compares the contour plots of the SPH model with LWT for the longer overhang configuration. Appendix C.4 includes the short overhang. The top figures show the x-velocities and the bottom figures the z-velocities.

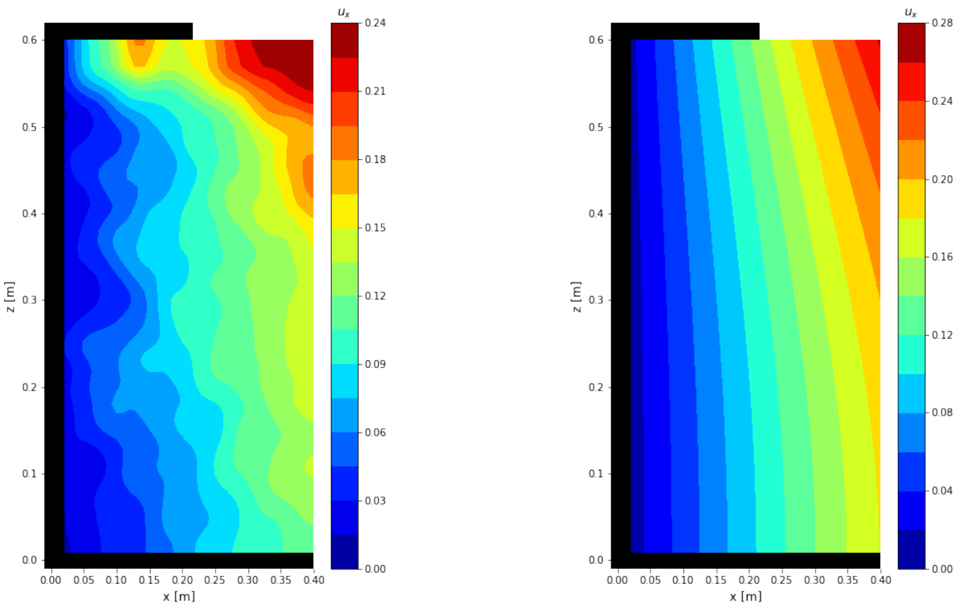

(a) u_x: SPH (b) u_x: LWT

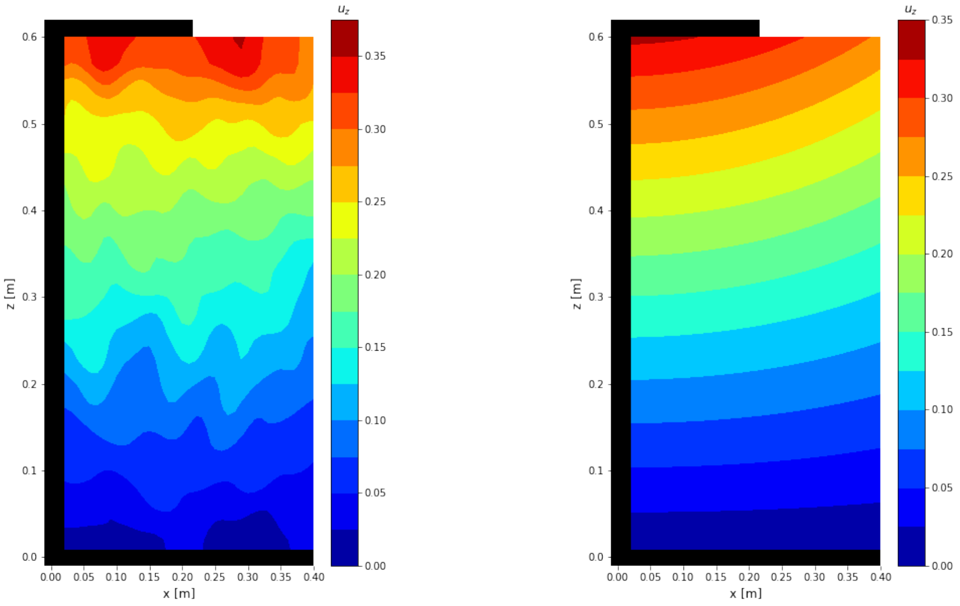

(c) u_z: SPH (d) u_z: LWT

Figure 6.27: Numerical velocity field before impact compared to LWT for case EL

Figure 6.27 shows good agreement between the numerical and theoretical velocity fields overall, although it can be observed that the velocities in x-direction show denser contours close to the overhang. Nevertheless, the magnitude of the theoretical velocities is well approximated, which validates the direct integration of the velocities to optimize the conceptual model for these overhang configurations. In doing so, the triangular area is adopted from the theory for simplicity, but the z-location at which the area starts is made variable and is expressed relative to overhang width W. The x-velocities are still integrated by means of a rectangular distribution, but with a constant width equal to $1.5W$ as found in the previous subsection for the longer overhang, which is adopted for the short configuration as no conclusion could be drawn based on its contour plot, as explained in appendix C.4. Figure 6.28 shows the results for the short (left) and longer overhang (right) with the y-axis presenting the height of the triangular area with respect to the overhang width W. $6W$ equals full height as used in the original model and 0 means the location of the overhang, i.e. no contribution of the z-velocity as the height of the triangular area is zero.. Note that the force-impulse on the wall, obtained by integration of the pressure-impulse profile as further elaborated in chapter 7, is added as a vertical line for both the SPH model and the experiment.

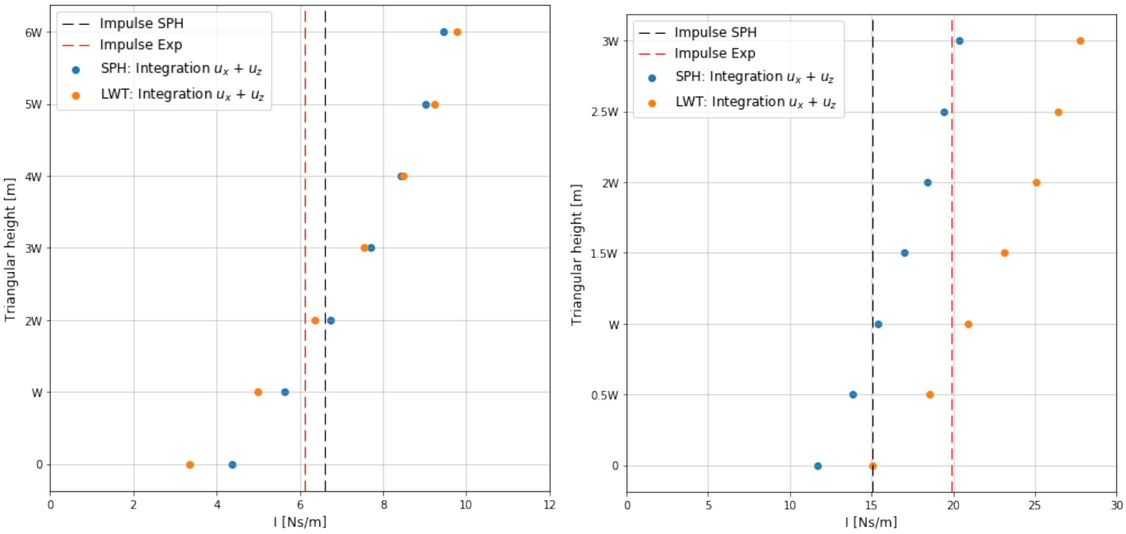

(a) Short overhang configuration

(b) Longer overhang configuration

Figure 6.28: Optimisation conceptual model by direct integration of numerical velocity fields

From figure 6.28, it is observed that both LWT and SPH intersect with their impulse at a triangular height of $2W$ for the short overhang, i.e. between $z = 0.4$ and 0.6 m. In case of the longer overhang, there is a noticeably stronger deviation between LWT and SPH. However, both the model and the theory intersect with their impulse at the same triangular height equal to $1.5W$. In chapter 7, the force-impulses will be calculated using the original conceptual model and the modified model with optimised areas of integration. The newly found areas of integration are visualised in figure 6.29.

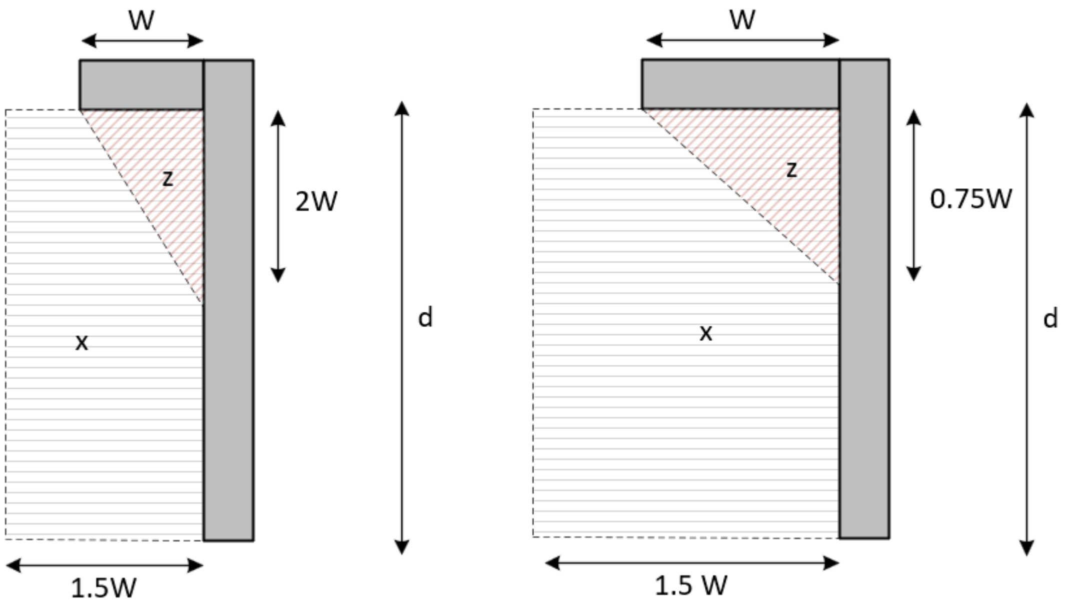

(a) Short overhang configuration (b) Longer overhang configuration

Figure 6.29: Conceptual model: Optimised areas of integration

6.6 Summary and discussion results

For the vertical wall without overhang modelled in DualSPHysics, it is concluded that SPH can accurately predict pulsating pressures by standing waves. The numerical wave heights at various locations in the flume showed almost a 1 to 1 correlation with the physical experiment and excellent agreement was found in the pressure distributions. The implementation of an AWAS provided a stable solution for longer time series. However, close to the bottom some initial noise was observed by the gravity force being instantly applied at $t = 0$. This noise could be reduced by applying a ramp function to the gravity force. Finally, pressure probes near the bottom registered a noisy response, which dissipated further up. Special care should be given to the placement of the probes and the boundary gap to increase accuracy.

For the structure with an overhang modelled in LS-Dyna, the wave fields showed more deviation. No AWAS could be used, leading to re-reflective waves disturbing the domain after some time in the simulation depending on the wave conditions. The accuracy increased significantly when a particle size to wave height ratio of 10 was applied. The pressures along the wall were overall well reproduced by the models. However, an overestimation was found repeatedly for the upper sensors, due to a lack of air in the model, the model being 2D and having rigid boundaries.

The pressures found under the overhang showed a more spurious agreement and for the first time the model returned an underestimation of peak pressures at 7 and 17 cm from the wall cases ES and AL. This was explained by the point of impact of the wave, which was in the corner of the overhang and wall for all conditions in the model, but varying for the experiment depending on the air pocket.

The calculated pressure-impulses showed good agreement for cases AS, ES and AL, though with overestimated values for the uppermost sensor for AS and ES. Case EL showed a bad agreement for the lower regions of the wall, since the double peaked distribution was not captured by the SPH model. The duration of the impacts in the model was in the range 30-40 ms showing little variation, while the experiment had a wide range of 15-110 ms. In the experiment, low pressure peak go hand in hand with a large duration due to the air pockets and the vice versa for extremely high peaks. As a result, very similar pressure-impulses are found between the two wave conditions and the lack of air in the model is less of a determining factor.

The degree of variability was found to be dramatically lowered for the pressure-impulses compared to the peak pressures for both the experiment and the models. This shows that for the design of hydraulic structures, it is more reliable to use the (numerical) impulses instead of the peak pressures. For all above mentioned points of discussion, more validation is needed in terms of experiments and numerical models for varying overhang configurations and wave conditions

The analysis of the velocity fields showed a clear decrease of velocities in a semi-circular profile under the overhang. Thus, the assumption of a constant impact velocity of the pressure-impulse model was not supported. Moreover, a contribution to the impulse was found in both the x- and z-direction, which validated the assumption made in the conceptual model. However, the triangular distribution over the full height of the wall was found to be too conservative and an attempt was made to optimise the model by numerical integration of the velocity fields before impact, resulting in integration boundaries over the wall with a height of $2W$ for the short overhang and $1.5W$ for the longer overhang. Based on the tested conditions, it is concluded that the contribution in z decreases for an increased overhang length.

Chapter 7

Theoretical analysis and validation

This chapter entails the application of the design formulae for a simple vertical wall construction and the validation of the pressure-impulse model and the conceptual model as introduced in chapter 2, theoretical background, for structures with overhang. Furthermore, the velocity fields right before and during impact are analysed for both overhang configurations and compared to the assumptions made in the conceptual model.

7.1 Design formulae structure without overhang

In this section, the design formulae explained in detail in chapter 2, will be applied to the experimental conditions and compared with the numerical model. Figure 7.1 shows the results after using equations 2.8, 2.11 and 2.12 for linear wave theory (LWT), Sainflou and Goda respectively.

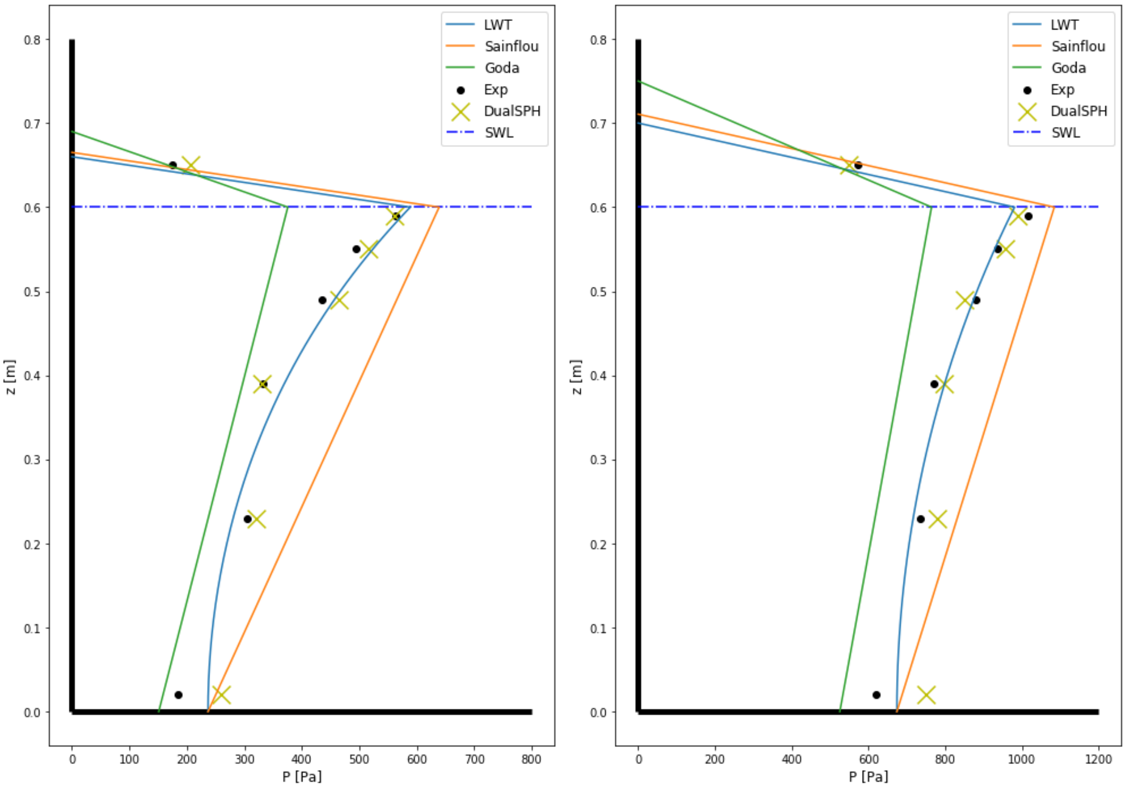

(a) Case A: H = 0.06 m, T =1.3 s (b) Case E: H = 0.1 m, T =1.9 s

Figure 7.1: Validation design formulae for structure without overhang

For the wave and geometrical conditions applied in the experiment, it is clear that LWT shows the best fit for the numerical and experimental pressures. Furthermore, it is observed that Sainflou overestimates the pressures as expected due to its theoretical background. Goda shows an underestimation of the pressures, which is line with van Vledder et al. (2019), in which was found that Goda underestimates for a relative depth d/L smaller than 0.54. For case A and E, the relative depths are 0.25 and 0.15 respectively. Finally, the figure emphasizes the accuracy of the SPH model for standing waves on a vertical wall with sensor 1 near the bottom being an outlier, due to the noise that was recorded. The pressures are integrated over the wall height to obtain the total force on the wall and tabulated in table 7.1. For the experimental and numerical data, the force is calculated by integrating the pressure points using the trapezoidal rule. Note that the rule of thumb given in equation 2.9 as an upper limit is added for thoroughness.

Method	F: Case A [N/m]	Error [%]	F: Case E [N/m]	Error [%]
LWT	224.84	6.13	513.29	5.5
Sainflou	283.46	33.8	587.65	20.8
Goda	164.79	-22.2	426.47	-12.4
Rule of thumb	370.82	75.0	637.65	31.0
SPH	226.85	7.0	508.27	4.4
Exp	211.85	-	486.64	-

Table 7.1: Comparison total horizontal force

It is evident from the table that SPH and LWT both perform very well with small relative errors. Sainflou and Goda become more accurate when the wave height to water depth ratio increases, which is also the case for the rule of thumb. However, the rule of thumb is only a rough estimate for preliminary designs as confirmed by the largest overestimation. SPH has excellent agreement for both conditions. Yet, a higher accuracy is found for the increase in wave height, which has two reasons. Firstly, sensor 7 at the top registered a significant pressure drop in the experiment for the smaller wave height due to temperature changes in the sensor as mentioned in subsection 6.2.1. Secondly, more noise was produced near the bottom due to the particle size to wave height ratio being lower than 10.

7.2 Application models for structures with overhang

In this section, the two theoretical models, i.e. the pressure-impulse model (Wood et al., 2000) and the conceptual model (Tuin, 2019) based on linear wave theory, are applied to the 4 overhang configurations as modelled in LS-Dyna. Firstly, the short overhang conditions are treated and secondly the longer overhang conditions. The solution to the Laplace equation (subsection 2.5.2 and boundary conditions is adopted from de Almeida Sousa and Hofland (2020). The conceptual model is solved in two ways: single integration and double integration. For the single integration method, the highest particle velocities are directly integrated over the height, which is at x =0 for the upward velocity and at $x = -W$ for the horizontal velocities. The integration schemes are given in equations 7.1 and 7.2 using the axes as schematised in figure 2.21 as reference. Note that the representative width is equal to the overhang width. Equations 2.5 and 2.6 are implemented for the particle velocities assuming full reflection, i.e. $a = H$. The newly found boundaries of integration in 6.5.2 for the conceptual model are added with the label 'Conceptual model: Modified', and presented in 7.3. The lower boundary for z is denoted as 'a' and equal to $2/3d$ for the short overhang and $3/4d$ for the longer overhang. The distribution of $W(z)$ is adjusted accordingly.

$$\text{Single Integration} = \begin{cases} I_x = \rho W \int_0^d u_{x,refl}(-W, z)dz \\ I_z = \rho W \int_0^d u_{z,refl}(-0, z)dz \end{cases} \tag{7.1}$$

$$\text{Double integration} = \begin{cases} I_x = \rho \int_0^d \int_{-W}^0 u_{x,refl}(x, z)dxdz \\ I_z = \rho \int_0^d \int_{-W(z)}^0 u_{z,refl}(x, z)dxdz \end{cases} \tag{7.2}$$

$$\text{Modified integration} = \begin{cases} I_x = \rho \int_0^d \int_{-\frac{3}{2}W}^0 u_{x,refl}(x, z)dxdz \\ I_z = \rho \int_a^d \int_{-W(z)}^0 u_{z,refl}(x, z)dxdz \end{cases} \tag{7.3}$$

$$\text{In which:} \quad W(z) \quad = \quad \begin{cases} \dfrac{W}{d}z \\ \dfrac{1}{2}z + \left(W - \dfrac{1}{2}d\right) & \text{(Modified: Short overhang)} \\ \dfrac{4}{3}z + \left(W - \dfrac{4}{3}d\right) & \text{(Modified: Longer overhang)} \end{cases}$$

All pressure-impulse profiles and integrated force-impulses are made dimensionless (denoted with an overbar) using the definitions given in equations 7.4 and 7.5 as introduced in section 2.5.2 with V being the vertical impact velocity. This velocity is found using equation 2.6 and is equal to 0.29 m/s and 0.33 m/s for cases A and E respectively.

$$\overline{P} = \frac{P}{\rho V W} \tag{7.4}$$

$$\overline{I} = \frac{I}{\rho V W^2} \tag{7.5}$$

7.2.1 Short overhang configuration

The results for the conditions $H = 0.06$ m and 0.1 m with $T = 1.3$ s and 1.9 s for $W = 0.1$ m, i.e. cases AS and ES, are given in this subsection for the dimensionless numerical and experimental pressure-impulse profiles and are compared to the theoretical models. Figure 7.2 shows the results for the dimensionless profiles along the wall.

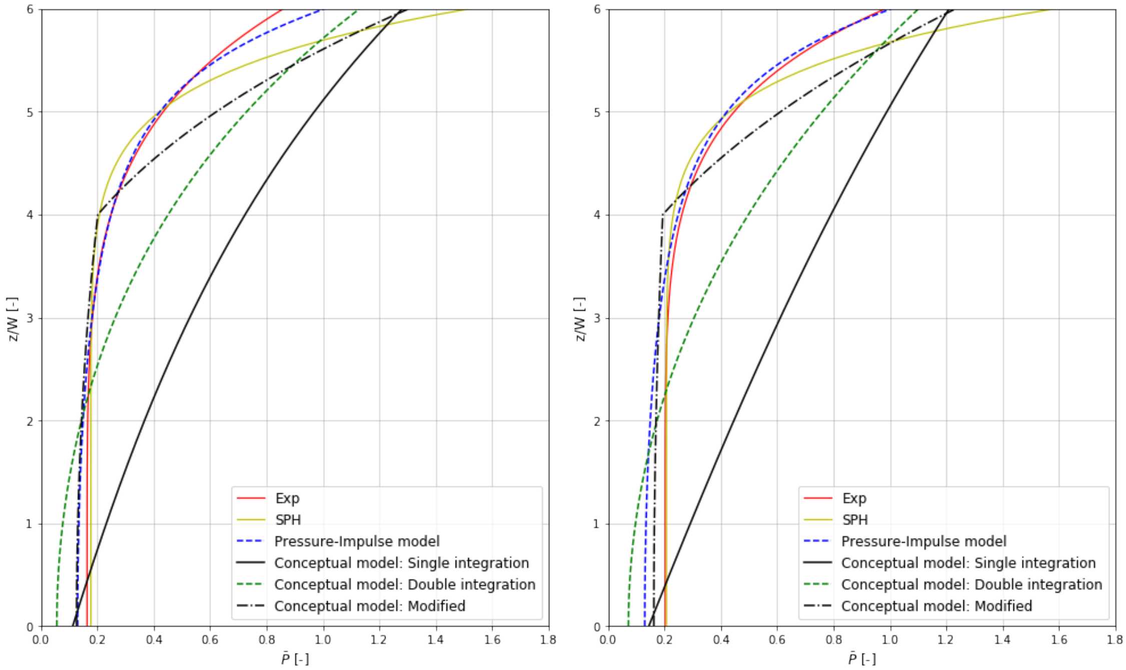

(a) Case AS: $H = 0.06$ m, T =1.3 s (b) Case ES: $H = 0.1$ m, T =1.9 s

Figure 7.2: Dimensionless pressure-impulse profiles along the wall for short overhang conditions

Evidently, the pressure-impulse model has the best fit for the short overhang configuration for both conditions. It can be observed that in either case there is only a mild underestimation near the bottom of the wall, which is amplified for case E. Halfway, the pressure-impulse model converges to the experimental profile. The conceptual model does not show the highly linear distribution up to $z/W = 3$ for either solution originally. The single integration scheme shows bad agreement with the numerical and experimental profiles. For the double integration method, the profile becomes less linear and shows a better representation of the profile. Right under the overhang at $z/W = 6$, the conceptual model converges to the experiment and shows higher accuracy than the SPH models. The modified model does show a good fit up to $z/W = 3$. The kink in the line is caused by the contribution of the z-velocities. By integration of the profile over the wall, the total dimensionless force-impulse can be calculated to quantify the level of agreement with the experiment. Then, equation 7.5 is applied to make the force-impulse dimensional. These values are found in table 7.2. Note that the fitted solution proposed by Hofland et al. (2019), as given by equation 2.25, is added to the table to be complete.

Model	I: Case AS [Ns/m]	Error [%]	I: Case ES [Ns/m]	Error [%]
Pressure-impulse	4.71	-2.2	5.37	-12.5
Concept: Single	10.14	110.9	12.57	144.0
Concept: Double	6.44	33.9	7.90	28.9
Concept: Modified	5.62	16.6	6.56	7.0
Fitted solution	4.84	0.6	5.52	-10.0
SPH	5.34	11.1	6.60	7.7
Exp	4.81	-	6.13	-

Table 7.2: Comparison force-impulse on wall for short overhang conditions

The table shows only a very mild error for the pressure-impulse model for case A and a slightly increased, yet small error for case E. The fitted solution to the pressure-impulse model shows very similar outcomes, which is expected taking the validity range of the overhang widths into account for which the formula was derived, which this configuration suffices. Logically, the conceptual model shows large variation whether single or double integration is applied. The single integration method returned more than twice the experimental values, which means that this method largely overestimates when the spatial coordinate in x direction is taken as a constant. The conceptual model becomes far more accurate when double integration, though still shows errors around 30%, since the highly linear part of the profile, between $z/W = 0$ and $z/W = 4$, is not reproduced. The modified model with the adjusted area of integration for the z-velocity shows largely increased accuracy, especially for case ES. Finally, SPH shows excellent agreement with only a mild overestimation of the force-impulse, which is due to the profile diverging from the experiment closely under the overhang.

The force-impulse on the overhang is calculated using the same technique and compared to the pressure-impulse model, for which the infinite depth solution is used as given in equation 2.24. The choice for this convenient solution is based on the ratio of the height over the overhang width equal to $d/W = 6$, which is closely approximated by the ratio $d/W = \infty$ as supported by figure 2.19. The dimensionless profiles are depicted in figure 7.3 and the integrated force-impulses are tabulated in table 7.3.

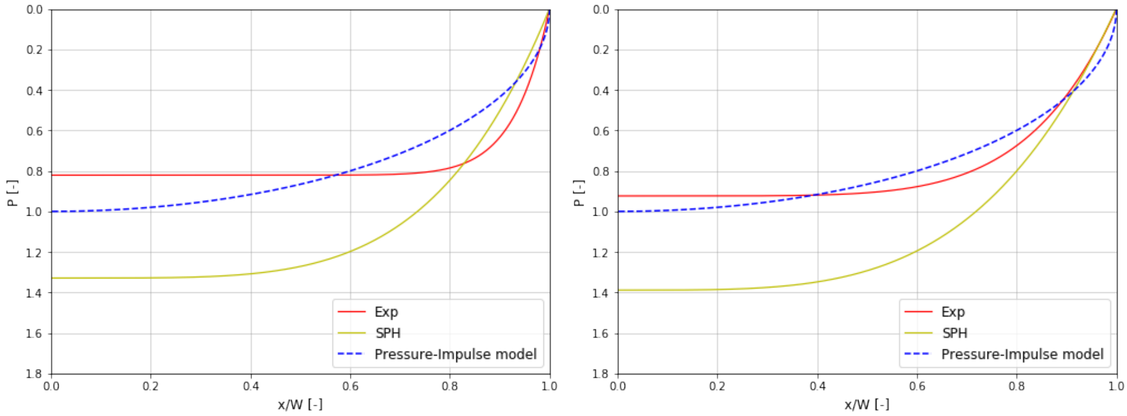

(a) Case AS: H = 0.06 m, T =1.3 s (b) Case ES: H = 0.1 m, T =1.9 s

Figure 7.3: Dimensionless pressure-impulse profiles along the overhang for short overhang conditions

The pressure-impulse model shows excellent agreement with the experimental force-impulses, while the SPH model overestimates by a margin of about 40%. Naturally, the varying

Model	I: Case AS [Ns/m]	Error [%]	I: Case ES [Ns/m]	Error [%]
Pressure-impulse	2.28	-2.5	2.60	-0.51
SPH	3.16	42.1	3.64	39.6
Exp	2.22	-	2.61	-

Table 7.3: Comparison force-impulse on overhang for short overhang conditions

shape of the profile cannot be reproduced by the theoretical model as it assumes a semi-circular shape only dependent on the overhang width, while in reality the shape is also influenced by other factors, such as the effect of air pockets and the points where the wave hits the structure, which led to the flattened experimental profile for case A. Nevertheless, excellent results are found for the application of the theoretical model.

7.2.2 Longer overhang configuration

Next, the two wave conditions for the longer overhang are analysed and compared with theory. The results for the conditions H = 0.06 m and 0.1 m with T = 1.3 s and 1.9 s for W = 0.2 m, i.e. cases AL and EL, are given for the dimensionless numerical and experimental pressure-impulse profiles along the wall in figure 7.4.

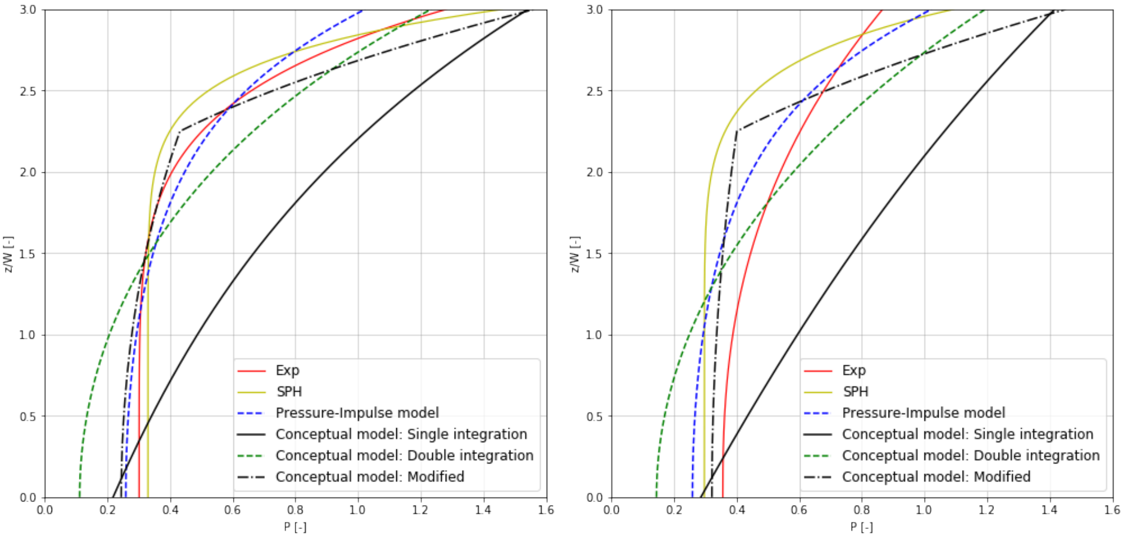

(a) Case AL: H = 0.06 m, T =1.3 s

(b) Case EL: H = 0.1 m, T =1.9 s

Figure 7.4: Dimensionless pressure-impulse profiles along the wall for longer overhang conditions

Starting with figure 7.4a, which shows the milder wave conditions, it can be observed that the pressure-impulse model shows good agreement with the experiment up to z/W = 2.5, after which the profile underestimates the experimental pressure-impulse. For the conceptual model, the same behaviour is observed as for the short overhang conditions. The single integration scheme shows a large overestimation over the entire height and a profile that's too linear compared to the experiment and numerical model. The double integral method underestimates the values in the lower regions of the wall more strongly than for a short overhang, but approaches the experiment near the top accurately. The modified model shows a good fit with the experiment, but overestimates at the top where it converges to the single integration line. Figure 7.4b shows again that this wave condition is a special case, due to its double wave impact. Compared to the previous cases, the strongest deviation is observed between the theoretical models and the experiment. The pressure-impulse model shows the best agreement. Table 7.4 presents the integrated dimensional force-impulses for the displayed profiles.

Model	I: Case AL [Ns/m]	Error [%]	I: Case EL [Ns/m]	Error [%]
Pressure-impulse	15.05	-4.3	17.17	-13.6
Concept: Single	25.64	62.9	31.57	58.8
Concept: Double	15.45	-1.8	18.98	-4.93
Concept: Modified	16.09	2.3	19.04	2.1
Fitted solution	15.07	-4.2	17.19	-13.5
SPH	15.16	-3.7	15.07	-24.2
Exp	15.73	-	19.88	-

Table 7.4: Comparison force-impulse on wall for longer overhang conditions

SPH and the conceptual model show the highest accuracy in determining the force-impulses for case AL. For the conceptual model, the force-impulse for the single integration scheme is still far too high. The modified model and double integration scheme show excellent agreement, not only for case AL, but also for EL, for which they outperform the rest. Also, it can be observed that the modified model converges to the original model for the increased wave height. However, the pressure impulse-model still does well with an error of -13.6% and showed the best fit to the profile. Based on table 7.2 and 7.4 it can be concluded that the pressure-impulse model, when applied to the vertical wall, is accurate for both overhang configurations, with the best performance for very short overhang widths. This can be explained by the assumption in the theory that the impact velocity is equal for the entire width, which is a fair assumption for very short overhangs. The original conceptual model is best applied for longer overhang configurations, as its accuracy improved significantly for the increased overhang width. However, the double integration scheme is superior and should be applied to achieve the most accurate force-impulses. When the conceptual model is modified by adjusting the boundaries, a better fit of the profile is found. Furthermore, the accuracy in determining the force-impulse is greatly increased for the short overhang. For the longer overhangs, similar result is obtained. That said, all models have difficulties in reproducing the double impact pressure-impulse for case EL. SPH showed excellent potential in calculating the force-impulses on the wall.

Finally, the dimensionless pressure-impulse profile on the longer overhang is plotted and displayed in figure 7.5. The force-impulses are calculated by integration of the profiles and given in table 7.5.

Model	I: Case AL [Ns/m]	Error [%]	I: Case EL [Ns/m]	Error [%]
Pressure-impulse	9.11	-19.3	10.39	-0.6
SPH	12.09	7.2	10.96	4.9
Exp	11.3	-	10.44	-

Table 7.5: Comparison force-impulse on overhang for longer overhang conditions

Clearly, the numerical models show consistent agreement for either wave condition and precisely produce the experimental force-impulses. The increase in accuracy for the longer overhang configuration is in line with earlier findings in chapter 6. The pressure-impulse model shows its strongest deviation for case AL, with an underestimation of the force-impulse of around 20% in contrast with case EL, where the exact experimental value is found.

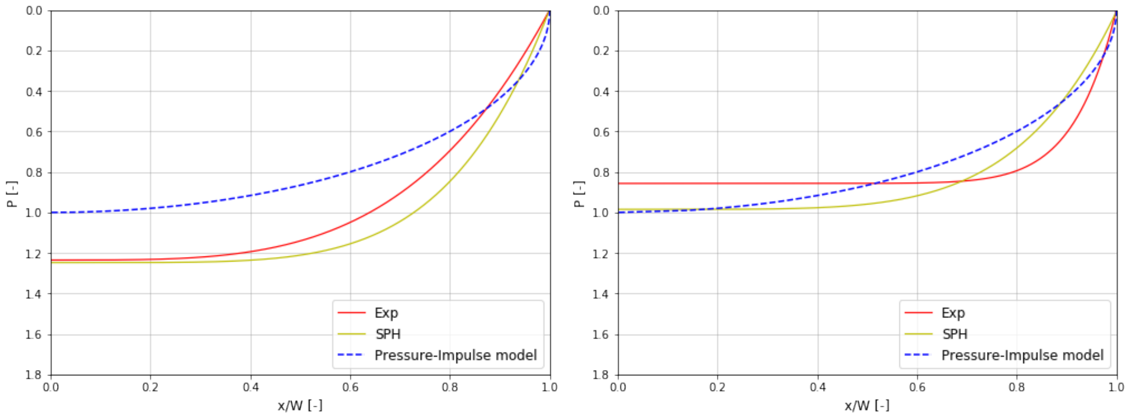

(a) Case AL: H = 0.06 m, T =1.3 s

(b) Case EL: H = 0.1 m, T =1.9 s

Figure 7.5: Dimensionless pressure-impulse profile along the overhang for longer overhang conditions

Overall, it can be concluded that SPH can be used in the estimation of force-impulses on the wall for the overhang configurations. For the force-impulse on the overhang, there is a clear increase in performance for the longer overhang conditions. Naturally, there is a direct relation between how accurate the uppermost numerical sensor on the wall in the impact zone can register the pressure-impulse and the deviation in pressure-impulse profiles along the overhang. Of the theoretical models, the most consistent performance is found for the pressure-impulse model. Only for case AL, which is strongly influenced by the entrapment of air, a relatively large deviation was found. The conceptual model showed accurate results for the longer overhang conditions in which it outperformed the pressure-impulse model for case EL. Therefore, it is interesting to analyse even longer overhang configurations in future study, and conditions in which the overhang width exceeds a quarter of the wave length, which is set as a boundary condition in the theory. The modified conceptual model showed better agreement than the original model for the short overhang conditions, when the contribution of the z-velocity was reduced. Moreover, the base pressure-impulse was more accurate when the contribution of the impact in x-direction was increased.

Chapter 8

Discussion, conclusions and recommendations

This chapter concludes the study and presents the final remarks of the research. A discussion is provided about the used model setup and its limitations, the interpretation of the results, both numerically and theoretically and the applicability. Thereafter, the conclusions are formulated as answers to the research questions. Finally, recommendations are given for further research of numerical modelling of wave impact on structures with an overhang.

8.1 Discussion

Model setup
In this thesis, two different software packages have been applied, namely DualSPHysics and LS-Dyna, which came with their limitations. For the former, the boundary condition did not allow for application to the overhang configurations, as a boundary gap formed between the rigid members and the particles. However, in terms of wave generation, the software provided an AWAS, which resulted in much smaller models as no re-reflective waves occurred. Ideally, the software packages would interchange their wave generation and boundary conditions to provide the optimum numerical tool. As a result, CPU time and the size of result files would decrease dramatically, which allows for smaller particle sizes to be implemented.

The applied numerical models have a number of simplifications that influence the results. Firstly, the model is 2D, which is not able to capture 3D effects. As a result, the pressures are usually found to be higher than when a 3D model is applied. However, SPH is a computationally challenging method and sensitive to storage capacity, and so a 3D model would result in a greatly increased CPU time and size of the result files. Similarly, an optimum had to be found in particle size, which was chosen to be $dp = 10$ mm. However, the smaller the particle size, the better representation of reality is achieved. Secondly, rigid boundaries were used to construct the wall and overhang, while in reality, some degree of elasticity is present. This results in dynamic effects as vibrations occur (Tieleman et al., 2019), which leads to a structural response. Therefore, SPH is not used at its full potential in this research, even if the studied impact falls into the impulsive category.

Interpretation of results
The results of the wave gauges were obtained by application of a piston type wave maker. The excitation of the wave maker was calculated from theory and applied in the model. However, obtaining the correct wave height was an iterative process as some diffusion was

observed in the numerical flume due to its long length. As such, it is advisable to use shorter domain lengths in practice, which is possible once an AWAS is developed.

The noisy pressure distribution for the structure without overhang was partly caused by the instantaneously applied gravity force at $t = 0$. It would be an improvement if a ramp function can be introduced that will result in a more gentle application, causing less shake-up of the particle domain. Furthermore, the pressure peaks and pressure-impulses were obtained for 5 to 6 wave impacts, depending on the wave celerity. However, in the experiment 70 peaks were obtained due to its much longer simulation time. When an AWAS is applied and the numerical domain shortened, more stable peaks can be obtained to possibly reduce the standard deviation and variation. Furthermore, no air was included in the model. This means aeration effects, such as cushioning by air pockets, were not reproduced and the impact duration showed much less variation than the experiment. Moreover, a single consistent manner of impact on the overhang was observed at the transition from wall to overhang, while the experiment showed multiple variations. The most apparent variation was the double impact type. For this case, SPH did not show good agreement in terms of impulses.

The numerical velocity fields were calculated by subtracting the velocity just after impact from the impact velocity. This is an accurate method for the top sensors that showed clear abrupt drops in velocities, but introduced some noise for the deeper located velocities, mostly in x-direction. The proposed modifications of the conceptual model based on the velocity fields, are exploratory and more validation is needed to derive a true relation between areas of integration, relative to the width of the overhang and the wave conditions.

Scope of research
All overhang configurations used in this thesis sufficed the criteria for short overhangs (de Almeida Sousa et al., 2019). Furthermore, the applied wave conditions were chosen, such that the validity criteria of the pressure-impulse model were met (de Almeida Sousa & Hofland, 2020). Only one water level condition was applied, that is with a freeboard of zero. In this thesis, the pressure-impulse model is considered without air. However, the theory can be expanded by including the effects of air with a so called 'bounce back' factor, describing the sudden expansion of an air bubble (de Almeida Sousa & Hofland, 2020; Wood et al., 2000).

Applicability
In practice, physical experiments are time consuming, expensive and thus not always available. Based on this study, the numerical SPH tool showed to be applicable to wave impact problems on overhangs. However, for design purposes an analytical solution is useful due to its quick application. For longer overhang configurations than the validity range of the pressure-impulse model, it is advised to use the conceptual model in its original form, as it was found that the accuracy increased for the longer overhang case. Besides, the optimisation of the areas of integration is only in its initial phase as not enough experimental/numerical validation is provided yet.

8.2 Conclusions

The conclusions of this research are found by combining the findings in this report with the main objectives, which were testing the capabilities of the SPH and using the numerical and experimental results to validate the theoretical models. The conclusion is formulated by the hand of the 3 research questions.

Can SPH accurately predict non-impulsive and impulsive wave loads of non-breaking waves?

This research question consists of two parts and will be answered accordingly, starting with the non-impulsive wave loads on vertical walls.

The structure without overhang was modelled in DualSPHysics, and showed excellent agreement with the experiment. The measured water surface elevation approached a 1 to 1 correlation and overlap for the majority of the wave gauges. The experimental pressures were found to be accurately reproduced by the model. The total integrated force on the wall had only a very mild deviation of 7% and 4.4% for the low and higher wave heights respectively, by which it outperformed the design formulae. Thus, it can be concluded that SPH can accurately predict non-impulsive wave loads on vertical walls for the tested conditions in this thesis.

The structures with overhang were modelled in LS-Dyna. Spurious agreement of the wave fields was found for the smallest wave heights. The wave pattern after reflection was only moderately reproduced by the model and the lack of an AWAS limited the number of undisturbed waves. A strong increase in accuracy was found for the higher wave height as a ratio H/dp of 10 was sufficed. In all cases, the pressure distributions repeatedly showed an overestimation for the two uppermost sensors, located in the impact zone, in the range of 15-30%. The error was more significant the more the experimental case was influenced by air, as no air particles were included in the model. The longer overhang with the largest wave height condition showed the least agreement, as here the wave was observed to impact in two stages in the experiment. However, SPH showed good agreement with the experimental pressure distributions overall.

Can SPH be used to calculate the force-impulse on a structure with overhang?

The SPH pressure-impulse profiles along the wall showed good agreement with the experiment, except for the double impact case. Here, the pressure-impulse was split up in two contributions while SPH only showed one, which led to a strong underestimation for the lower regions on the wall. For the short overhang configurations, excellent agreement was found for the lower 4 sensors, while the upper two sensors showed an overestimation in the range of 50%, which is explained by the duration of the impact. SPH showed a more or less constant impact duration of 30-40 ms, while a large variety was found for the experiment (15-110 ms) due to air effects. That said, the lack of air effects in the model was mitigated by the use of pressure-impulse. Namely, when a large air pocket was observed in the experiment, it resulted in a relatively low peak, but large impact duration, while the SPH model showed higher pressures, but with a lower impact duration. Thus, the numerical pressure-impulse profile ’corrects’ itself, when the impact duration and pressure peaks are integrated. Furthermore, a strong reduction in variability was found (3-5 times less) when using pressure-impulses instead of peak pressures. Integration of the profiles showed a high level of agreement of the force-impulses, except on the short overhang, due to its overestimation of the pressures combined with a similar impact duration as the experiment.

How do the results of the theoretical models for a structure with overhang compare to SPH?

In this thesis, two theoretical models were presented, namely the pressure-impulse model (Wood & Peregrine, 1996) and the conceptual model (Tuin, 2019). An analysis of the numerical velocity fields showed circular contours of the stopped water mass, similar to the pressure-impulse model, but did not present a constant velocity. A decrease was observed from the point of impact outwards both over the width and depth, which was amplified for the longer overhang. Furthermore, a contribution in x-direction was found in agreement with the conceptual model. However, the width of the stopped mass in x-direction extended past the overhang to approximately $1.5W$. Also, the triangular area of integration for the z-velocity was found to be too conservative when integrated over the full wall height. Instead, the contribution has to be lowered, which is more apparent for the longer overhang case. Therefore, SPH was used to propose a modified conceptual model with the new integration width for x to $1.5W$, and height of the triangular area for z of $2W$ for the short overhang and $z = 3/4W$ for the longer overhang.

In a theoretical analysis, the conceptual model was solved by using single, double and modified integration schemes. The single scheme showed a large overestimation of force-impulse and thus could be disregarded. The double scheme showed errors in force-impulse of 30% for the short overhang case, but increased in accuracy dramatically for the longer overhang case up to 5%. The modified model showed excellent agreement in force-impulse and resulted in a better fit to the numerical and experimental pressure-impulse profile than the original model. The pressure-impulse model showed good agreement in the shape of the profile and magnitude of force-impulse for both the wall and overhang. A stronger agreement was found for the short configuration, as here the vertical impact velocity is more constant.

Finally, it was found with the use of SPH that the base pressure-impulse along the wall is caused by the impact in x-direction and the increase near the waterline by the contribution of the impact in z-direction.

8.3 Recommendations

Recommendations for further research are given based on the discussion and conclusions of this thesis.

- SPH showed good results in simulating non-breaking wave impact on structures with overhang. However, more extensive validation is needed for a greater variety of configurations, incident wave conditions and freeboards

- The structure of interest was a steel gate. In this report, the behaviour above the waterline was researched due to wave impact. However, it would be interesting to know what happens under the water line to the submerged members of the gate, loaded by wave induced pressures, e.g. in the form of a case study

- The theoretical and numerical models were applied disregarding air. It is recommended to apply SPH models including air particles to analyse if the observed aeration effects can be simulated, like cushioning of peak pressures and variations in impact duration. Due care has to be given to linking the SPH parts and their discrepancies in properties, like the compressibility of air compared to water. Analytical validation can be done by using the pressure-impulse model including bounceback factor (de Almeida Sousa & Hofland, 2020)

- Propositions to modify the conceptual model were given based on the 4 conditions in this thesis. More extensive validation is needed for a complete optimisation of the areas of integration and their shapes. Furthermore, it is advisable to compare the capabilities of the theoretical models when applied to overhang ranges longer than $W/L_0 < 0.1$ or $3 < d/W < 6$ and/or for freeboards not equal to zero

- For this thesis, SPH was used to calculate and compare pressure-impulse and force-impulse. It is advisable to perform similar research with different CFD tools to analyse their strengths and limitations compared to SPH. In doing so, SPH can be further analysed by using local refinement of particles, i.e. using a higher resolution for the wave impact zone to increase accuracy while simultaneously lowering run times, by testing 3D models and their comparison to 2D and by using different formulations of the kernel approximation
- The dynamics of the overhang construction is only briefly touched upon in this thesis. However, dynamics are an important factor in the design of hydraulic structures, and so an in depth dynamic analysis is recommended to explore the full potential of SPH
- The impact duration can be used to translate impulses to forces. However, this value is highly dependent on the level of air entrapment and difficult to standardise. Further research is needed for design implementation to make sure that the designs are not too conservative when the impact duration is considered too short and vice versa.

Bibliography

Airy, G. B. (1845). *Tides and waves*. Encyclopaedia Metropolitana.

Altomare, C., Crespo, A., Domínguez, J., Gómez-Gesteira, M., Suzuki, T., & Verwaest, T. (2015). Applicability of smoothed particle hydrodynamics for estimation of sea wave impact on coastal structures. *Coastal Engineering*, *96*, 1–12. https://doi.org/10.1016/j.coastaleng.2014.11.001

Altomare, C., Dominguez, J. M., Crespo, A. J. C., Gonzalez-Cao, J., Suzuki, T., Gomez-gesteira, M., & Troch, P. (2017). Long-crested wave generation and absorption for SPH-based DualSPHysics model. *Coastal Engineering*, *127*, 37–54.

Bagnold, R. A. (1939). Interim report on wave-pressure research. *Jour. of Institute of Civil Engineers*, *12*.

Battjes, J. A. (1974). Computation of set-up, longshore currents, run-up and overtopping due to wind-generated waves. Civil Engineering; Geosciences.

Bistafa, S. R. (2018). On the development of the navier-stokes equation by navier. *Revista Brasileira de Ensino de Fisica*, *40*. https://doi.org/http://dx.doi.org/10.1590/1806-9126-RBEF-2017-0239

Bullock, G. N., Obhrai, C., Peregrine, D. H., & Bredmose, H. (2007). Violent breaking wave impacts. part 1: Results from large-scale regular wave tests on vertical and sloping walls. *Coastal Engineering, Elsevier*, (54).

Burcharth, H. (2003). *Breakwaters with vertical and inclined concrete walls* [Report of Working Group 28 of the Maritime Navigation Commission]. PIANC General Secretariat, Brussels.

CERC. (1984). *Shore protection manual* [4th Edition]. U.S. Govt. Printing Office, Washington DC.

Chen, X., Hofland, B., Capel, A., & van Gent, M. R. A. (2019). Use of impulses to determine the reaction force of a hydraulic structure with an overhang due to wave impact. *Coastal Engineering, Elsevier*, *147*, 75–88.

Cooker, M., & Peregrine, D. (1990). Violent water motion at breaking-wave impact. *Proceedings of the International Conference on Coastal Engineering*, *1*(22).

Cooker, M., & Peregrine, D. H. (1995). Pressure-impulse theory for liquid impact problems. *Fluid Mechanics*, (297).

Crespo, A., Domínguez, J., Rogers, B., Gómez-Gesteira, M., Longshaw, S., Canelas, R., Vacondio, R., Barreiro, A., & García-Feal, O. (2015). Dualsphysics: Open-source parallel cfd solver based on smoothed particle hydrodynamics (sph). *Computer Physics Communications*, *187*, 204–216. https://doi.org/https://doi.org/10.1016/j.cpc.2014.10.004

Cummins, S., Silvester, T., & Cleary, P. (2012). Three-dimensional wave impact on a rigid structure using smoothed particle hydrodynamics. *International Journal for Numerical Methods in Fluids*, *68*, 1471–1496. https://doi.org/10.1002/fld.2539

Cuomo, G., & Allsop, W. (2005). Wave impact at sea walls. https://doi.org/10.1142/9789812701916_0327

Cuomo, G., Allsop, W., Bruce, T., & Pearson, J. (2010). Breaking wave loads at vertical seawalls and breakwaters. *Coastal Engineering*, *4*(57).

Dao, M. H., Xu, H., Chan, E. S., & Tkalich, P. (2013). Modelling of tsunami-like wave run-up, breaking and impact on a vertical wall by SPH method. *Nat. Hazards Earth Syst. Sci.*, *13*, 3457–3467.

de Almeida Sousa, E., & Hofland, B. (2020). Validation of pressure-impulse theory for standing wave impact loading on vertical hydraulic structures with short overhangs. *Coastal Engineering*, *159*. https://doi.org/https://doi.org/10.1016/j.coastaleng.2020.103702

de Almeida Sousa, E., Hofland, B., & Jonkman, S. N. (2019). Wave Impact Pressure-Impulse on Vertical Structures with Overhangs. *N. Gosenberg, T. Schlurmann (Eds.), Coastal Structures 2019 Bundesanstalt für Wasserbau.* https://doi.org/https://doi.org/10.18451/978-3-939230-64-9_010

de Koning, J. (2019). *Simulating bending failure of ice using smoothed particle hydrodynamics* (Master's thesis). Delft University of Technology. the Netherlands.

Didier, E., Neves, D. R. C. B., Martins, R., & Neves, M. G. (2014). Wave interaction with a vertical wall: SPH numerical and experimental modeling. *Ocean Engineering*, *88*, 330–341.

Filho, C. A. D. F., & Chacaltana, J. T. A. (2017). Boundary treatment techniques in smoothed particle hydrodynamics: Implementations in fluid and thermal sciences and results analysis.

Galvin, C. J. J. (1964). Wave-Height prediction for wave generators in shallow water. *Tech. Memo. 4*.

Gingold, R. A., & Monaghan, J. J. (1977). Smoothed particle hydrodynamics: theory and application to non-spherical stars., *181*, 375–389. https://doi.org/10.1093/mnras/181.3.375

Goda, Y. (1972). *A new method for wave pressure calculation for the design of composite breakwaters.* Proceeding of 14th international Conference Coastal Engineering.

Gómez-Gesteira, M., & Dalrymple, R. (2004). Using a three-dimensional smoothed particle hydrodynamics method for wave impact on a tall structure. *Journal of Waterway Port Coastal and Ocean Engineering-asce*, *130*. https://doi.org/10.1061/(ASCE)0733-950X(2004)130:2(63)

Gui, Q., Shao, S., & Dong, P. (2014). Wave impact simulations by an improved ISPH model. *Journal of Waterway, Port, Coastal, and Ocean Engineering*, *140*, 04014005. https://doi.org/10.1061/(ASCE)WW.43-5460.0000239

Hallquist, J. O. (2006). Ls-dyna theory manual. Livermore Software Technology Corporation.

Hofland, B., Kaminski, M. L., & Wolters, G. (2010). Large scale wave impacts on a vertical wall. *Coastal Engineering*.

Hofland, B., Massos, M., & de Almeida, E. (2019). Effect of Venting Holes to Relieve Wave Impact Pressures on Flood Gates with Overhangs. *N. Gosenberg, T. Schlurmann (Eds.), Coastal Structures 2019 Bundesanstalt für Wasserbau*, 190–199. https://doi.org/https://doi.org/10.18451/978-3-939230-64-9_020

Holthuijsen, L. H. (2007). *Waves in oceanic and coastal waters*. Cambridge University Press, New York.

Jongeling, T. H. G., & Erdbrink, C. (2010). *Dynamica van beweegbare waterkeringen* [Trillingen in onderstroomde schuiven en uitgangspunten voor een schaalmodelopstelling]. Deltares, Delft.

Karman, v. (1929). The impact on sea plane floats during landing. *Nat. Adv. Comm. Aeronautics*, *Technical note*(321).

Kisacik, D., Bogaert, P., Troch, P., & Caspeele, R. (2014). Investigation of uplift forces on a vertical wall with an overhanging horizontal cantilever slab. *Coastal Engineering*, (90).

Kolkman, P. A., & Jongeling, T. H. G. (2007). *Dynamic behaviour of hydraulic structures* [Part B: Structures in waves]. Delft hydraulics, Delft.

Korthof, R. M. (1982a). *Stormvloedkering oosterschelde: Orienterend onderzoek naar golfklappen op de plaatliggerschuif: Loodrechte golfaanval en aanstroming* (tech. rep. No. M1504). Rijkswaterstaat.

Korthof, R. M. (1982b). *Stormvloedkering oosterschelde: Vertikale golfbelastingen op de vakwerkschuiven: Loodrechte aanval* (tech. rep. No. M1723). Rijkswaterstaat.

Liu, M. B., & Liu, G. R. (2010). Smoothed particle hydrodynamics (SPH): An overview and recent developments. *Archives of Computational Methods in Engineering*, *17*, 25–76.

Lundgren, H. (1969). *Wave shock forces: An analysis of deformations and forces in the wave and in the foundation*. Proc: Symposium: Research on wave action, Vol 2, Delft.

Mai, T., Mai, C., Raby, A., & Greaves, D. m. (2019). Aeration effects on water-structure impacts: Part 2. wave impacts on a truncated vertical wall. *Ocean Engineering, Elsevier*, (186).

Miche, R. (1944). Mouvements ondulatoires des mers en profondeur constante on decroissante. *Annales des Ponts et Chaussées*.

Minikin, R. R. (1963). *Winds, waves and maritime structures* [2nd Edition]. Griffin, London.

Molenaar, W. F., & Voorendt, M. Z. (2016). *Manual hydraulic structures*. Delft University of Technology, Delft.

Monaghan, J. J. (1977). Simulating free surface flows with SPH. *Journal of Computational Physics*, *110*, 399–406.

Morison, J. R. (1950). The force exerted by surface waves on piles. *Journal of Petroleum Engineering*, *2*. https://doi.org/https://doi.org/10.2118/950149-G

Niu, K.-N., Zheng, X., Miao, Y., & Lv, X.-P. (2015). Numerical simulation of violent wave impact by ISPH method. *Procedia Engineering*, *126*, 665–669. https://doi.org/10.1016/j.proeng.2015.11.258

Oumeraci, H., Kortenhaus, A., Allsop, W., de Groot, M., Crouch, R., Vrijling, J., & Voortman, H. (2001). Probabilistic design tools for vertical breakwaters. In H. Voortman (Ed.), *Probabilistic design tools for vertical breakwaters* (pp. 1–373). CRC Press / Balkema - Taylor Francis Group.

Rafiee, A., Dutykh, D., & Dias, F. (2013). Numerical simulation of wave impact on a rigid wall using a two–phase compressible sph method. https://doi.org/10.1016/j.piutam.2015.11.013

Rijkswaterstaat. (2019). *Oosterscheldekering*. Retrieved November 19, 2019, from https://www.rijkswaterstaat.nl/water/waterbeheer/bescherming-tegen-het-water/waterkeringen/deltawerken/oosterscheldekering/

Sainflou, G. (1928). Essai sur les digues maritimes. *Annales des Ponts et Chaussées*, *98*(4).

Schiereck, G. J., & Verhagen, H. J. (2012). *Introduction into bed, bank and shoreline protection* [2nd edition]. VSSD.

Shah, S. A. (2010). *Water impact investigations for aircraft ditching analysis* (Master's thesis). RMIT University. Vietnam.

Silvester, T., & Cleary, P. (2006). Wave-structure interaction using smoothed particle hydrodynamics.

Stokes, G. G. (1847). *On the theory of oscillatory waves*. Reports of the British Association, Volume VI.

Takahashi, S., & Hosoyamada, S. (1993). Hydrodynamic characteristics of sloping top cassions. *Proceedings of the International Conference on Hydro-technical Engineering*, *5*(31).

Tanimoto, K., Goda, Y., Moto, K., & Isizuka, S. (1976). *An investigation on design wave force formulae of composite-type breakwaters*. Proceeding of 23rd Japanese Conference Coastal Engineering.

TAW. (2003). *Leidraad kunstwerken*. Nivo, Delft.

Tieleman, O. C., Tsouvalas, A., Hofland, B., Y., P., & Jonkman, S. N. (2019). A three dimensional semi-analytical model for the prediction of gate vibrations immersed in fluid. *Marine Structures*, *65*, 134–153. https://doi.org/https://doi.org/10.1016/j.marstruc.2018.12.007

Tuin, H. G. (2019). Conceptual wave impact model on a structure with overhang based on linear wave theory - discussion notes.

Tung, T. T. (2018). Study of the SPH method in LS-DYNA. *International Journal of Science and Research*, *7*(8).

van Vledder, G., Hofland, B., Tuin, H., & van Maris, B. (2019). Numerical Evaluation of Design Rules for Non-Breaking Wave Loads on Vertical Walls. *N. Gosenberg, T. Schlurmann (Eds.), Coastal Structures 2019 Bundesanstalt für Wasserbau.* https://doi.org/https://doi.org/10.18451/978-3-939230-64-9_076

Varnousfaaderani, M. R., & Ketabdari, M. J. (2015). Numerical simulation of plunging wave breaker impact by a modified turbulent WCSPH method. *Journal Brazilian Society of Mechnical Sciences and Engineering*, *37*, 507–523.

Visser, T. (2003). *Ontwerpnota stromvloedkering oosterschelde: Boek 4:de sluitingsmiddelen* (tech. rep.). Rijkswaterstaat.

Wagner, H. (1932). Über stoss- und gleitvorgänge an der oberfläche von flüssigkeiten. *Zeitschrift für Angewandte Mathematik und Mechanik*, *12*(4).

Waternoodsmuseum. (2018). *Oosterscheldekering.* Retrieved November 19, 2019, from https://watersnoodmuseum.nl/kennisbank/oosterscheldekering/

Wood, D. J., & Peregrine, D. H. (1996). Wave Impact beneath a horizontal surface. *In: Proceedings of Coastal Engineering Conference*, 2573–2583.

Wood, D. J., Peregrine, D. H., & Bruce, T. (2000). Wave Impact on a Wall using Pressure-Impulse Theory. I: Trapped Air. *J. Waterway, Port, Coastal and Ocean Eng.*, *126*, 182–190.

Yreux, E. (2018). Fluid flow modeling with sph in LS-DYNA ®.

Appendix A

Design formulae impact wave loads on structure without overhang

Since wave impact loads are highly dynamic with an extremely stochastic nature, it is difficult to obtain an accurate analytical formula. Even though the short rise times disregard the possibility that wave impacts endanger the stability of the structure due to its inertia, it can be crucial for the strength of the structure, e.g. in case of partial collapse. Some models that are used for rough estimates are identified here.

Minikin (1963) developed a design procedure based on Bagnold's conceptual model and empirical results, by splitting the total load in a hydrostatic and dynamic component as illustrated in figure A.1.

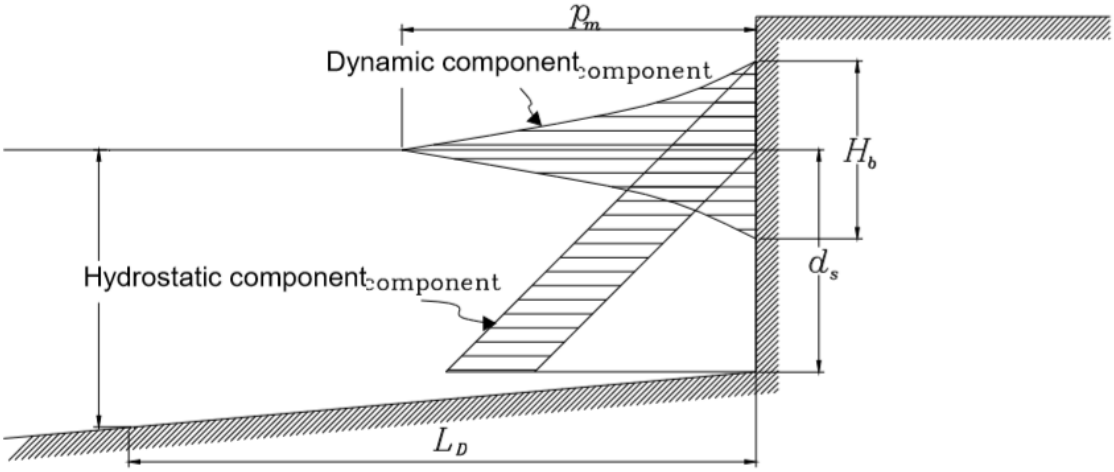

Figure A.1: Minikin's model for wave impact (Molenaar & Voorendt, 2016)

The pressure and total force is mathematically described by:

$$p_m = \frac{1}{2} C_{mk} \pi \rho g \frac{H_b}{L_D} \frac{d_s}{D} (D + d_s) \tag{A.1}$$

$$F = \frac{p_m H_b}{3} + \frac{\rho g H_b}{2} (\frac{H_b}{4} + d_s) \tag{A.2}$$

In which: C_{mk} = coefficient of impact (≈ 2) [-]
d_s = depth in front of wall [m]
D = depth at one wavelength in front of the wall [m]
L_D = wavelength at depth D [m]

It should be noted that this is the corrected version according to Kisacik et al. (2014). CERC (1984) gave unreasonable values due to a false unit conversion. In practice, Minikin's method is not used anymore due to its servere overestimation of the forces.

The Dutch standard for breaking wave loads (TAW, 2003) is the design procedure proposed by Goda as described in section 2.3.2. This model is extended by Takahashi and Hosoyamada (1993) and others to include wave breaking on a sill in front of the structure. In this extension, the geometry factors found in equation 2.12 do no longer equal 1. The modified factors are given by:

$$\begin{aligned} \lambda_1 &= \lambda_3 = 1 \\ \lambda_2 &= \max\left(1, \frac{\alpha_I}{\alpha_2}\right) \end{aligned} \tag{A.3}$$

In which:

$$\begin{array}{lll} \alpha_I &= \alpha_n \alpha_m & \text{(Impulse coefficient)} \\ \alpha_m &= \min\left(\frac{H_D}{d}, 2\right) & \\ \alpha_n &= \frac{\cos(\delta_2)}{\cosh(\delta_1)} & \text{if } \delta_2 \leq 0 \\ \alpha_n &= \frac{1}{\cos(\delta_1)\sqrt{\cosh(\delta_2)}} & \text{if } \delta_2 > 0 \\ \delta_1 &= 20\delta_{11} & \text{if } \delta_{11} \leq 0 \\ \delta_1 &= 15\delta_{11} & \text{if } \delta_{11} > 0 \\ \delta_2 &= 4.9\delta_{22} & \text{if } \delta_{22} \leq 0 \\ \delta_2 &= 3.0\delta_{22} & \text{if } \delta_{22} > 0 \\ \delta_{11} &= 0.93\left(\frac{B_M}{L_D} - 0.12\right) + 0.36\left(\frac{h-d}{h} - 0.6\right) & \\ \delta_{22} &= -0.36\left(\frac{B_M}{L_D} - 0.12\right) + 0.93\left(\frac{h-d}{h} - 0.6\right) & \end{array}$$

When the impulse loads become too great, Goda's formula is known to underestimate the total load (Oumeraci et al., 2001). Therefore, PROVERBS recommends a new prediction formula for preliminary design including the significant wave height H_{si} (average of the highest 1/3 of wave record):

$$F_{h,imp} = 15\rho g d^2 \left(H_s/d\right)^{3.134} \tag{A.4}$$

Further development of this formula including a probabilistic approach to include uncertainties and variability led to a rather extensive method, in which a relative maximum force $F^*_{h,imp}$ is defined following a generalised extreme value distribution with scale (θ), shape (ξ) and location (μ) parameters of the probability density function. $P_{\%}$ is defined as the probability of non-exceedance.

$$F_{h,imp} = F^*_{h,imp}\,\rho g H_b^2 \tag{A.5}$$

$$F^*_{h,imp} = \frac{\theta}{\xi}(1 - \xi \ln P_{\%}) + \mu \tag{A.6}$$

Cuomo et al. (2010) suggested a prediction formula based on Miche's breaking criterion (equation 2.1) using the subscript 1/250 as an indication of the average of the highest four events in a 1000-wave test:

$$F_{h,imp,1/250} = \rho g H_{mo}\, L_{hs} \left(1 - \frac{|h_b - h_s|}{h_s}\right) \tag{A.7}$$

In which:
H_{mo} = significant wave height [m]
L_{hs} = wavelength at toe structure [m]
h_s = water depth at structure [m]
h_b = water depth at breaking [m]

Cooker and Peregrine (1995) developed a pressure-impulse model for extreme wave impact. Based on Laplace's equation derived from a two-dimensional boundary-value problem and solved with a Fourier analysis. Violent impacts such as flip-through impact can be approximated using equation A.8.

$$P(x,y) = \rho H \sum_{n=1}^{\infty} a_n \sin(\lambda_n\, y/H) \frac{\sinh(\lambda_n(b-x)/H)}{\cosh(\lambda_n b/H)} \tag{A.8}$$

In which:
λ_n = $(n - \frac{1}{2})\pi$ [-]
y/H= position relative to vertical wall [m]
α_n = $2U_0 \frac{\cos(\mu\lambda_n - 1)}{\lambda_n^2}$ [-]
U_0 = velocity impacting wave [m/s]
b = length of wave [m]
μ = aeration factor [-]

Summarising, impact wave loads cause the highest peak pressures. The level of aeration and moment of breaking define the pressure distribution; low aeration generally result in higher pressures. Analytical formulae derived in the associated experiments capture the observed pressure distribution relatively well, yet can give unreliable values in other practical cases and thus should be treated with much care.

Appendix B

Variant study model setup

Multiple model setups have been tried to achieve the optimal SPH model with the most accurate results. In this chapter, a variant study has been conducted to show the reasoning behind the used model in this thesis. Three different boundary conditions have been tried: A rigid vertical wall of shell elements using tracer particles to obtain pressures, a vertical wall with small load cells and a symmetry plane.

B.1 Model with a rigid boundary

The first model that was tested had a rigid boundary as wall, meshed with shell elements similar to the overhang construction. Figure B.1 depicts an impression of the model with a long overhang. The wall was split up in segments to be able to read the reaction forces along the wall.

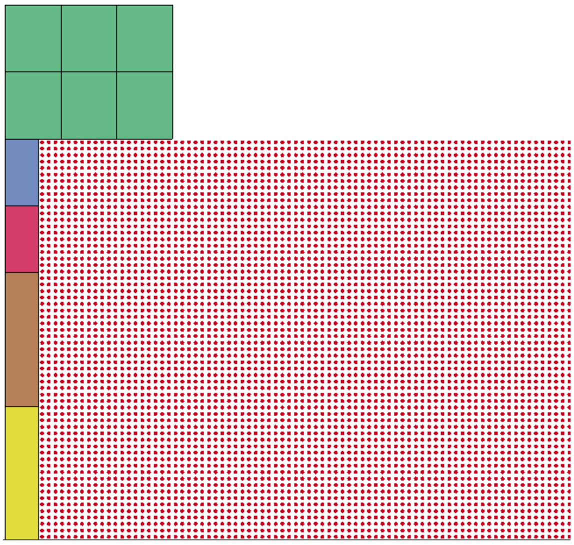

Figure B.1: Model with rigid boundary

This model setup came with two significant limitations. Firstly, particle sticking at the wall was observed, which disturbed the wave field as the reflection was not well reproduced. The particles formed a column against the wall as can be seen in figure B.2, due to some numerical friction. At a certain point, the column collapsed, but not before the wave was already moving up again. Therefore, some falling particles were observed to bounce off the surface elevation leading to singular particle impact, before the actual wave hit the structure. Due to the unreliable results that followed, this model was disregarded.

Furthermore, the pressures were obtained using so called tracer particles, which are ghost particles fixed in the domain extracting pressures. Unfortunately, this build-in function of LS-Dyna resulted in unrealistic pressures, which were far too high.

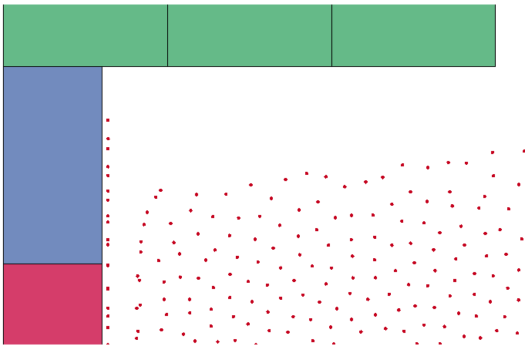

Figure B.2: Particle sticking

B.2 Model with load cells along the wall

The second model had a similar setup as aforementioned. However, now the rigid wall was split up in small load cells to obtain the reaction forces at the locations of the pressure sensors to subsequently divide by the area of the load cells to obtain the pressures. This was done to omit the tracer particle function. An impression is given in figure B.3.

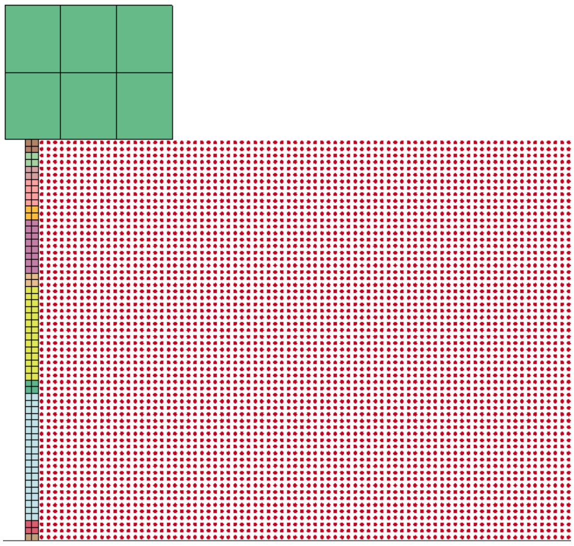

Figure B.3: Model with rigid boundary and load cells

This type of rigid boundary did not solve the particle sticking issue and a particle column was still observed. That said, in this configuration the model was able to extract accurate pressures for the sensors located near the overhang. However, closer to the bottom the results were too noisy as only a few particles interact with the load cells of 2 cm, i.e. only a maximum of 2 particles could interact. This led to a noisy and pressure distribution as shown in figureB.4 for sensors 1, 2 3 and 4, which was unusable to obtain pressure-impulses.

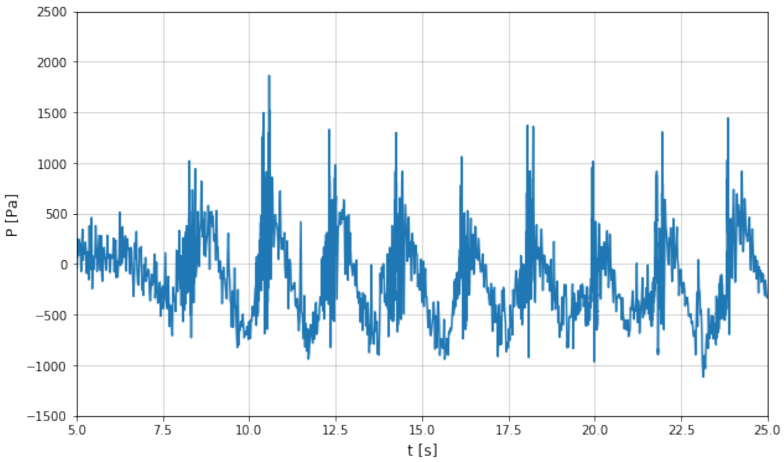

Figure B.4: Pressure distribution using load cells

B.3 Model with symmetry plane

In the third and final model, the rigid wall was replaced with a symmetry plane, which was also used for the bottom of the flume. Now, only the overhang consists of shell elements and particle interaction. Figure B.5 shows an impression of the model.

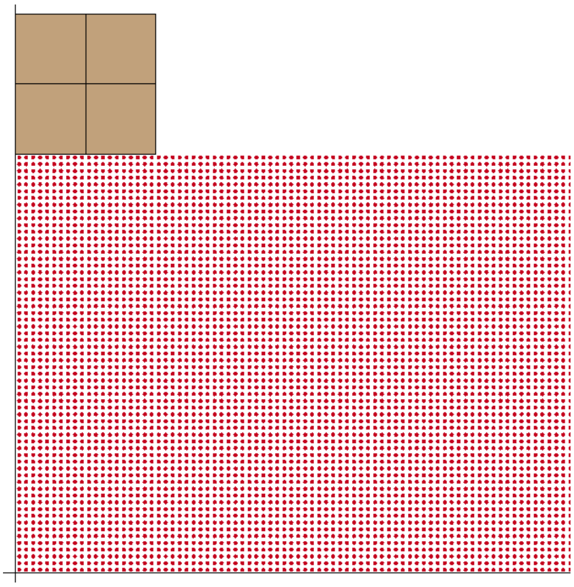

Figure B.5: Model using symmetry planes as boundary condition

For this case, no particle sticking was observed and the most accurate wave fields were obtained. Naturally, unreliable results would still be obtained if tracer particles were used. Therefore, a python script was written that modelled numerical pressure sensors in the particle domain, which were placed at the location of the experimental sensors with a buffer $\pm 1dp$. This was done to make sure a pressure was read at all time steps. The script extracted the nodal coordinates of the model over time, filtered the location of interest and used the pressure information stored on the particles. The numerical velocity fields were obtained in similar fashion. This method led to the most accurate results and was used throughout this thesis. That said, a limitation occurred in the lower part of the domain near the bottom. Here, particle clustering was observed, which resulted in a constant declining pressure field. Naturally, this is physically impossible and so the data of sensor

1 had to be disregarded for this research. Figure B.6 depicts the observed clustering and the pressure distribution that followed.

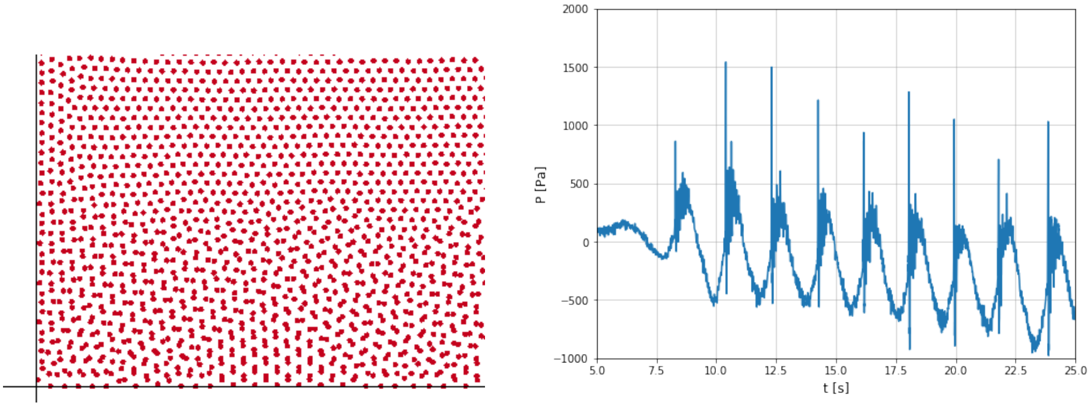

(a) Particle clustering (b) Pressure distribution for sensor 1

Figure B.6: Particle clustering

Appendix C

Miscellaneous results

In this chapter, the remaining results not included in the main report are depicted and described. These are the wave gauges, pressure sensors and numerical velocity fields. The quantification of the results is included in the main body of the thesis. Furthermore, the pressure drop as described in section 6.2.1 is further explained.

C.1 Wave gauges

All cases labelled with A indicate the wave condition $H = 0.06$ m and $T = 1.3$ s. The cases labelled with E indicate the wave condition $H = 0.1$ m and $T = 1.9$ s. The location of the wave gauges are presented in figure C.1 once again for convenience.

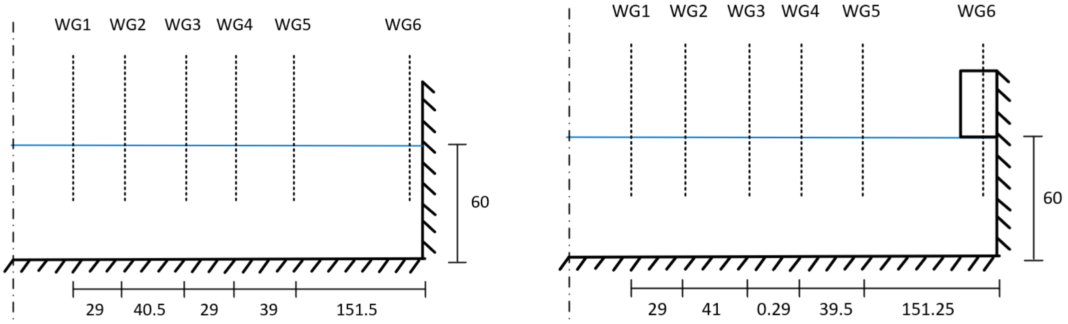

(a) Without overhang (b) With overhang

Figure C.1: Location of wave gauges

Starting with the cases without overhang, the wave heights are plotted in figure C.2 for wave gauges 2 and 5, case A, and for wave gauges 3 and 5, case E. The fit of the model and relative errors in wave height are quantified in table 6.1 and 6.2. The numerical wave field shows a very high overlap for all 4 wave gauges. R^2 values were found between 0.98 and 0.99 with very little relative erros in wave height. Furthermore, the wave field is stable due to the AWAS, as the case without overhang was modelled in DualSPHysics, in which this option was provided.

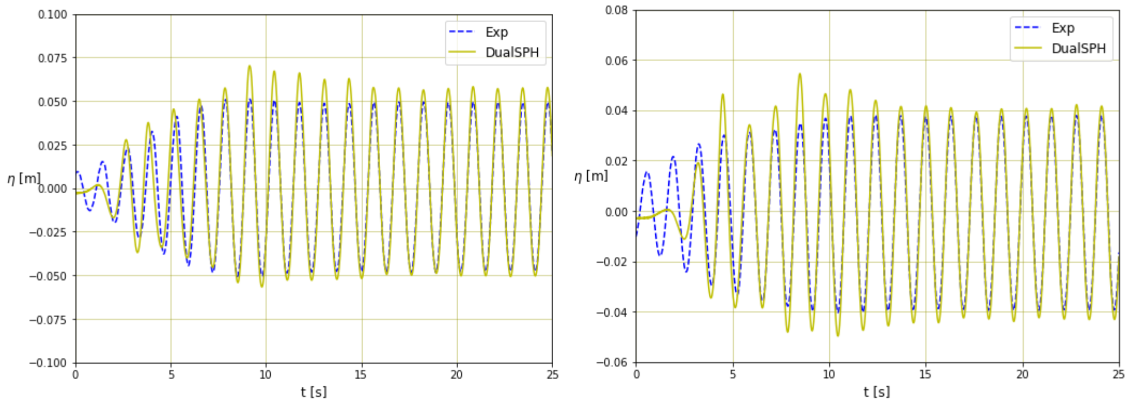

(a) Case A: WG2

(b) Case A: WG5

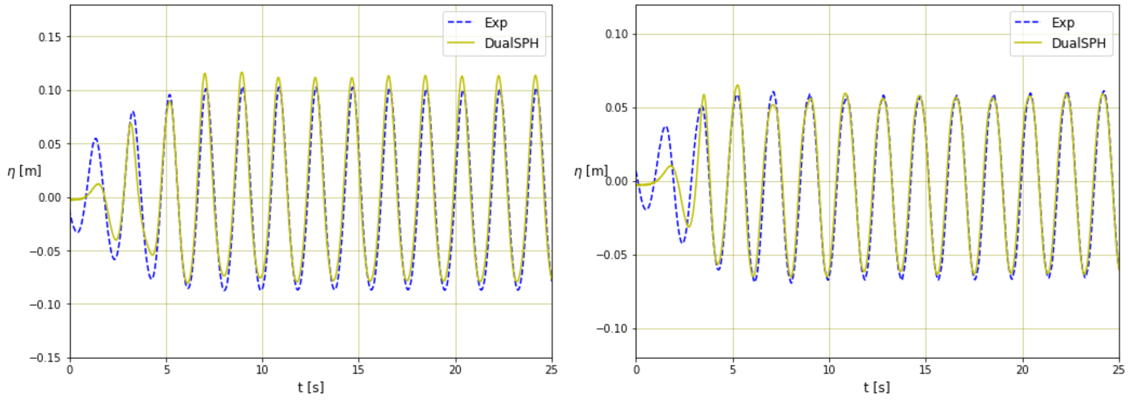

(c) Case E: WG3

(d) Case E: WG5

Figure C.2: Wave height comparison cases A and E without overhang

Continuing with the cases with a short overhang of 10 cm, wave gauges 3 and 5 for case AS and 3 and 4 for case ES are displayed in figure C.3. The quantification of the wave fields can be found in tables 6.3 and 6.4. Clearly, a less stable wave field is obtained for the overhang configurations. For the smallest wave height AS, a ratio of $H/dp = 10$ is not sufficed, which shows in the accuracy of the fit, i.e. 0.63 and 0.84 respectively, implying moderate to good agreement. Moreover, the peak of the wave is significantly lower.

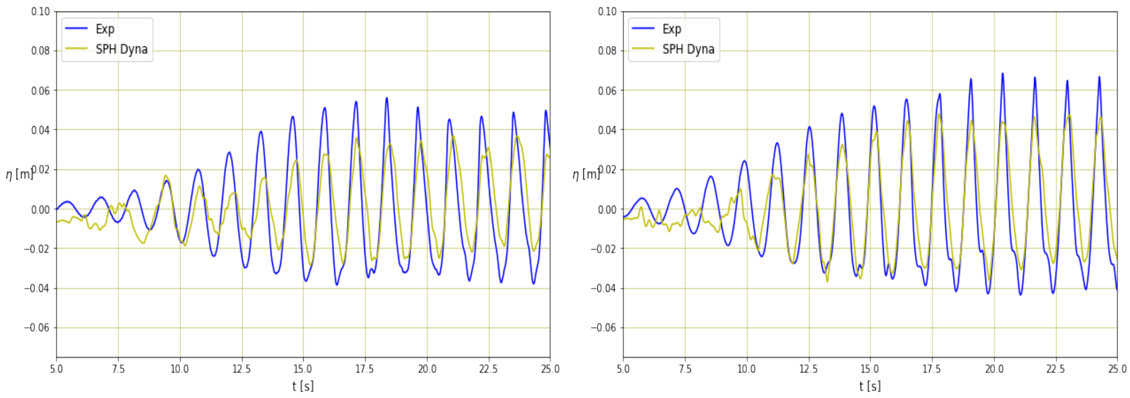

(a) Case AS: WG3

(b) Case AS: WG5

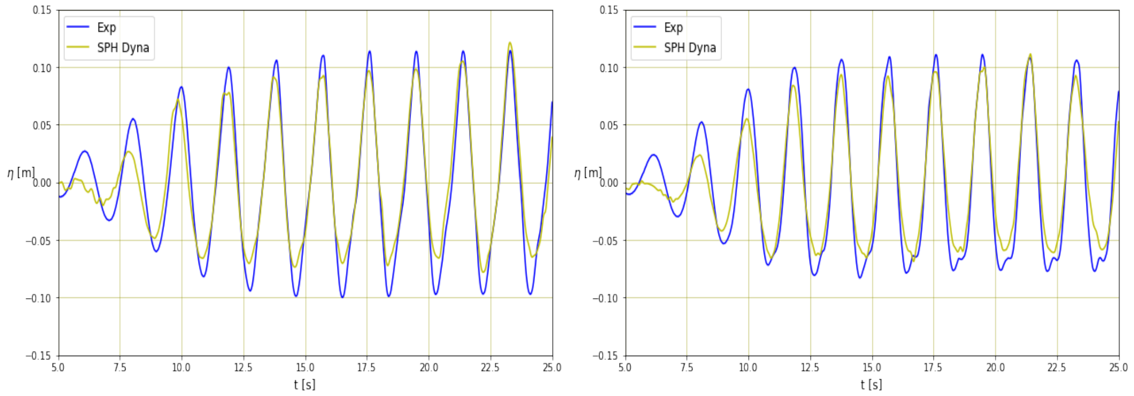

(c) Case ES: WG3 (d) Case ES: WG4

Figure C.3: Wave height comparison cases AS and ES with a short overhang

Increasing the wave height to 0.1 m, the goodness of fit increases to 0.95 for both WG3 and WG4 and thus shows excellent agreement between the experiment and the model.

Figure C.4 shows the results for the longer overhang configuration (20 cm) for WG3 and WG5, case AL, and WG2 and WG4, case EL. The quantification can be found in tables 6.5 and 6.6.

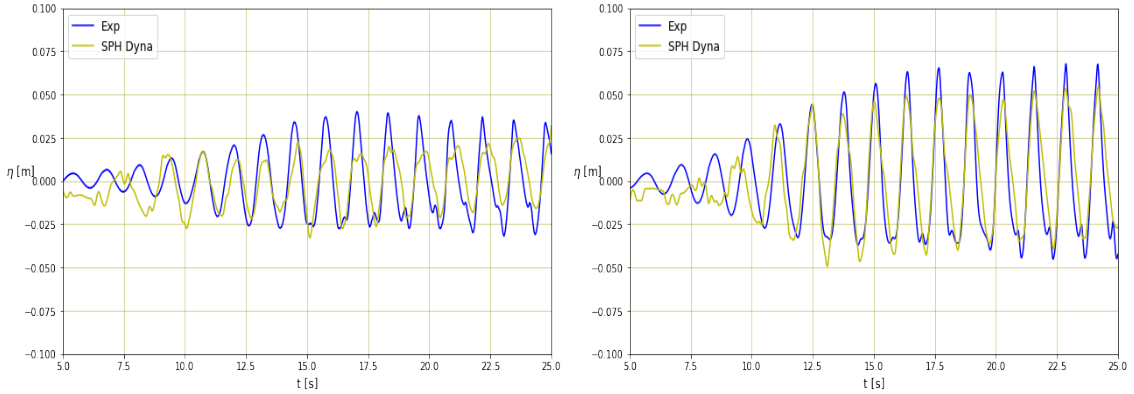

(a) Case AL: WG3 (b) Case AL: WG5

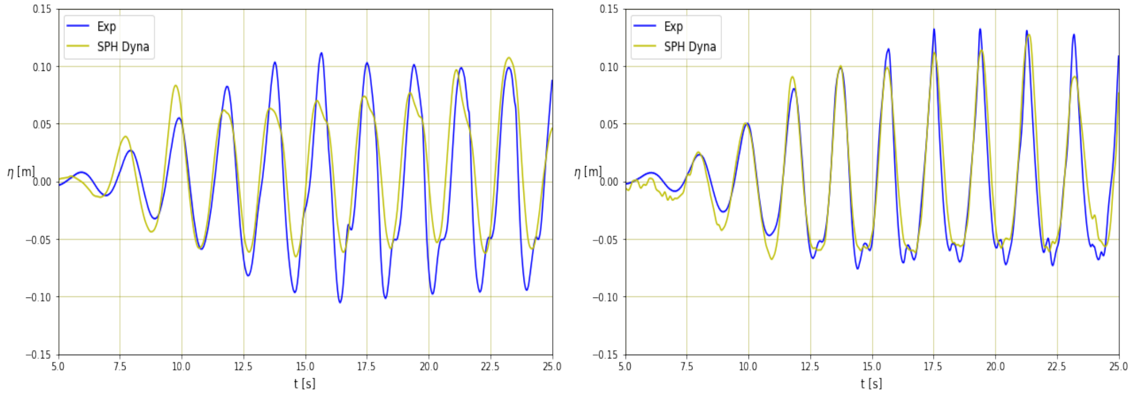

(c) Case EL: WG2 (d) Case EL: WG4

Figure C.4: Wave height comparison cases AL and EL with a longer overhang

For the longer overhang configuration, the same behaviour is observed as for the short overhang. The smallest wave height shows a similar level of fit of 0.61 and 0.87 for WG3 and 5 respectively. For the increased wave height, the fit improves to 0.73 and 0.94. Furthermore, less diffusion is observed in total height of the wave.

C.2 Pressure sensors

In this section, the pressure distributions are shown for the miscellaneous sensors, not included in the main body. The location of the sensors is presented in figure C.5. PS7 is located at 7 cm from the wall for the short overhang and at 17 cm from the wall for the longer overhang.

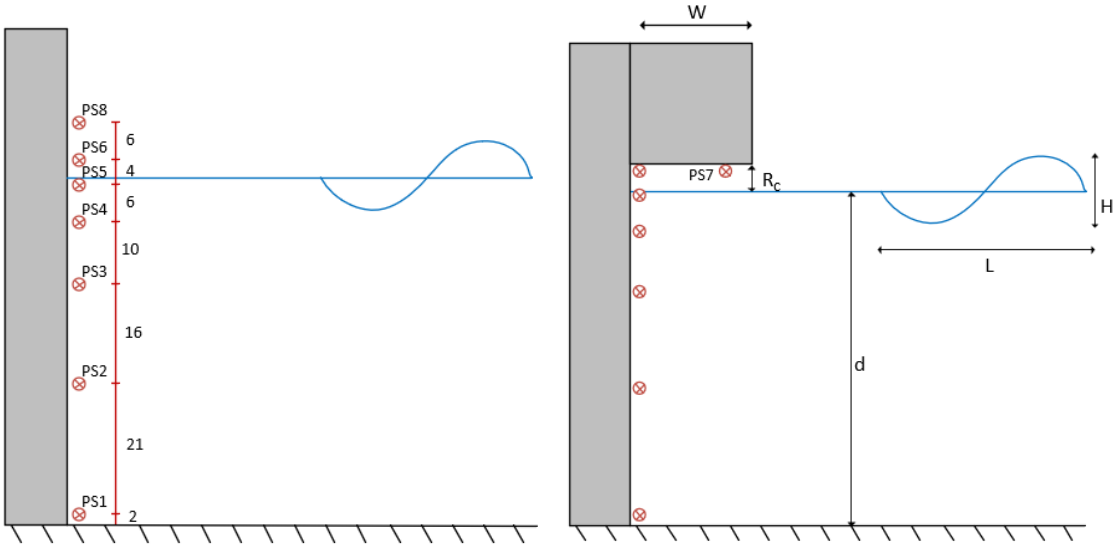

(a) Structure without overhang

(b) Structure with overhang

Figure C.5: Locations pressure sensors in [cm]

Firstly, case A and E are considered without an overhang. For both cases, sensors 2, 3 and 5 are depicted in figure C.6. The peak pressures are quantified in tables 6.7 and 6.8. As discussed in section 6.2.1, a gravity force is applied instantaneously at the start of the simulation, resulting in noise, which dissipates upwards. Therefore, the noise is more apparent for PS2 and PS3. Also, when a ratio of $H/dp = 10$ is sufficed, as is the case for case E, less noise is observed. That said, the accuracy of the numerical distribution after a steady state is achieved, is very high. Almost a 1 to 1 correlation is shown. Therefore, it was concluded that SPH is able to accurately reproduce the pressures and wave heights for the configuration without overhang.

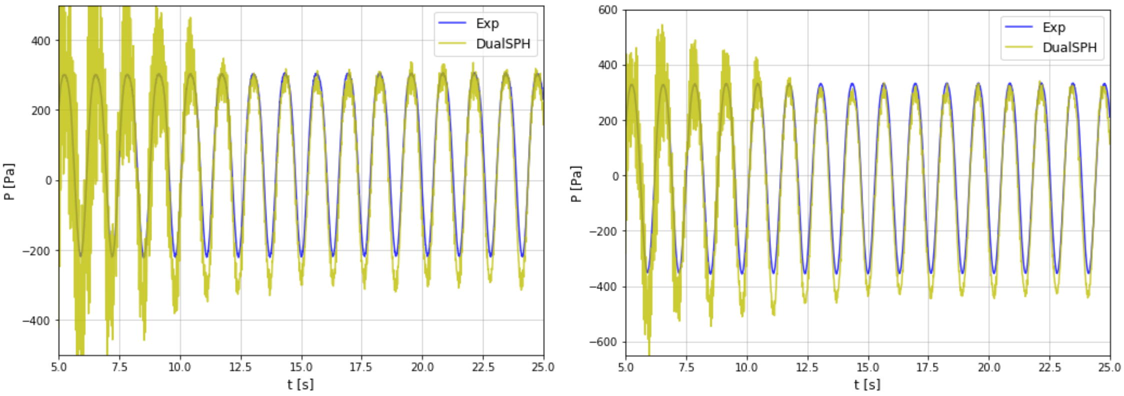

(a) Case A: PS2 (b) Case A: PS3

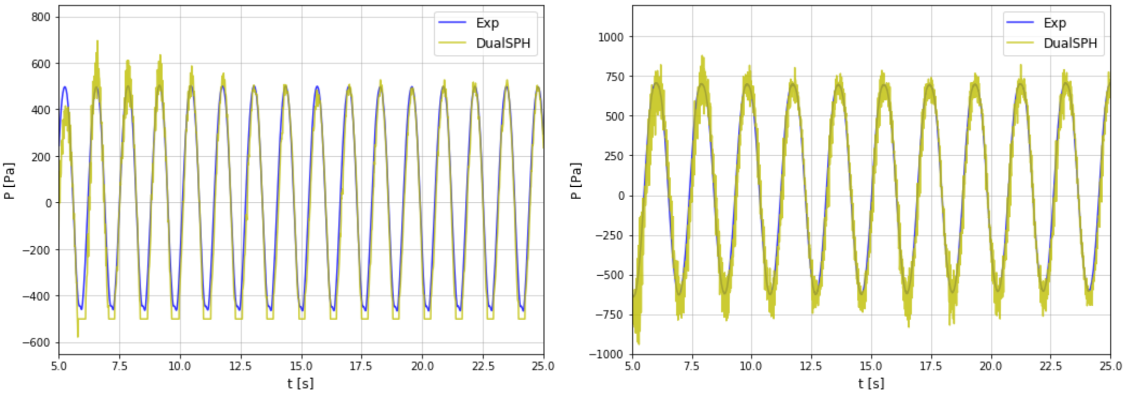

(c) Case A: PS5 (d) Case E: PS2

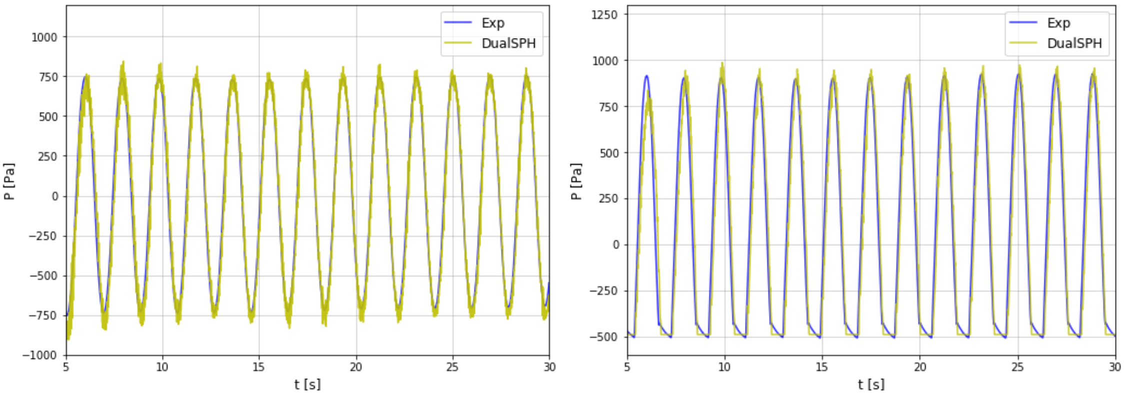

(e) Case E: PS3 (f) Case E: PS5

Figure C.6: Pressure comparison case A and E without overhang

Secondly, the overhang conditions are considered and displayed in figure C.7. The peak pressures are quantified in tables 6.9, 6.10, 6.11 and 6.12 for case AS and ES for the short overhang configuration and AL and EL for the longer overhang configuration, respectively. Note that only PS2 is depicted as PS1 reproduced unusable results due to particle clustering, as explained in appendix B.

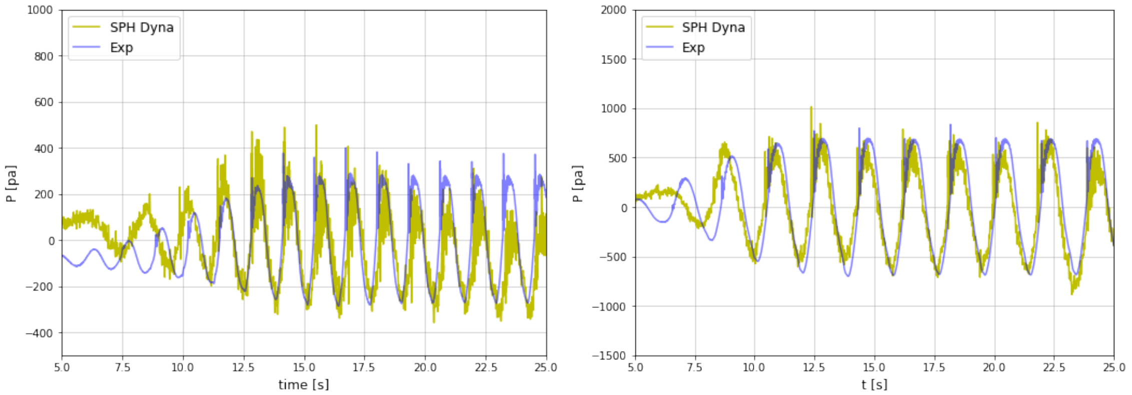

(a) Case AS: PS2 (b) Case ES: PS2

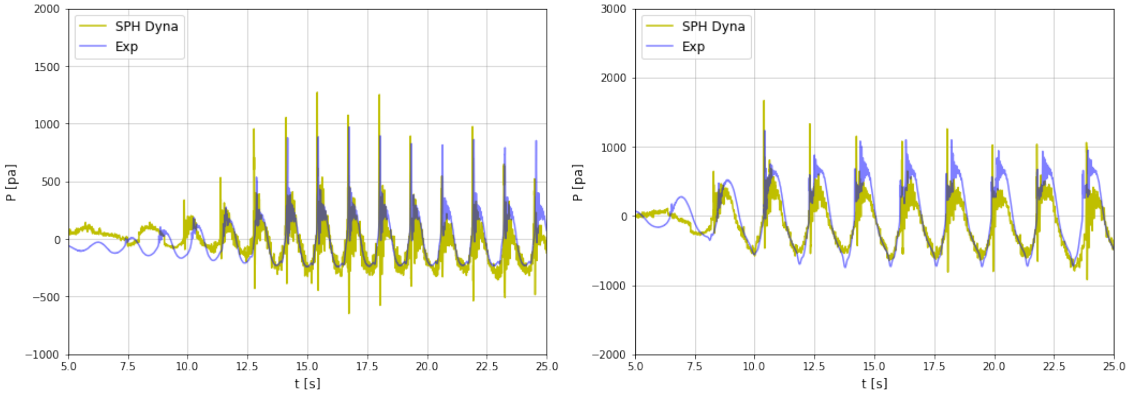

(c) Case AL: PS2 (d) Case EL: PS2

Figure C.7: Pressure comparison PS2, all overhang cases

Good agreement is found between the model and experiment in terms of pressure distribution and peaks. For the smaller wave heights (A), a bit more noise is observed due to the coarseness of the particle size compared to the wave height. In case AS, the distribution mildly affected by the particle clustering in the lower regions of the domain. For case EL, the experiment showed a double peaked impact, which was not reproduced by the model. However, the magnitude of the peaks shows similarity.

C.3 Pressure drop experiment

In this section, reasoning is given for the observed pressure drop for case A in section 6.2.1. Figure C.8 shows the pressure drop for both cases for sensor 8.

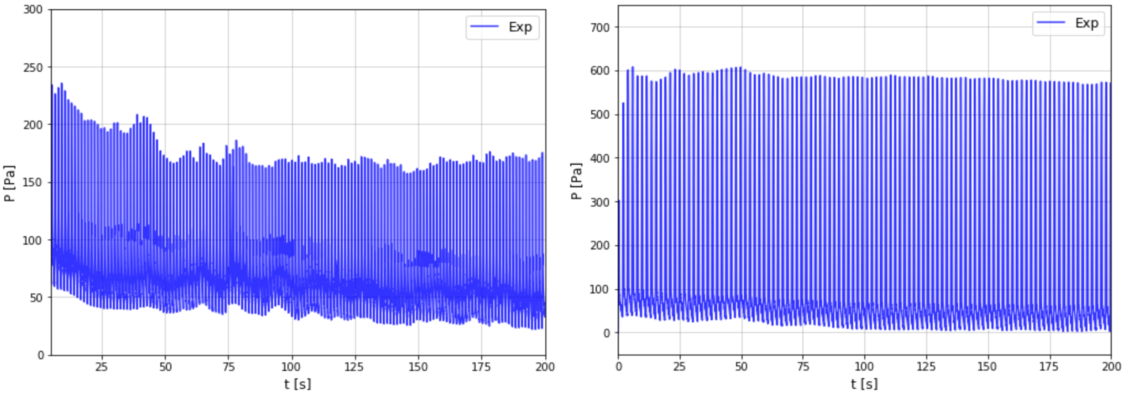

(a) Case A

(b) Case E

Figure C.8: Pressure drop experiment for sensor 8

Clearly, a pressure drop is observed for case A, while no significant drop is found for case E. This phenomenon is caused by temperature effects on the sensor. Since the sensor is located above the waterline, it is dry at first before the wave reaches the wall. When the first impact is registered and the sensor gets wet, the pressure drops. Due to the fact that the pressures are so low for this particular wave height, it will have a relatively high impact. For case E, the wave height increases and the pressures are doubled. Therefore, the pressure drops becomes less important. For the quantification in table 6.7, the average of peaks in the distribution is used after the sensor reaches a steady state.

C.4 Numerical velocity fields short overhang

In this final section, the numerical velocity fields are depicted for the **short overhang condition** with $h = 0.1$ m, i.e. case ES. In the main report, the velocity fields of both the longer overhang (case EL) and the short overhang configurations are used to obtain modified areas of integration for the conceptual model. Figure C.9 shows the stoppage of the velocities at impact.

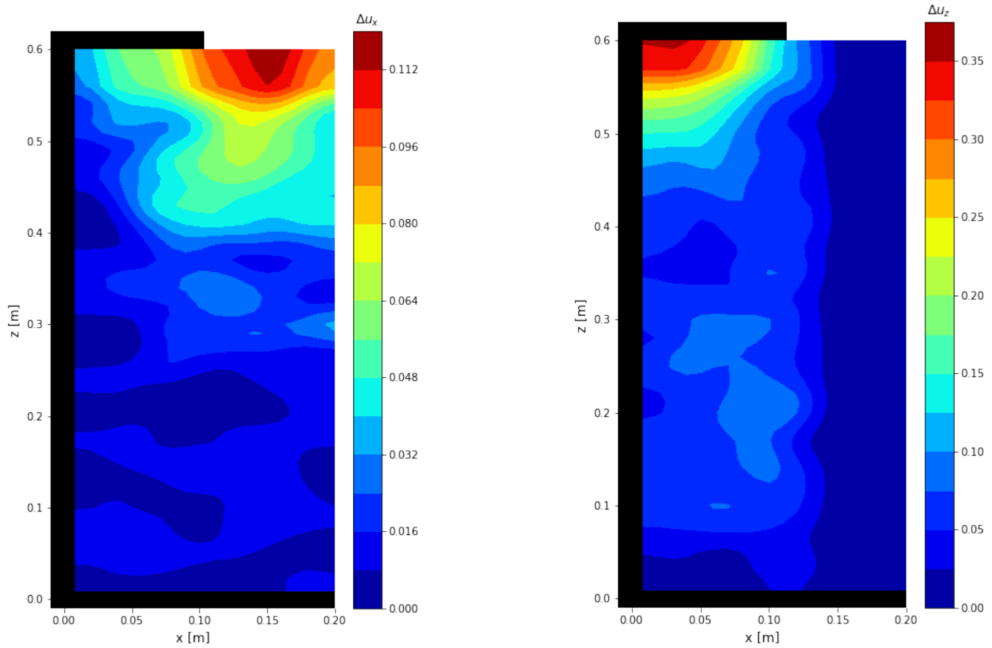

(a) Δu in x-direction in [m/s]

(b) Δu in z-direction in [m/s]

Figure C.9: Stoppage of velocities at impact for case ES

It is observed that the impact consists of a horizontal and vertical component. However, the x-component is dominated by the wave hitting the side of the overhang. Therefore, no conclusion can be drawn about the range in which the x-velocities are stopped purely due to the upward impact on the overhang. For the upward velocity, a circular profile in the stoppage of the velocities. Although, a clear decrease in velocities is observed over the width of the overhang and downwards along the wall. This is unlike the theoretical pressure-impulse model, which assumes a constant velocity in the circular profile. Compared to the longer overhang, it is observed that the dissipation of the velocities over the circular profile is not as strong. In other words, the stopped upward velocity is more constant for the short overhang.

In section 6.5.2, the numerical velocity fields just before impact are displayed for the longer overhang configuration and compared to linear wave theory. This is done to verify if the SPH model can be used to propose new areas of integration for the conceptual model to optimise the fit of its pressure-impulse profiles. The same is done in figure C.10 for the short overhang.

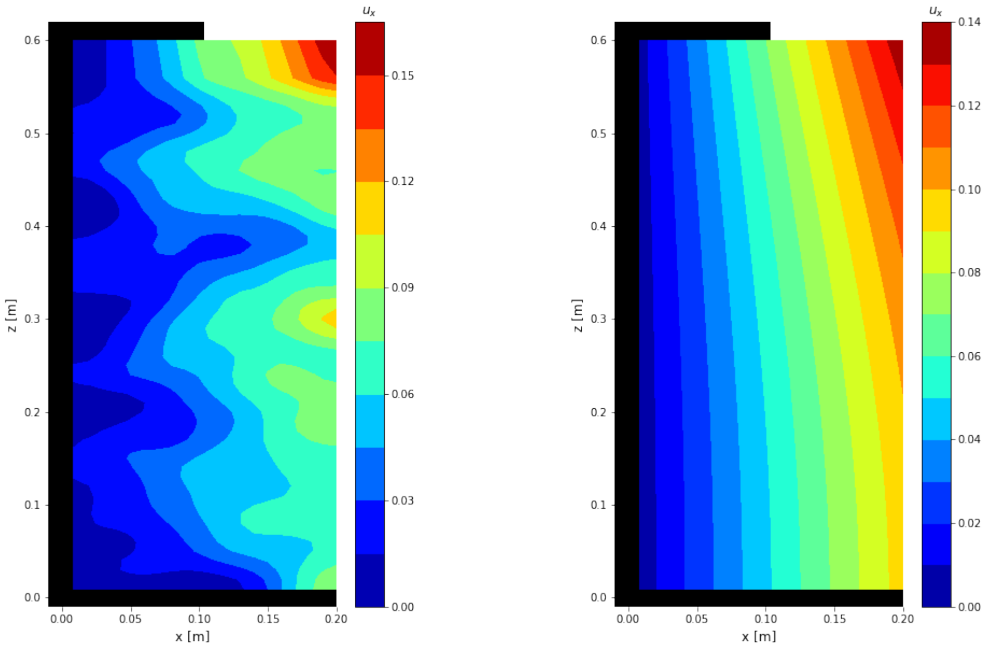

(a) u_x: SPH (b) u_x: LWT

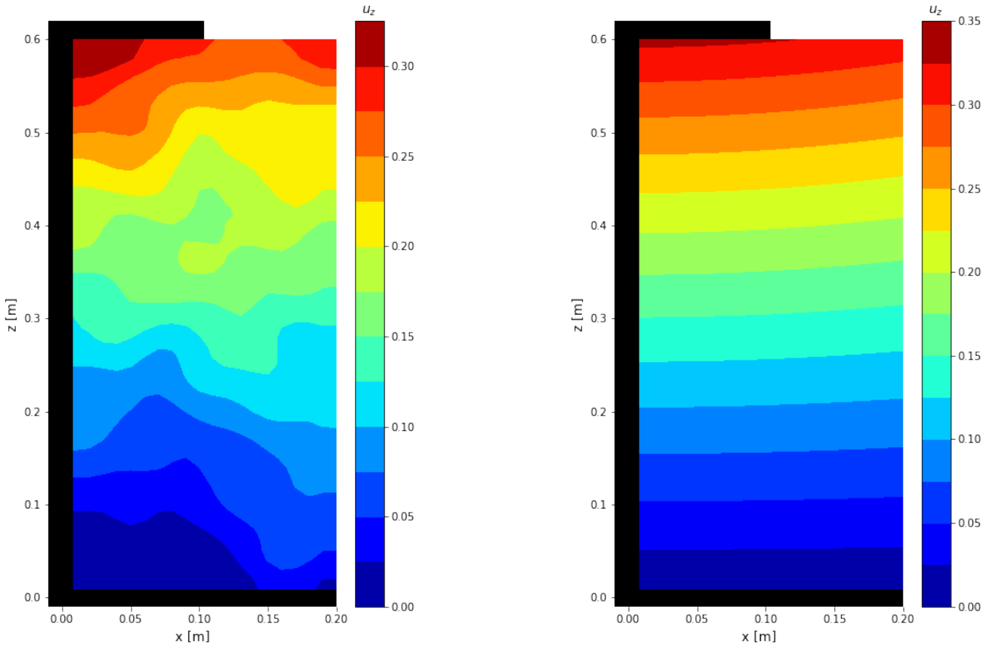

(c) u_z: SPH (d) u_z: LWT

Figure C.10: Numerical velocity field before impact compared to LWT for case ES

It is observed that the contour lines of the x-velocities are not as straight compared to the theory and show less accuracy compared to the longer overhang. Close to the waterline, the velocities are well approximated by the model. Better agreement is found for the vertical velocities as here, the contour lines are similar to the theory. Furthermore, the magnitude of the velocities has good agreement for both directions. Therefore, it is concluded that SPH can be used for direct integration of the velocities to propose modifications to the conceptual model.